

5-2018

## Electro-thermal Transport in Non-homogenous Network

Sajia Sadeque  
*Purdue University*

Follow this and additional works at: [https://docs.lib.purdue.edu/open\\_access\\_dissertations](https://docs.lib.purdue.edu/open_access_dissertations)

---

### Recommended Citation

Sadeque, Sajia, "Electro-thermal Transport in Non-homogenous Network" (2018). *Open Access Dissertations*. 1816.  
[https://docs.lib.purdue.edu/open\\_access\\_dissertations/1816](https://docs.lib.purdue.edu/open_access_dissertations/1816)

This document has been made available through Purdue e-Pubs, a service of the Purdue University Libraries.  
Please contact [epubs@purdue.edu](mailto:epubs@purdue.edu) for additional information.

ELECTRO-THERMAL TRANSPORT IN NON-HOMOGENEOUS NETWORK

A Dissertation

Submitted to the Faculty

of

Purdue University

by

Sajia Sadeque

In Partial Fulfillment of the

Requirements for the Degree

of

Doctor of Philosophy

May 2018

Purdue University

West Lafayette, Indiana

**THE PURDUE UNIVERSITY GRADUATE SCHOOL**  
**STATEMENT OF COMMITTEE APPROVAL**

Dr. David B. Janes, Chair

Department of Electrical and Computer Engineering

Dr. Ali Shakouri

Department of Electrical and Computer Engineering

Dr. Muhammad A. Alan

Department of Electrical and Computer Engineering

Dr. Zhihong Chen

Department of Electrical and Computer Engineering

**Approved by:**

Dr. Brian S. King

Head of the Graduate Program

*Dedicated to my parents,*

*Yasmin Akhter*

*and*

*Abdus Sadeque*

## ACKNOWLEDGMENTS

First, I would like to sincerely thank my supervisor, Professor David B. Janes, for his guidance, encouragement, and support throughout the PhD years. He spent an enormous amount of time guiding me and discussing my work. He provided me directions to overcome various research issues I encountered. I would like to take this opportunity to express my heartfelt gratitude, and say how fortunate I am to have him as my advisor.

I would like to thank Professor Ali Shakouri for the useful discussions and thoughtful comments, and for allowing me to use his lab facility for thermal measurements. I am thankful to Professor Muhammad Ashraful Alam for his insightful comments and suggestions throughout this work. I am grateful to Professor Zhihong Chen for taking time to evaluate my work and provide valuable feedbacks.

I would like to thank Professor Timothy Fisher and Aaditya Candadai for the great collaboration and for all helpful discussions.

I am obliged to all the technical staff members, administrative staff, friends and colleagues at Birck Nanotechnology Center, including Dave Lubelski, and Dr. Joon Hyeong Park. I would like to thank Dr. Kerry Maize, Dr. Amir K. Ziabari, Dr. Amr M. S. Mohammed, and Yu Gong for their continual experimental support. I really appreciate the support and assistance from the past and present members of our research group, including Dr. Collin Delker, Dr. Suprem Das, Asaduzzaman Mohammad, Jose Rivera-Miranda, Siddarth Sridharan, Doosan Back, and Jiseok Kwon.

I would like to acknowledge the support of National Science Foundation (NSF) for providing funding throughout my work.

Last but not least, I would like to thank wholeheartedly my family members-my parents, my sisters, my husband and my wonderful daughter, for their continual encouragements, love, support and sacrifices without which this journey would not have been successful.

## TABLE OF CONTENTS

	Page
LIST OF TABLES .....	vii
LIST OF FIGURES .....	viii
ABSTRACT .....	xviii
1. INTRODUCTION .....	1
1.1 Non-homogenous Network based Transparent Conducting Electrodes and its Classification .....	1
1.2 Graphene-Silver Nanowire Coperculating Hybrid Network .....	3
1.3 Current and Heat Transport in Homogenous and Non-homogenous Network.....	4
1.4 Electro-thermal Conduction in Non-homogeneous Network .....	6
1.5 Organization of Thesis .....	9
1.6 List of Associated Publications .....	10
2. COPERCOLATING NETWORKS: AN APPROACH FOR REALIZING HIGH PERFORMANCE TRANSPARENT CONDUCTORS USING MULTI- COMPONENT NANOSTRUCTURED NETWORKS .....	12
2.1 Overview .....	12
2.2 Performance Comparison of Thin-Film and Nanostructured Network Based TCEs. ....	12
2.2.1 Selection of Representative Studies .....	12
2.2.2 Comparison of Sheet Resistance versus Transmittance Performance ..	14
2.2.3 “Effective” Thickness of Transparent Conducting Films .....	15
2.2.4 Physical Model for Bulk Material and Adaptation for Nanostructured Non-homogenous TCEs .....	17
2.2.5 Physical Validity of Typical Figure of Merit .....	21
2.3 Conclusion .....	22
3. FABRICATION AND MEASUREMENT TECHNIQUES .....	23
3.1 Fabrication of Non-homogenous Networks .....	23
3.2 Transient Thermoreflectance Imaging Technique.....	25
4. TRANSIENT THERMAL RESPONSE OF HOTSPOTS IN GRAPHENE-SILVER NANOWIRE HYBRID TRANSPARENT CONDUCTING ELECTRODES .....	29
4.1 Overview .....	29

4.2	Transient Response of Hotspots .....	29
4.3	Radial Dependence of Time Constants and Amplitudes of Hotspots .....	33
4.4	Self-Heating and Heat Diffusion Model .....	36
4.5	Local Self-heating .....	36
4.5.1	Local Self-heating at Hotspots.....	36
4.5.2	Local Self-heating in Homogenous Conductor .....	37
4.6	Heat Diffusion through Channel Region .....	40
4.6.1	Simulation of Diffusion of Heat from Electrical Contacts.....	41
4.6.2	Transformation of Heat Diffusion Equation from 3-D Cylindrical Geometry to a 2-D Cartesian Geometry.....	42
4.6.3	Simulation Results .....	43
4.7	Transient Response of Non-Hotspots .....	47
4.8	Determination of Network Material Parameters .....	49
4.9	Determination of Thermal Resistances of Network and Substrate .....	50
4.10	Conclusion .....	51
5.	TRANSIENT SELF-HEATING AT NANOWIRE JUNCTIONS IN SILVER NANOWIRE NETWORK CONDUCTORS .....	52
5.1	Overview .....	52
5.2	Thermal Transients of Microscopic Hotspots in Silver Nanowire network .....	54
5.2.1	Temporal Evolution of Microscopic Hotspots .....	56
5.2.2	Determination of Thermal Time Constants .....	59
5.3	Temperature Rise Vs Length Profile .....	64
5.4	High-resolution Imaging of Adjacent Hotspots .....	65
5.5	Heat Transfer Model.....	67
5.5.1	Single Nanowire-Nanowire Junction Analysis.....	67
5.5.2	Determination of Thermal Interface Resistance between Nanowire and Quartz .....	70
5.5.3	Multiple Nanowire-Nanowire Junctions Analysis.....	75
5.6	Construction of Binary Mask .....	78
5.7	Determination of Heat Transfer Coefficient $h$ .....	79
5.8	Determination of Number of Hotspots .....	79
5.9	Determination of Substrate Contact Length of Nanowire .....	80
5.10	Circuit Representation of Hotspots in Silver Nanowire Network .....	82
5.11	Broadening of Temperature Profiles .....	83
5.12	Conclusion .....	84
6.	COMPARATIVE STUDIES OF TRANSIENT THERMAL RESPONSES OF HOTSPOTS IN GRAPHENE-SILVER NANOWIRE NETWORK AND SILVER NANOWIRE NETWORK .....	86
6.1	Overview .....	86

6.2	Comparative Transient Thermal Characteristics of Individual Hotspots .....	87
6.3	Collective Thermal Characteristics of Hotspots.....	91
6.3.1	Comparison of Evolution of Number of Hotspots .....	91
6.3.2	Comparison of Evolution of Average Hotspot Temperature .....	93
6.3.3	Comparison of Evolution of Spatial Distributions.....	94
6.3.4	Comparison of Evolution of Average Network Temperature .....	98
6.4	Comparison of Microscopic versus Macroscopic Behavior .....	99
6.4.1	Resistive Current Pathways .....	101
6.4.2	Local Heat Spreading .....	106
6.5	Conclusion .....	108
7.	TIME DEPENDENT TEMPERATURE DISTRIBUTIONS IN SILVER NANOWIRE NETWORK CONDUCTORS .....	110
7.1	Overview .....	110
7.2	Temporal Evolution of Temperature Distributions in Self-Heating Regime of 0-10 $\mu$ s .....	111
7.3	Temporal Evolution of Temperature Distributions in Heat Diffusion Regime of 0- 450 $\mu$ s .....	114
7.4	Simulation of Self-heating and Heat Diffusion in Silver Thin Film .....	117
7.4.1	Simulation of Self-heating in Silver Thin Film .....	118
7.4.2	Simulation of Heat Diffusion from Electrical Contacts to Silver Thin Film.....	121
7.5	Conclusion .....	124
8.	SUMMARY, CONCLUSION, AND FUTURE WORK.....	125
8.1	Research Objective, Summary and Conclusion .....	125
8.2	Future Work .....	127
	LIST OF REFERENCES.....	128
	VITA.....	136

## LIST OF TABLES

Table	Page
Table 1.1: List of publications and their chapter relevance .....	10
Table 2.1: Comparison of $t_{eff}$ for representative studies on various classes of TCEs ....	20
Table 4.1: Physical properties used for calculation of $\rho_{Hybrid}, C_{Hybrid}, \kappa_{Hybrid}$ ....	49
Table 5.1: Amplitudes and thermal time constants of different hotspots .....	62
Table 5.2: Summary of the material and thermal properties. ....	72
Table 5.3: Summary of the derived parameters. ....	72
Table 6.1: Macroscopic Properties of Silver NW and Hybrid Network .....	100
Table 6.2: Microscopic Observations and Average Power at Hotspots .....	101
Table 6.3: Estimated Thermal Resistances and Temperatures of Junctions .....	108

## LIST OF FIGURES

Figure	Page
Fig. 1.1: Three generations of TCEs (figure is taken from [1]).	3
Fig. 1.2: (a) and (b) Homogeneous TCE e.g. ITO at different visual scales; figures are taken from [25] and [26] respectively; (c) and (d) Non-homogeneous TCE e.g. silver NW network at different visual scales; figures are taken from [27] and [28] respectively.	5
Fig. 1.3: (a) Uniform heating in homogenous conductor (e.g. ITO heater); figure is taken from [29] (b) Non-uniform heating (hotspot formation) in non-homogeneous network [24].	5
Fig. 1.4: (a) Temperature rise due to self-heating (i.e. electro-thermal response) at a hotspot can be used to probe the current at the NW-NW junction; (b) The maximum heating occurs at the weak links in the most conducting paths.	7
Fig. 1.5: Different methods to characterize transient heat dynamics. (a)-(c) Silver NW networks using Infra-red thermography, spatial resolution in ‘mm’ range. Figures are taken from [34], [35], and [32] respectively. (d) CNT networks using inverted optical microscopy, spatial resolution in ‘ $\mu\text{m}$ ’ range; figure is taken from [36]. In all cases, temporal resolution is in ‘s’ or ‘min’ range.	8
Fig. 2.1: Optical transmittance versus log of sheet resistance for representative studies on various types of transparent conductors. The various studies are summarized in the text.	15

Fig. 2.2: Optical transmittance vs. normalized thickness for representative studies on various types of transparent conductors. A linear relationship (Eq. (2.5)) is also shown for reference. The various studies are summarized in the text. ....	19
Fig. 2.3: Sheet Conductance versus normalized thickness for representative studies on various types of transparent conductors. A linear relationship (Eq. (2.4)) is also shown for comparison. The various studies are summarized in the text. ....	19
Fig. 3.1: Fabrication steps of silver NW and graphene-silver NW based hybrid non-homogenous network.....	24
Fig. 3.2: (a) Schematics of silver NW network; (b) Schematics of graphene-silver NW hybrid network; (c) Samples prepared with 4 different densities of silver NWs.....	24
Fig. 3.3: CCD image of a hybrid network as captured by a 20x lens showing the concentric circular inner and outer electrical contact pads along with the electrical probes used for electro-thermal (i.e. transient thermoreflectance) measurements. ....	25
Fig. 3.4: (a) Experimental set-up of TR measurement (b) 20x CCD image of a hybrid device showing the circular contacts along with the probes (c) Schematics of the transient TR measurements showing the device heating pulse, heating and cooling cycle and delay $\tau_D$ of the LED pulse.....	27
Fig. 4.1: Transient response at different $\tau_D$ s showing formation of hotspots during heating cycle at (a) 10 $\mu$ s, and (b) 450 $\mu$ s respectively and during cooling cycle at (c) 520 $\mu$ s, and (d) 980 $\mu$ s respectively. Left and right dotted lines represent the inner and the outer contacts respectively. Four different hotspots located 46, 71, 87, and 134 $\mu$ m away from the center of the inner contact are labelled and denoted as hotspots 1- 4, respectively, throughout the chapter. ....	30
Fig. 4.2: Schematic of a hotspot.....	31

- Fig. 4.3:  $\Delta T$  vs time (i.e.  $\tau_D$ ) for long device heating pulse of 450  $\mu s$  (a) heating cycle (b) cooling cycle for hotspots 1- 4 (Fig. 4.1).....32
- Fig. 4.4:  $\Delta T$  vs time (i.e.  $\tau_D$ ) for short device heating pulse of 10  $\mu s$  (a) heating cycle (b) cooling cycle for hotspots 1- 4 (Fig. 4.1).....33
- Fig. 4.5: (a)  $\tau_1, \tau_2$  vs distance ( $r$ ) for hotspots (HSs) and non-hotspots (NHSs). Dashed line represents simulation (calculated) results for  $\tau_{2H}$  ( $\tau_{1H}$ ). (b)  $A_1$  vs  $r$  for the same. Dashed line represents the analytical solution for  $A_{1H}$ . (c)  $A_2$  vs  $r$  for the same. Dashed line represents the simulation results for  $A_{2H}$ . The simulations and the analytical results are for HSs during the heating cycle.  $r < 40 \mu m$  and  $r > 140 \mu m$  represent the inner and the outer electrical contact regions respectively. Vertical dashed lines correspond to the boundaries between contacts and channel region.  $\tau_1, \tau_2, A_1,$  and  $A_2$  values of hotspots 1-4 are shown in arrows.....35
- Fig. 4.6: Geometry considered for analytical model of self-heating in homogenous conductor e.g. metal thin film .....38
- Fig. 4.7: Thermal transient of the hotspot at the edge of the inner contact (at  $r = 32 \mu m$ ) used to obtain boundary condition for temperature rise in the inner contact. ..42
- Fig. 4.8: (a) PDE simulation results at 450  $\mu s$  across quartz. The cross-sectional view of the inner and outer contacts are also shown. (b) Zoomed out view of (a). Here,  $r' = 280 \mu m$  corresponds to the center of the inner contact i.e.  $r = 0$ .....44
- Fig. 4.9: Experimental  $\Delta T - A_{1H}$  (i.e. temperature rise due to diffusion only) vs distance at different time ( $\tau_D$ ).  $A_{1H}$  is different for different HSs. Solid lines represent plots generated from PDE simulation. Simulation plots show the trends of the experimental data. Here, distance corresponds to distance from the edge of the inner contact towards the right outer contact ( $r' = 320 - 380 \mu m$  from Fig. 4.8).....45

- Fig. 4.10: Experimental  $\Delta T - A_{IH}$  vs time ( $\tau_D$ ) for different HSs located at different distances. Solid lines represent plots generated from PDE simulation. Simulation plots represent the trends of the experimental data. ....46
- Fig. 4.11: Simulation of  $\Delta T - A_{IH}$  vs time ( $\tau_D$ ) for  $\tau_D = 3000 \mu s$ .....47
- Fig. 4.12:  $\Delta T$  profile for a hotspot and nearby non-hotspot.....48
- Fig 5.1: (a) Relative timing diagrams of applied voltage pulse, LED pulse showing delay  $\tau_D$ , and temperature rise/fall during the heating (voltage pulse “on”) and cooling cycle; (b) CCD image at  $\tau_D = 10 \mu s$  of the portion of the silver NW network visible within the field of view of 100x lens; (c) Corresponding thermal image at  $\tau_D = 10 \mu s$ ; (d) CCD image superimposed on the thermal image to illustrate the physical location of hotspots with respect to the NW junctions. ....55
- Fig. 5.2: Thermal images at different time (i.e.  $\tau_D$ ) during the heating cycle at (a) 400 ns (b) 1  $\mu s$  (c) 2  $\mu s$  and during the cooling cycle at (d) 10.4  $\mu s$  (e) 10.6  $\mu s$  (f) 11  $\mu s$ . ....56
- Fig. 5.3: (a) False color CCD image of randomly dispersed silver NW network showing several NWs and junctions with NW #1 and NW #2 highlighted in red lines; (b) TR image superimposed on grayscale CCD image to show the physical location of the hotspot at the junction. Yellow rectangles in (a) and (b) denote the same region (“location 1”).....57
- Fig. 5.4: False color CCD image of randomly dispersed silver NW network near location 1 showing several NWs and junctions.....58
- Fig. 5.5: TR images at different time (i.e. delay  $\tau_D$ ) show evolution of the local heating near the microscopic hotspot at location 1 at (a) 0 ns (b) 400 ns (c) 1  $\mu s$  (d) 2  $\mu s$ . ....58

- Fig. 5.6:(a) Several NW-NW junctions (location 2,3,and 4) are shown in a 100x grayscale CCD image of AgNW network; (b) Corresponding TR image at 1  $\mu$ s;(c) Merged CCD and TR image at 1  $\mu$ s show formation of the microscopic hotspots at these NW-NW junctions..... 60
- Fig. 5.7:  $\Delta T$  vs.  $\tau_D$  profiles of the hotspots located at 2, 4, and 6 during the (a) heating cycle (b) cooling cycle..... 61
- Fig. 5.8: TR image at 400 ns showing various microscopic hotspots. The values of amplitudes  $A$  and  $\tau$  of the circled hotspots are listed in Table 5.1. .... 63
- Fig. 5.9: (a,b) CCD images; (c,d) TR images at 400 ns of the microscopic hotspots located at locations 4 and 6. .... 64
- Fig. 5.10: (a)  $\Delta T$  vs length profiles along NW #1 and NW #2 at different time delays (0 ns – 2  $\mu$ s). .... 65
- Fig. 5.11: (a) False color CCD image of portion of silver NW network showing several NW-NW junctions. (b) 4 NWs are labelled NW B1, B2, B3 and B4 that form junctions. (c) TR image at 1  $\mu$ s. Two hotspots within the yellow rectangle region are 5 pixels ( $\sim 1 \mu$ m) apart. (d) CCD images and thermal image are merged to confirm that the hotspots (within yellow rectangle region) coincide with the NW-NW junctions. (e)  $\Delta T$  vs length profiles along NW B1 at different delays. Arrows indicate  $\Delta T$  peaks corresponding to each of the three indicated NW-NW junctions..... 66
- Fig. 5.12: Geometry for the heat transfer model. (a) Symmetry considered for the model and configuration of the top and the bottom NW along with the contact length  $l_C$ . (b) Thermal interface resistances (constriction and gap thermal resistance). .... 68

- Fig. 5.13: Comparison of experimental data at  $1 \mu\text{s}$  with numerical results from the heat transfer model (a) for the top NW (i.e. NW #1) (b) bottom NW (i.e. NW #2). 74
- Fig. 5.14: Comparison of experimental data with numerical results from the heat transfer model (a) top NW B2 at location 5 (b) top NW B3 at location 6 (c) bottom NW B1 from location 5 to 6. .... 77
- Fig. 5.15: Binary mask obtained from grayscale CCD image. This mask was used to select pixels corresponding to NW locations, and to eliminate pixels corresponding to areas without NWs. .... 78
- Fig. 5.16: (a) TR image at  $1 \mu\text{s}$ ; (b) Binary image created from (a), showing all pixels with  $\Delta T$  greater than or equal to  $8\text{K}$ . The binary image is used to calculate the approximate number of hotspots within the network. .... 80
- Fig. 5.17: AFM image showing configuration of a representative NW-NW junction (a) 2-D view; (b) (c) 3-D views from two different angles; (d) Height profiles for this NW pair. .... 81
- Fig. 5.18: A resistor network representing current conducting pathways in silver NW network. .... 82
- Fig. 5.19: (a) Pulse temperature rise at NW-NW junction; (b) the broader temperature profile (blue Gaussian curve) resulting from optical diffraction as captured by the  $100\times$  objective lens showing underestimation of temperature. Histogram (shown in red) is estimated by averaging the Gaussian temperature curve at each pixel. .... 84
- Fig. 6.1: Transient response (i.e. TR images) at different  $\tau_{DS}$  showing formation of hotspots during heating cycle at (a)(b)  $1 \mu\text{s}$ , and (c)(d)  $10 \mu\text{s}$  for silver NW and hybrid network respectively. The dotted lines represent the inner and the outer circular electrical contacts respectively. .... 88

- Fig. 6.2: Comparison of  $\Delta T$  vs.  $\tau_D$  profiles of two hotspots at comparable distances in the silver NW and hybrid network during the (a) heating cycle (b) cooling cycle. 89
- Fig. 6.3: Comparison of (a)  $A_H$  vs distance  $r$  from the center of the inner electrical contact; (b)  $A_C$  vs  $r$ ; (c)  $\tau_H$  vs  $r$ ; (d)  $\tau_C$  vs  $r$  in silver NW and hybrid network.  $r < 40 \mu\text{m}$  and  $r > 140 \mu\text{m}$  represent the inner and the outer electrical contact regions respectively. .... 91
- Fig. 6.4: Binary images at  $\tau_D = 10 \mu\text{s}$  in (a) silver NW network, and (b) hybrid network. Binary images are created from TR images, showing all pixels with  $\Delta T$  greater than or equal to 5K. The binary images are used to calculate the approximate number of hotspots within the network. The dashed lines denote the inner and the outer circular electrical contacts. .... 92
- Fig. 6.5: Comparison of number of hotspots vs time  $\tau_D$  in silver NW and hybrid networks. .... 93
- Fig. 6.6: Comparison of average hotspot temperature change ( $\Delta T$ ) vs time  $\tau_D$  in silver NW and hybrid networks. .... 94
- Fig. 6.7: Schematics showing the correlation of ANN ratio with spatial clustering. .... 95
- Fig. 6.8: Schematics of (a) binary images to be created from TR images showing different hotspots at a certain time instant  $\tau_D$ ; (b) borderlines of the hotspots are shown in red and mutual distances are shown in yellow lines; (c) Nearest neighbor distances of individual hotspots are shown in blue. .... 96
- Fig. 6.9: Evolution of (a) average nearest neighbor distance  $DO$  ; (b) expected mean distance given a random pattern  $DE$  ; (c) ANN ratio with time  $\tau_D$ . .... 97
- Fig. 6.10: Comparison of average  $\Delta T$  of the NWs within the channel region of silver NW network and hybrid network. .... 98

- Fig. 6.11: Comparison of temperature histograms of NW pixels within silver NW network and hybrid network at (a)  $\tau_D = 200$  ns, and (b)  $\tau_D = 10$   $\mu$ s. .... 99
- Fig. 6.12: Circuit simulation of a resistor network showing two parallel current conducting pathways in a silver NW network (configuration 1). Eight hotspots (HS 1-8) are represented by the eight resistive links (shown in red circles). ..... 103
- Fig. 6.13: Circuit simulation of the resistor network (configuration 2) with two hotspots (HS 1 and 4) removed by adding more parallel conducting pathways through resistors (shown in green) to represent current conduction pathways in hybrid network. Moreover, graphene provides additional connectivity between the two parallel current conducting pathways (shown in pink) in hybrid network. .... 104
- Fig. 6.14: Circuit simulation of the resistor network (configuration 3) with an additional current conducting pathway created through an additional resistor network (shown in yellow). ..... 105
- Fig. 6.15: Electrical power at each of the hotspots. Two of the hotspots (HS 2 and 3) show higher power in hybrid network compared to silver NW network whereas other hotspots (HS 5 – 8) show lower values. .... 106
- Fig. 6.16: AFM images showing configuration of representative NW-NW junctions in silver NW network and hybrid network. (a)(b) 2-D views; (c) - (f) 3-D views from two different angles of NW-NW junctions in silver NW and hybrid network respectively. In hybrid network, graphene wraps the NW-NW junction. .... 106
- Fig. 6.17: (a) Length profiles from AFM images of a representative NW-NW junction in hybrid network show graphene draping  $\sim 50$  nm on both sides of a NW. (b) Schematics along the cross-section of a NW showing graphene draping on both sides of the NW. .... 107

- Fig. 7.1: Binary mask obtained from grayscale CCD image. This mask was used to select pixels corresponding to NW locations, and to eliminate pixels corresponding to areas without NWs. .... 112
- Fig. 7.2: Probability density function  $f$  vs.  $\Delta T$  at various time instants over local self-heating time regime at (a) 200 ns, (b) 400 ns, and (c) 800 ns. (d)  $\log(f)$  vs.  $\Delta T$  at various time instants to take a closer look at the tail of the temperature distributions. (e)  $\log(-\log(1-F))$  vs.  $\log(\Delta T)$  at various time instants showing straight lines (signature of Weibull distributions). .... 113
- Fig. 7.3: Over the local self-heating time regime, evolution of (a) shape parameter (b) scale parameter with time. .... 114
- Fig. 7.4: Probability density function  $f$  vs.  $\Delta T$  at various time instants over heat diffusion time regime at (a) 20  $\mu\text{s}$ , (b) 50  $\mu\text{s}$ , (c) 160  $\mu\text{s}$ , and (d) 400  $\mu\text{s}$ . (e)  $\log(f)$  vs.  $\Delta T$  at various time instants to take a closer look at the tail of the temperature distributions. (f)  $\log(-\log(1-F))$  vs.  $\log(\Delta T)$  at various time instants showing straight lines (signature of Weibull distributions). .... 116
- Fig. 7.5: Over the heat diffusion time regime, evolution of (a) shape parameter (b) scale parameter with time. .... 117
- Fig. 7.6: (a) Device structure for self heating Simulation of silver thin film. (b)  $\Delta T$  profile at 10  $\mu\text{s}$ . (c)  $\Delta T$  vs. distance for different  $\tau_D$  s from 200 ns to 10  $\mu\text{s}$ . (d)  $\Delta T$  vs. time for different spatial locations. (e) pdf at 10  $\mu\text{s}$ . (f)  $\log(-\log(1-F))$  vs.  $\log(\Delta T)$  at 10  $\mu\text{s}$ . .... 120
- Fig. 7.7: Simulation results of heat diffusion through silver film (a)  $\Delta T$  profile at 450  $\mu\text{s}$ . (b)  $\Delta T$  vs. distance for different  $\tau_D$  s from 10  $\mu\text{s}$  to 450  $\mu\text{s}$ . (c)  $\Delta T$  vs. time for different spatial locations. .... 122

Fig. 7.8: Probability distribution function at different time instants (a)  $\tau_D = 20 \mu\text{s}$ , (b)  $\tau_D = 50 \mu\text{s}$ , (c)  $\tau_D = 160 \mu\text{s}$ , and (d)  $\tau_D = 400 \mu\text{s}$ . ..... 123

Fig. 7.9:  $\log(-\log(1-F))$  vs.  $\log(\Delta T)$  at corresponding time instants of  $\tau_D = 20 \mu\text{s}$ ,  $50 \mu\text{s}$ ,  $160 \mu\text{s}$ , and  $400 \mu\text{s}$ . ..... 123

Fig. 7.10: Evolution of (a) shape and (b) scale parameter with time ( $0 - 450 \mu\text{s}$ ) as obtained from heat diffusion simulation within silver film. .... 124

## ABSTRACT

Sadeque, Sajia. Ph.D., Purdue University, May 2018. Electro-thermal Transport in Non-homogenous Network. Major Professor: David B. Janes.

Nano-structured networks have drawn attention as potential replacements for bulk-material approaches in applications including transparent conducting electrodes (TCEs). As TCEs, these systems can provide relatively low sheet resistances in the high optical transmission regime along with excellent mechanical flexibility. While percolation models have been developed to describe the general trends in sheet resistance and transmittance on nanowire density, prior experiments have not yielded details such as distributions of junction resistances and current pathways through the networks. Most experimental studies on nanostructured TCE properties have focused on large area steady state exploration of electrical and optical properties or more microscopic studies of single/few junctions within the networks. A more detailed and microscopic understanding of the conduction pathways is necessary to more completely understand the percolating transport in these network systems.

In this thesis, we fabricate high quality graphene-silver nanowire (NW) based hybrid TCE and use transient thermoreflectance (TR) imaging technique with high temporal (200 ns) and spatial resolution ( $\sim 200 - 400$  nm) that allows simultaneous characterization of time and spatial dependence of the local self-heating around NW-NW junctions. Hotspots arise from self-heating associated with applied bias and are spatially correlated with current pathways through the network. Moreover, these hotspots can potentially redistribute and/or turn off percolating conductive current pathways due to elevated temperatures and thus impose reliability concerns. The ability to image the formation of the microscopic hotspots due to local self-heating (i.e. associated with local current pathways through the microscopic regions) provides a means to semi-quantitatively

infer current pathways in these percolating systems. First, we investigate time dependent temperature rise at hotspots in hybrid network at low spatial resolution (i.e. each hotspot comprises multiple NW-NW junctions) that allows analysis of multiple hotspots residing in between the electrical contacts. We quantitatively determine the thermal time constants of the hotspots and show their dependence on different spatial locations within the network. Collectively, we decouple the temperature rise into separate contributions from local self-heating and heat spreading from the electrical contacts. As we identify the time regime when local self-heating at the hotspots is predominant, we focus on local self-heating (rather than heat spreading from contacts) for subsequent electro-thermal studies. Next, using high-resolution TR imaging in case of a silver NW network, we study microscopic hotspots corresponding to individual NW-NW junctions and show the temporal and spatial evolution of the temperature profiles along two crossing NWs. We quantify the local power generated at a hotspot (i.e. an individual junction) at steady state and the fraction of this power propagating along each constituent NW. We also compare material/composition dependence of hotspots (each containing multiple junctions) characteristics in terms of their transient electro-thermal response, number, average temperature, and spatial distribution by considering two random 2-D networks where different transport mechanism prevails: silver NW network (percolation) and graphene-silver NW hybrid network (copercolation). Finally, we do an extended study of temperature distributions (which can be described by Weibull distributions) in silver NW network that shows distinctive signatures (i.e. evolution of shape parameter with time) of local self-heating vs heat spreading through network. The ability to resolve the local self-heating with high temporal and spatial resolution uniquely enables a comprehensive understanding of electro-thermal response and current pathways in the distributed conductors.

## 1. INTRODUCTION

### 1.1 Non-homogenous Network based Transparent Conducting Electrodes and its Classification

This chapter gives an overview of the next generation transparent conducting electrodes including 1-D/2-D hybrid nanostructured networks as potential ITO alternatives. It also discusses the motivation of this work to understand the current conduction mechanisms and distribution of conductive pathways/resistive bottlenecks in non-homogenous network by means of self-heating. *The content of this chapter is taken from our previous publications in Nanophotonics [1] and IEEE Transactions on Nanotechnology [2], and thus copyrighted by Nanophotonics and IEEE.*

Transparent conducting electrodes (TCEs) are integral elements in many current and emerging electronic and optoelectronic components, including touchscreens, photovoltaics, displays, thin film transistors (TFTs) and OLEDs (organic light emitting diodes) [3]. Currently, transparent conductive oxides (TCOs) are the most widely used materials for TCEs. While indium tin oxide (ITO) is the most common, TCOs of interest include fluorine doped tin oxide (FTO) and metal doped zinc oxides (such as Aluminum doped zinc oxide (AZO)). A relatively large band gap and a very high concentration of free electrons (typically  $> 10^{20} \text{ cm}^{-3}$  in the conduction band) ensure that TCOs have excellent optical transmission and relatively high electrical conductance, respectively [4, 5]. The technology is mature and mass-production of TCO-coated glass (thousands of tons/day) for a broad range of product categories is routine.

Unfortunately, TCOs have several limitations: First, there appears to be a fundamental tradeoff between carrier concentration and optical absorption, with the dopants or defects required for high carrier concentrations contributing to increased optical absorption [6, 7]. In particular, the n-doping of TCOs arises from intrinsic defects or external doping – these in turn lead to strong absorption in Infra-red regions of the spectrum – limiting the overall transmission of 85-90%. This may be sufficient for touch-screens,

but photovoltaic (PV) technologies could benefit from higher performance alternatives. Second, in addition to conventional Moore's scaling (for high speed/performance computing), 'More-than-Moore (MtM) technology' approaches will require flexible and transparent electronics/optoelectronics for applications such as flexible displays and touchscreens [8, 9]. ITO must be sufficiently thick to meet the conductivity requirement, making it difficult to fabricate it as a flexible film. Third, there is limited abundance of elements such as Indium; therefore, massive deployment of thin-film PV technology is possible only if an alternative to TCOs is found. These emerging requirements of higher performance, flexibility, earth-abundant supply, and most importantly, the high cost of TCOs have led to extensive research into alternate TCE materials, including nanostructured materials. In our publication [1], we provided a detailed overview of reported TCEs along with performance comparisons of ITO and other non-homogenous nanostructured network based TCEs.

*The first generation of TCO-alternatives is based on non-homogenous Metal nanonets:* A number of two-dimensional non-homogenous networks of nanostructured elements have been reported, including metallic nanowire (NW) networks consisting of silver NWs, metallic carbon nanotubes (m-CNTs), copper NWs, gold NWs and metallic mesh structures [10-14]. In these single-component systems, it has generally been difficult to achieve sheet resistances that are comparable to ITO at a given broad-band optical transparency, particularly in the high sheet conductance/high optical transmittance regime.

*The second generation of TCO-alternatives is based on coperculating networks:* A relatively new third category of non-homogenous network based TCEs consisting of non-homogenous networks of 1D-1D and 1D-2D nanocomposites (such as silver NWs and CNTs, silver NWs and polycrystalline graphene, silver NWs and reduced graphene oxide, graphene-silver NWs-graphene) have demonstrated TCE performance comparable to, or better than, ITO [15-17]. In such networks, coperculation between the two components can lead to relatively low sheet resistance at NW densities corresponding to high optical transmittance. This class is often denoted as 'hybrid networks'.

Schematically the three generations of TCEs are shown in Fig. 1.1. 1st generation are the TCOs: The TCOs are homogenous ohmic conductors e.g. current flows uniformly between the electrical contacts. 2nd generation are 1D metal nanonets and 2D graphene based percolating network: The nanonets and graphene both involve conduction through percolating network: the electrons hop from one stick to the next in a nanonet conductor, while they go around the high-resistance grain-boundaries in typical polycrystalline

graphene grown in CVD process. 3rd generation are the 1D-1D and 1D-2D based copercolating network: The copercolating network integrates both approaches, and creates a TCO-like conductor with very low percolation threshold.

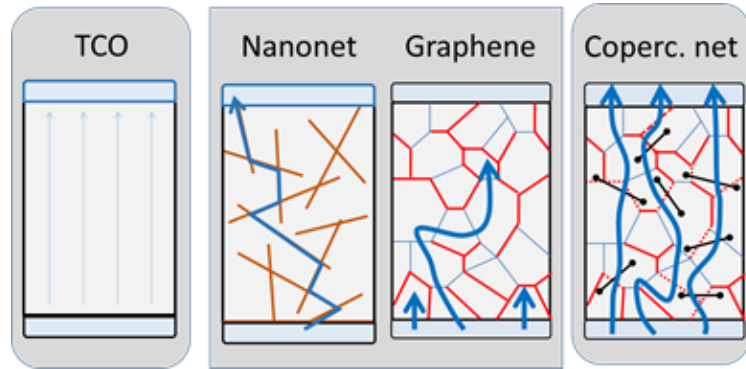


Fig. 1.1: Three generations of TCEs (figure is taken from [1]).

## 1.2 Graphene-Silver Nanowire Copercolating Hybrid Network

Non-homogenous nanostructured TCEs based on copercolating hybrid networks integrating single-layer graphene (SLG) and a silver NW network been reported with low sheet resistance ( $\sim 13\text{-}20 \Omega/\square$ ) at 85-92% optical transmission at 550nm wavelength, along with excellent mechanical strength and chemical stability [18, 19]. In this kind of copercolating hybrid 1D-2D structure, transport bottlenecks within the graphene or silver NW network (high-resistance grain boundaries and NW-NW junction resistance, respectively) are circumvented by one another (graphene grain boundaries are bridged by silver NWs and NW-NW junctions are bridged by graphene). The hybrid material, thus, provides sheet resistance versus transparency characteristics superior to either individual material and comparable (or even superior) to traditional TCOs [20]. As explained in [19], these hybrid networks should not be viewed as two noninteracting conductors in parallel since the observed resistances are significantly lower than the parallel combination of the resistances of the two components measured individually. Together, these elements mutually erase the percolating bottlenecks and reduce the overall percolation threshold as shown in details in [19] for copercolating systems of graphene-silver NW (solution cast). The resistance of the hybrid is lower than the individual films – this is an example of percolation engineering. This is why the figure of merit of copercolating hybrids behave as if they are classical thin-

films, except with much higher performance. As shown in [20], for coperculating systems like graphene-copper nanotrough roll-to-roll network, graphene-silver NW roll-to-roll network, sheet conductance changes linearly with thickness, which is a characteristics of thin film conductors. On the contrary, silver NW based random networks show significant change in sheet conductance beyond threshold thickness (density) [10, 21-23].

### **1.3 Current and Heat Transport in Homogenous and Non-homogenous Network**

As with many nanostructured approaches based on randomly deposited nanomaterials, non-homogenous networks (i.e. silver NW network and graphene-silver NW hybrid network) are spatially inhomogeneous at length scales ranging from the NW diameter ( $\sim 90$  nm) to the mm range. The inhomogeneity exists at two levels: (1) current flows selectively through percolating/coperculating pathways (assuming the NW density is above the percolation threshold) and (2) the resistance varies across the percolation paths, with the average resistance of a NW-NW junction resistance much larger than the resistance along a NW body. Fig. 1.2 illustrates the spatial homogeneity of traditional TCO based TCE e.g. ITO thin film and spatial non-homogeneity of random silver NW network based TCE at different spatial scale.

Spatial inhomogeneity gives rise to spatially varying current conducting pathways as shown in Fig. 1.1 as well as non-uniform temperature profiles. When current flows through a conductor, self-heating occurs due to power dissipation. For the device, the overall power dissipation is  $P = I^2R$ , with  $I$  and  $R$  referring to overall device current and resistance, respectively. Unlike a homogeneous thin film (such as ITO), power dissipation is not spatially uniform in non-homogenous networks. Local Joule heating based on local current within pathways gives rise to spatially-varying  $\Delta T$  (temperature difference between NW-NW junction and surrounding medium). Due to high resistivity of the NW-NW junctions, the Joule power is maximum there and microscopic hotspots are formed at the junctions. In contrast, such hotspots are not generally observed in homogeneous conductors. This is illustrated in Fig. 1.3 where ITO based heater shows uniform heating whereas silver NW network shows hotspots. These hotspots may lead to further increase of NW-NW junction resistance resulting in super Joule heating [24], temporary discontinuity and/or rerouting of a percolation path, and possibly permanent local damage of the material. In general, these transport phenomena are not observed in homogeneous conductors.

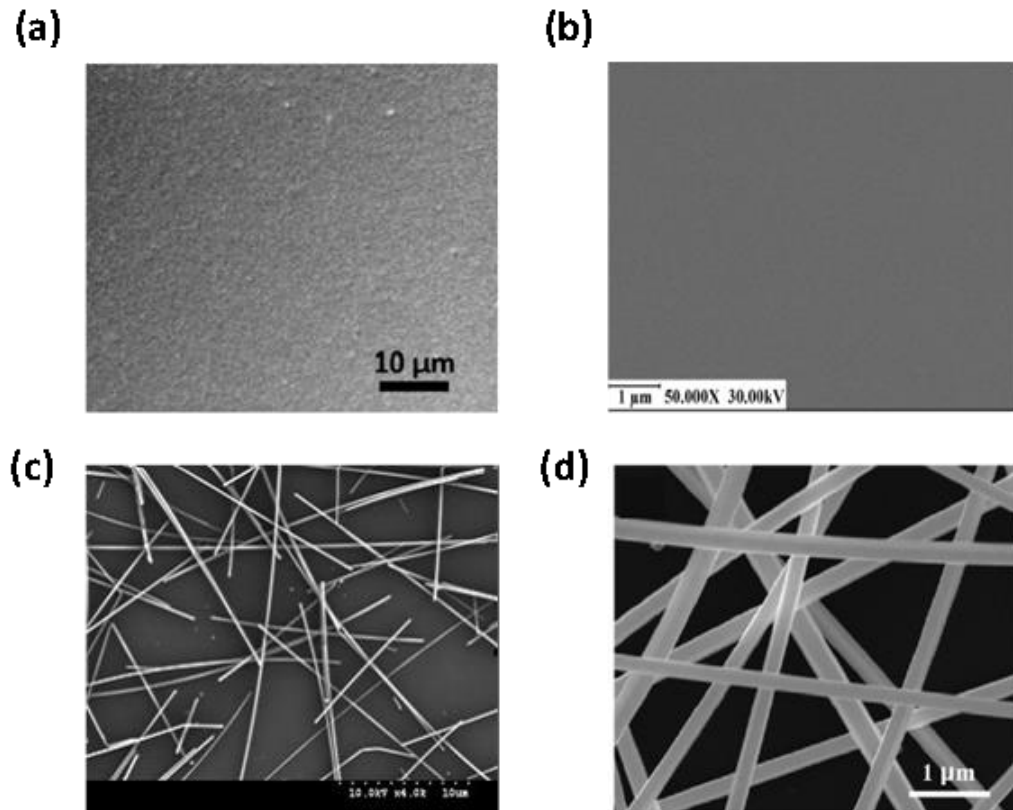


Fig. 1.2: (a) and (b) Homogeneous TCE e.g. ITO at different visual scales; figures are taken from [25] and [26] respectively; (c) and (d) Non-homogeneous TCE e.g. silver NW network at different visual scales; figures are taken from [27] and [28] respectively.

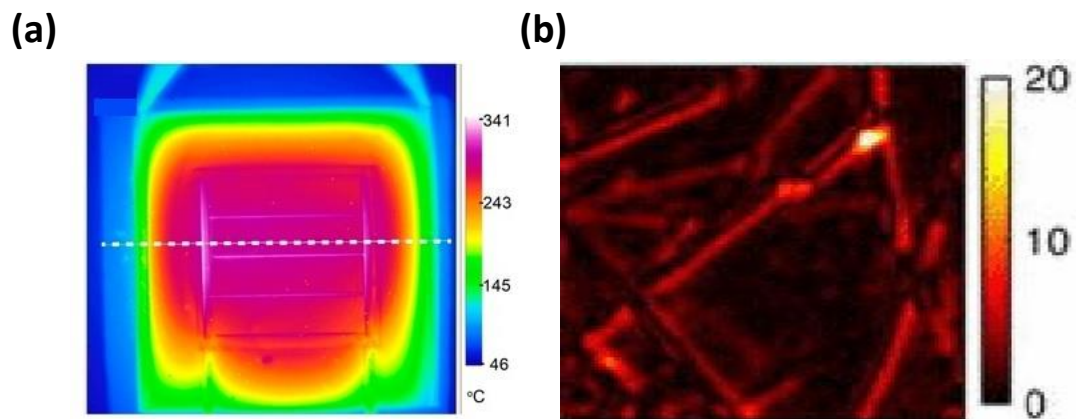


Fig. 1.3: (a) Uniform heating in homogenous conductor (e.g. ITO heater); figure is taken from [29] (b) Non-uniform heating (hotspot formation) in non-homogeneous network [24].

## 1.4 Electro-thermal Conduction in Non-homogeneous Network

While percolation network theories can include the effects of randomness on the macroscopic conductance of such systems, a more comprehensive picture of microscopic processes such as current pathways is required in order to understand the conduction properties as a function of spatial location and time. Since direct measurements of current at each spatial location (or even at the NW-NW junctions) of a network is experimentally challenging, alternative approaches, for example, temperature rise due to self-heating (i.e. electro-thermal response) can be taken as a method to probe current at different spatial locations (specially at the NW-NW junctions) within a network. As shown in Fig. 1.4(a), temperature rise at a junction ( $\Delta T_{\text{Junction}}$ ) and the current flowing through that junction ( $I_{\text{Junction}}$ ) are related by the power generated at that junction ( $P_{\text{Junction}}$ ) as explained through the following equations.

$$P_{\text{Junction}} = I_{\text{Junction}}^2 R_{\text{Junction}}$$

$$\Delta T_{\text{Junction}} = P_{\text{Junction}} \theta_{\text{TH Junction}}$$

Here,  $R_{\text{Junction}}$  and  $\theta_{\text{TH Junction}}$  are the electrical and thermal resistance of the NW-NW junction respectively. Moreover, as illustrated in Fig. 1.4(b), since the maximum heating occurs at the weakest (i.e. the most resistive) links in the most conducting pathways, by comparing  $\Delta T_{\text{Junction}}$  of two junctions (where hotspots are formed), it is possible to semi-quantitatively determine the currents flowing through those junctions using the above two equations. The assumption here is that the electrical and thermal resistances of the junctions are similar which is generally the scenario after the annealing process of the non-homogenous networks.

Most of the earlier heat-related studies of non-homogenous network focused on large area monitoring of temperature profiles as shown in Fig. 1.5(a) and (b). Recently, few studies have been reported relating temperature and current flowing, either through the entire network (Fig. 1.5(c)) or through one / few junctions (Fig. 1.5(d)). However, in most cases, the spatial resolution is in the “mm” range and the temporal resolution in “second” or “minute” range. A more detailed study is needed to learn about the coupled dynamics of temperature-current at multiple NW-NW junctions simultaneously, under the same bias conditions, and with high spatial and temporal resolution, but with a larger field of view of the thermal images so that the connection between the macroscopic and microscopic aspects can be comprehended.

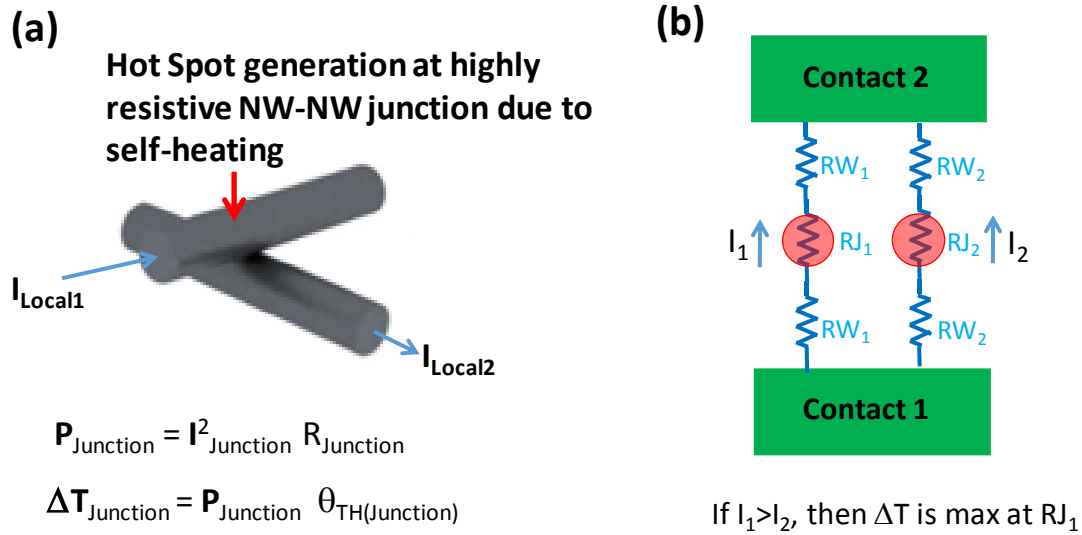


Fig. 1.4: (a) Temperature rise due to self-heating (i.e. electro-thermal response) at a hotspot can be used to probe the current at the NW-NW junction; (b) The maximum heating occurs at the weak links in the most conducting paths.

The steady-state temperature profile associated with self-heating in percolating and copercolating non-homogenous networks has been reported previously [24, 30], but transient response has not been investigated in detail. In this work, we aim to study the thermal response taking “time” as a tool to probe the electro-thermal response of hotspots in network based systems.

From reliability point of view, since local hotspots could potentially shut off and/or redistribute the conduction pathways [30-33] and damage the network locally due to elevated temperature, the study of the time evolution of the hotspots and the knowledge of the heat dissipation dynamics are important, not only to gain invaluable insights about the physics of electrical conduction, but also to ensure the reliability of the network over time.

From TCE perspective, while nanostructured networks, particularly the copercolating networks, can provide impressive TCE performance as well as the other characteristics, there are a number of open questions that must be addressed before this class of materials are suitable for widespread use. Most of the reported studies to date have focused on overall sheet resistance versus transmittance relationships. Studies on the microscopic conduction physics have shown spatial inhomogeneity on size scales ranging from the nanoscale to hundreds of microns, as well as local behavior that is different than

macroscopic behavior. A complete understanding of the microscopic conduction physics will be essential in understanding the overall impact on the properties of devices employing these materials. This thesis aims to answer some of these questions.

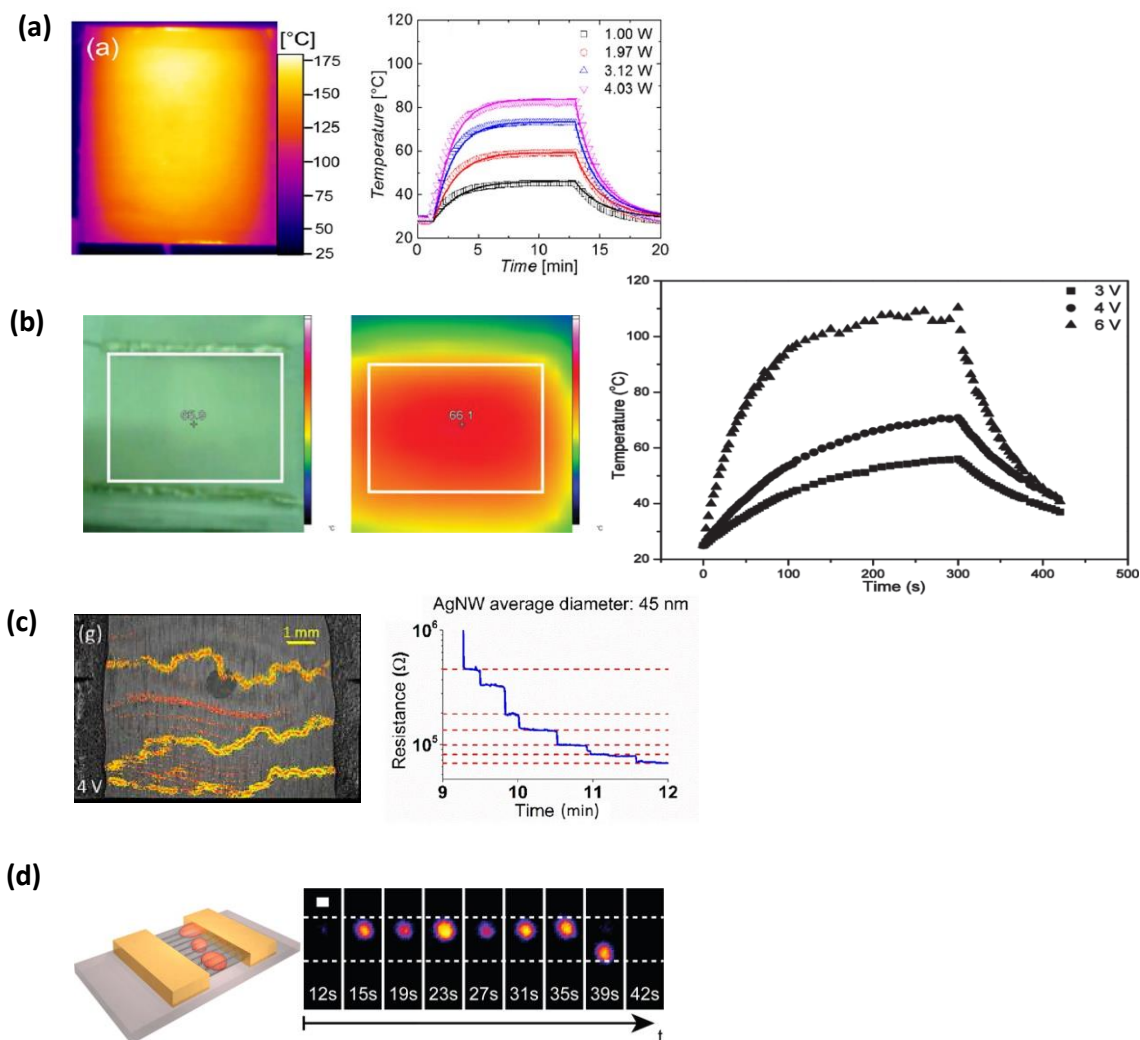


Fig. 1.5: Different methods to characterize transient heat dynamics. (a)-(c) Silver NW networks using Infra-red thermography, spatial resolution in ‘mm’ range. Figures are taken from [34], [35], and [32] respectively. (d) CNT networks using inverted optical microscopy, spatial resolution in ‘ $\mu\text{m}$ ’ range; figure is taken from [36]. In all cases, temporal resolution is in ‘s’ or ‘min’ range.

## 1.5 Organization of Thesis

The thesis is organized in the following way:

In **Chapter 2**, we compare performances of different non-homogenous random networks as transparent conductors and discuss the applicability of bulk approaches in explaining the observed macroscopic behavior of overall sheet resistance and transmittance with thickness.

In **Chapter 3**, we discuss the fabrication steps of two different types of non-homogenous networks (silver NW network and graphene-silver NW hybrid network) and details of transient thermal measurement (i.e. thermoreflectance imaging) techniques.

In **Chapter 4**, we describe the electro-thermal conduction through graphene-silver NW hybrid network as a function of time in order to quantify the dynamics of hotspots. We determine the thermal time constants and show how they vary with distance at different spatial locations within the network. We develop a heat diffusion model to understand the physical origins of the thermal time constants and to explain the distance dependency. We quantify the time domain over which temperature rise is dominated by the local self-heating of NW-NW junctions rather than due to other extrinsic factors.

In **Chapter 5**, we focus on obtaining high-resolution spatio-temporal profiles of temperature rise of the microscopic hotspots formed in the vicinity of NW-NW junctions due to local self-heating. Using a heat transfer model and the experimental NW temperature profiles, we determine the local power generated at the microscopic hotspots.

In **Chapter 6**, we explore composition/material dependent characteristics of hotspots by monitoring and comparing time dependent temperature rise, number of hotspots, average hotspot temperature, and their spatial distributions within two different types of random networks.

In **Chapter 7**, we demonstrate the temporal evolution of overall temperature distributions of NWs within such non-homogenous systems. We explain that the temperature distributions exhibit distinct characteristics of the dominant thermal process (local self-heating vs diffused heating from extrinsic source) occurring within the network.

**Chapter 8** provides a general summary and some closing remarks.

## 1.6 List of Associated Publications

The list of related publications is shown in Table 1.1.

Table 1.1: List of publications and their chapter relevance

Serial No	Publication	Chapter Relevance
1	<b>Sajia Sadeque</b> , S.R. Das, Takashi Ikuta, Kazuhiko Matsumoto, M. Alam and David B. Janes “Optical Haze Studies of Single Layer Graphene/Silver Nanowire Hybrid Transparent Conducting Electrodes”, presented at Electronic Materials Conference (EMC), 2014.	-
2	<b>Sajia Sadeque</b> , Y. Gong, K. Maize, A. Shakouri and David B. Janes “Transient Thermal response of Graphene/Silver Nanowire Hybrid Transparent Conducting Electrodes using Thermo-reflectance Imaging”, presented at Electronic Materials Conference (EMC), 2015.	4
3	K. Maize, S. R. Das, <b>Sajia Sadeque</b> , A. M. S. Mohammed, A. Shakouri, David B. Janes and M. Alam, “Super-Joule heating in Graphene and Silver Nanowire Network”, Appl. Phys. Lett. 106, 143104, 2015.	-
4	<b>Sajia Sadeque</b> , Y. Gong, K. Maize, A.K. Ziabari, A. Shakouri and David B. Janes “Radial Dependence of Self-Heating Time Constants in Graphene-Silver Nanowire Hybrid Transparent Conducting Electrodes”, presented at Electronic Materials Conference (EMC), 2016.	4
5	S. R. Das, A. M. S. Mohammed, K. Maize, <b>Sajia Sadeque</b> , A. Shakouri, David B. Janes and M. Alam, “Evidence of Universal Temperature Scaling in Self-Heated percolating Networks ”, Nano letters 16.5 (2016): 3130-3136	7
6	<b>Sajia Sadeque*</b> , S.R. Das*, C. Jeong, R. Chen, M. Alam and David B. Janes “Copercolating Networks: An Approach for Realizing High-Performance Transparent Conductors using Multicomponent Nanostructured Networks.”, Nanophotonics, 2016.	2

Serial No	Publication	Chapter Relevance
7	<b>Sajia Sadeque</b> , A. Candadai, Y. Gong, K. Maize, A.K. Ziabari, A. M. S. Mohammed, A. Shakouri, T. Fisher and David B. Janes “Thermal Transient Response of Microscopic Hotspots in Silver Nanowire Transparent Conducting Electrodes, EMC 2017.	5
8	<b>Sajia Sadeque</b> , A. Candadai, Y. Gong, K. Maize, A.K. Ziabari, A. M. S. Mohammed, A. Shakouri, T. Fisher and David B. Janes “Thermal Transient Response of Microscopic Hotspots in Silver Nanowire Network Conductors”, in review, 2018	5
9	<b>Sajia Sadeque</b> , Y. Gong, K. Maize, A.K. Ziabari, A. M. S. Mohammed, A. Shakouri and David B. Janes “Transient Thermal response of Hotspots in Graphene-Silver Nanowire Hybrid Transparent Conducting Electrodes”, IEEE Transactions on Nanotechnology, 2018.	4
10	“Comparative Studies of Transient Thermal Response of Hotspots in Graphene-Silver Nanowire Network and Silver Nanowire Network”, (In preparation)	6
11	“Time Dependent Temperature Distributions in Silver Nanowire Network”, (In preparation)	7

## 2. COPERCOLATING NETWORKS: AN APPROACH FOR REALIZING HIGH PERFORMANCE TRANSPARENT CONDUCTORS USING MULTI-COMPONENT NANOSTRUCTURED NETWORKS

### 2.1 Overview

In this chapter, we provide an overview of reported non-homogenous multi-component hybrid (i.e. copercolating) networks, including a comparison of the performance regimes achievable as transparent conducting electrode (TCE) materials with those of homogenous conductors (e.g. ITO) and single-component (i.e. percolating) non-homogenous networks. The performance is compared to that expected from bulk thin-films and analyzed in terms of a physical model. *The content of this chapter is taken from our previous publication in Nanophotonics [1], and thus copyrighted by Nanophotonics.*

### 2.2 Performance Comparison of Thin-Film and Nanostructured Network Based TCEs

#### 2.2.1 Selection of Representative Studies

A number of studies have been published for each class of TCEs described in Chapter 1 [10-17, 19-21, 23, 37-45]. In order to allow qualitative and quantitative comparison among the performances of the three classes, representative studies from each class have been selected. In this analysis, representative publications are chosen based on (i) performance (transmittance ( $T$ ) versus sheet resistance ( $R_S$ ) relationship) that is representative of high-quality results within the class, (ii) availability of a complete set of data (thin film thickness ( $t$ ), nanowire (NW) density/thickness,  $T$ ,  $R_S$  or conductivity/resistivity), and, (iii) a sufficiently large thickness range, allowing meaningful interpolation or extrapolation of  $T$  over a range of ~70-90%. In general, a variety of results have been obtained within a given class, corresponding to different deposition techniques, width and length of NWs, or post-processing techniques [19, 37-41]. Most of the studies account for the optical properties of the substrate, typically by correcting for the substrate

reflectance and normalizing the measured  $T$  values to those measured for the substrate (to compensate for substrate loss).

The classes of TCE and representative studies are the following:

### I. Indium Tin Oxide

ITO is a widely used TCO and is chosen as a representative material for TCOs. While materials such as AZO and FTO have shown somewhat lower sheet resistance at a given optical transmittance (compared to ITO) [22, 23], the transmittance versus thickness and sheet resistance versus thickness relationships are expected to be qualitatively similar to those of ITO.

a. *Peumans, et al.* [42], denoted as “ITO Theory”. The authors simulate  $T$  and  $R_S$  of ITO thin-films based on “optical constants for e-beam deposited ITO acquired using spectroscopic ellipsometry.” Since ITO performance varies widely depending on processing details and a widely accepted empirical dataset is not available, this theoretical dataset is used by many groups to compare the performance of new TCEs. Unfortunately, the paper does not specify film thickness explicitly.

b. *Benoy, et al.* [43], denoted as “ITO Benoy”. This experimental study presents a complete data set ( $t$ ,  $R_S$ ,  $T$ ) for a range of thicknesses, ranging from 80 nm to 350nm. For this paper, it was not clear how the authors corrected for substrate reflection and multiple reflections. The data compares well with “ITO Theory” for the range of thickness reported; however, data regarding the low-resistivity regime is not available.

### II. Silver NW and CNT Nanotube Networks

a. *Ruiz, et al.* [21], denoted as “AgNW Ruiz”. This paper presents a complete set of data with good performance ( $R_S = 20.2 \Omega/\text{sqr}$  at  $T = 95\%$ ). Density,  $R_S$ ,  $T$  data all are provided along with NW dimensions. Several combinations of length and width are reported; the current analysis focused on a specific data set (length  $\sim 100 \mu\text{m}$  and width  $\sim 200 \text{ nm}$ ), which represents the highest performance.

b. *Colman, et al.* [23], denoted as “AgNW Colman”. This paper also presents a complete set of data, including  $R_S$  vs  $t_{eff}$ ,  $T$  vs  $t_{eff}$ ,  $T$  vs  $R_S$ . The reported NW parameters included length =  $6.6 \mu\text{m}$  and diameter =  $84 \text{ nm}$ . The effective thickness of the film,  $t_{eff}$ , will be defined in the next section.

c. *Lee, et al.* [44], denoted as “CNT Lee”. This paper presents a relatively complete set of data, including conductivity vs thickness and  $R_S$  vs  $T$ . The CNT dimensions (diameter, length) are not stated, and thickness data has not been provided for all data

points. Data points that are present in both conductivity vs thickness plot and  $R_S$  vs  $T$  plot are utilized in the current analysis.

### III. Hybrid Graphene/ NW Coperculating Networks

a. *Chen, et al.* [19], denoted as “Hybrid, Solution Cast”. Our prior study presented results on a high-performance hybrid network produced by drop-casting, along with an analysis of  $R_S$  extraction from circular transfer length measurement (TLM) test structures. The silver NWs had nominal length/diameter of 40  $\mu\text{m}$  and 100 nm and nominal NW densities were stated.

b. *Peng, et al.* [20], denoted as “Hybrid Graphene/AgNW R2R”. This publication presents a high-performance hybrid network, produced by roll-to-roll printing using a silver NW suspension with  $\sim 20 \mu\text{m}$  length and 30 nm diameter and nominal NW densities were stated.

c. *Peng, et al.* [20], denoted as “Hybrid Graphene/Nanotrough R2R”. In addition to the hybrid AgNW/graphene network, *Peng et al.* presented results for a hybrid structure consisting of a single layer of graphene and a 2-D network of copper nanotroughs. These samples exhibited very good performance, among the best  $R_S$  versus  $T$  performance reported to date, particularly in the low  $R_S$ /high  $T$  regime. In addition, this data set allows direct comparison to hybrid AgNW/graphene networks reported by the same authors. The dimensions and density of the Cu nanotroughs are not given.

#### 2.2.2 Comparison of Sheet Resistance versus Transmittance Performance

A direct comparison of the reported performances of various TCEs is illustrated in Fig. 2.1, which presents the  $T$  versus  $R_S$  (log scale) for the various data sets described in the previous section. The graph also includes the modeling result [42], which shows the predicted performance of ITO over a relative broad range of parameters. For data sets that present points at the same  $T$  ( $R_S$ ), a direct comparison can be made based on the corresponding values of  $R_S$  ( $T$ ). Of the TCE classes considered in this analysis, the hybrid samples, including graphene/AgNW and graphene/Cu nanotrough networks, exhibit the highest overall performance in the high  $T$  regime ( $T \sim 90\%$  and above). For both ITO and percolating networks, it has proven difficult to achieve comparable  $G_S$  values in the  $T > 90\%$  regime. The thicknesses dependences of  $G_S$  and  $T$  in these networks, along with a physical model for the  $G_S$  versus thickness dependence in a percolating network, will be discussed in later sections.

Note that the overall relationship between  $R_S$  and  $T$  is qualitatively different between various classes of TCEs. In order to allow comparison with the  $T$  vs  $R_S$  relationship expected for bulk thin films, and associated with a common definition of a figure of merit (FOM), curves are also shown for three values of the FOM, as stated in the caption. The specific dependences of  $T$  and  $R_S$  on  $t$  will be discussed in section 2.2.4, along with a description of the applicability of the FOM.

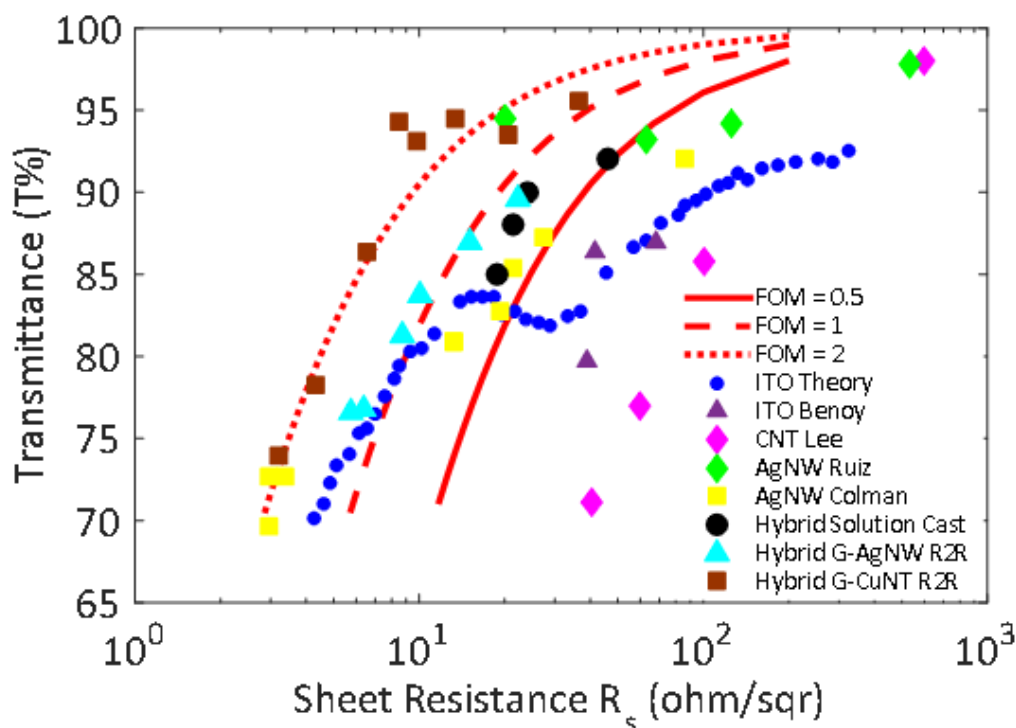


Fig. 2.1: Optical transmittance versus log of sheet resistance for representative studies on various types of transparent conductors. The various studies are summarized in the text.

### 2.2.3 “Effective” Thickness of Transparent Conducting Films

The performances of various TCE films may be compared – as we just did in Fig. 2.1– without specifying the film thickness. However, a deeper theoretical understanding of the data is possible when the information regarding thickness-dependence of transmission and resistance are available. As we will see below, for the new class of TCEs developed over the recent years, the notion of ‘thickness’ is not easy to define; nonetheless, a careful definition allows systematic and meaningful comparison of the dataset available.

Typically, in TCEs based on networks of nanostructures, the density of nanowires/nanotubes ( $D$ ) is presumed to correlate directly to the thickness of a bulk thin film ( $t$ ). The sheet conductance ( $G_S$ ) and optical transmittance ( $T$ ) are expected to follow, at least qualitatively, the respective bulk thin film dependencies on thickness. In order to allow a more direct comparison between various classes of materials, it is beneficial to define an effective thickness,  $t_{eff}$ , for each class of materials. Such a comparison provides a means to quantitatively compare the sheet conductance/transmittance behavior in various networks and to identify regimes in which the behavior deviates from the expected relationships for bulk thin films. For thin film TCOs, including ITO,  $t_{eff}$  is  $t$ , the actual thickness of the film. For percolating and coperculating networks, we define  $t_{eff}$  as the thickness of a uniform thin film of the same material (e.g., Ag in the case of Ag NW networks) containing the same number of atoms/cm<sup>2</sup> as the nanostructured network. Note that this definition considers the nanowire/nanotrough/nanotube component, but does not account for the 2-D layer (e.g. graphene).

For cases in which the authors have stated film thickness or a comparable quantity, the  $t_{eff}$  is determined from the parameters stated in Table 2.1. The  $t_{eff}$  is calculated for the various cases as follows:

a. AgNW Ruiz: Silver density  $D$  is given in g/m<sup>2</sup>. The  $t_{eff}$  is:  $1\text{ cm} \times 1\text{ cm} \times t_{eff} \times \rho = \frac{D\text{ (in g/m}^2\text{)}}{10000}$ .

b. AgNW Colman:  $t_{eff}$  is directly given. To show a smooth transition, one data point per  $t_{eff}$  has been taken.

c. Hybrid Graphene/AgNW Solution Cast: Silver NW density  $D$  is given in #of wires/cm<sup>2</sup>. The  $t_{eff}$  is calculated from:  $1\text{ cm} \times 1\text{ cm} \times t_{eff} \times \rho = \rho \times \text{total volume} = \rho \times D \left(\text{in } \frac{\text{\# of wires}}{\text{cm}^2}\right) \times \pi r^2 l$

d. Hybrid Graphene/AgNW R2R: Here silver NW density  $D$  is given in #of wires/mm<sup>2</sup>.  $D$  in #of wires/mm<sup>2</sup> is multiplied by 100 to convert to #of wires/cm<sup>2</sup>. The  $t_{eff}$  is calculated from:  $1\text{ cm} \times 1\text{ cm} \times t_{eff} \times \rho = \rho \times \text{total volume} = \rho \times D \left(\text{in } \frac{\text{\# of wires}}{\text{cm}^2}\right) \times \pi r^2 l$ .

The references ‘ITO Theory’ and ‘Hybrid Graphene/Nanotrough R2R’ do not report thickness and/or NW density, nor do they report dimensions of nanotroughs. In order to obtain  $t_{eff}$  for this case, we have assumed that the  $t_{eff}$  at  $T=70\%$  is the same as that calculated for ITO Benoy. Assuming  $G_S$  vs  $t_{eff}^*$  is linear, the  $t_{eff}$  value for a given point can then be directly calculated from the corresponding  $G_S$  value. In the case of Hybrid Graphene/nanotrough R2R, neither dimensions nor density is stated for the nanotroughs.

In order to obtain  $t_{eff}$  for this case,  $t_{eff}$  is estimated from the reported  $G_S$  values, assuming the same conductivity value ( $\sigma = 400000$  /ohm-cm) reported for individual nanotroughs. This assumption again implies an assumption that  $G_S$  vs  $t_{eff}^*$  is linear and yields  $t_{eff}$  at  $T=70\%$  that is in the same range as that calculated for hybrid AgNW/Graphene samples. Note that the corresponding values for  $t_{eff}$  listed in Table 2.1 (value at  $T = 70\%$ , shown in bold for these studies) are somewhat arbitrary. However, the relative values between various data points (used for normalized thickness, discussed below) are consistent with the corresponding reported  $R_S$  values reported in the respective papers.

#### 2.2.4 Physical Model for Bulk Material and Adaptation for Nanostructured Non-homogenous TCEs

In case of bulk material, the relation between transmittance ( $T$ ) and thickness ( $t$ ) of the material can be written as:

$$T = (\exp(-\alpha t))^2 \quad (2.1)$$

where  $\alpha$  is the absorption co-efficient. The relation between sheet conductance ( $G_S$ ) and  $t$  can be written as:

$$G_S \equiv R_S^{-1} = \sigma t \quad (2.2)$$

where  $\sigma$  is the dc conductivity of the material.

For most TCE applications, at least 70% of the light must be transmitted (i.e.  $T \geq 0.7$ ). This regime of interest corresponds to  $\alpha t \ll 1$ , so that Eq. (2.1) can be linearized as follows:

$$T \simeq 1 - 2 \alpha t \quad (2.3)$$

Assuming that comparable relationships apply for TCEs based on non-homogenous metallic NW/CNT networks and coperculating networks, Eq. (2.2) and Eq. (2.3) can be rewritten in terms of the effective thickness,  $t_{eff}$ , so that:

$$G_S \equiv R_S^{-1} = \sigma_{eff} t_{eff} \quad (2.4)$$

$$T \simeq 1 - 2\alpha_{eff} t_{eff} \quad (2.5)$$

where  $\sigma_{eff}$  and  $\alpha_{eff}$  are the corresponding effective electrical conductivity and effective absorption coefficient of the percolating/copercolating film. The “effective” designations refer to spatially average parameters, e.g., effective thickness of a random 2D NW network can be defined in terms of the average thickness over some macroscopic area, while the physical thickness of the layer will vary spatially on a microscopic scale (e.g., on a wire versus a gap in between wires). Strictly speaking,  $\sigma_{eff}$  and  $\alpha_{eff}$  are well defined only in the case where the behavior versus thickness follows the relationships in Eq. (2.4) and Eq. (2.5), respectively. Detailed electromagnetic simulations justify Eq. (2.5) for nanonets and metallic NW arrays [19, 46], but the justification of Eq. (2.4) will be considered more carefully in the next section. As discussed in this chapter, representative reports from percolating networks exhibit sheet conductances that deviate significantly from the relationship in Eq. (2.4) over the transmittance range of interest. In this case, it is not possible to define a single value of  $\sigma_{eff}$  that accurately describes the overall relationship. Even for copercolating networks that follow the relationship of Eq. (2.4), carrier mobility is not a meaningful quantity, since the carrier density within the network is not known, and conductance is limited by junctions rather than by bulk regions.

In order to represent various classes of materials on a single graph, we define a normalized effective thickness,

$$t_{norm} = \frac{t_{eff}(T)}{t_{eff}(T = 0.7)} \quad (2.6)$$

i.e., the thickness of the film at 70% transmission is taken as  $t_{norm} = 1$ . Fig. 2.2 and Fig. 2.3 present the  $T$  versus  $t_{norm}$  and  $G_S$  versus  $t_{norm}$  relationships, respectively, for the representative studies summarized in Table 2.1. For generating the data points, corresponding values of  $T$  at and above 70% have been considered. Actual experimental  $T$  and  $R_S$  data has been plotted against  $t_{norm}$ . If experimental  $T$  and  $R_S$  data (at  $T=0.7$ ) are available, those are used directly to calculate  $t_{norm}$ . In case, they are not available, experimental  $T$  is fitted with thickness  $t$  or  $t_{eff}$  with a straight line to infer the thickness  $t$  or  $t_{eff}$  at 70% transmission.

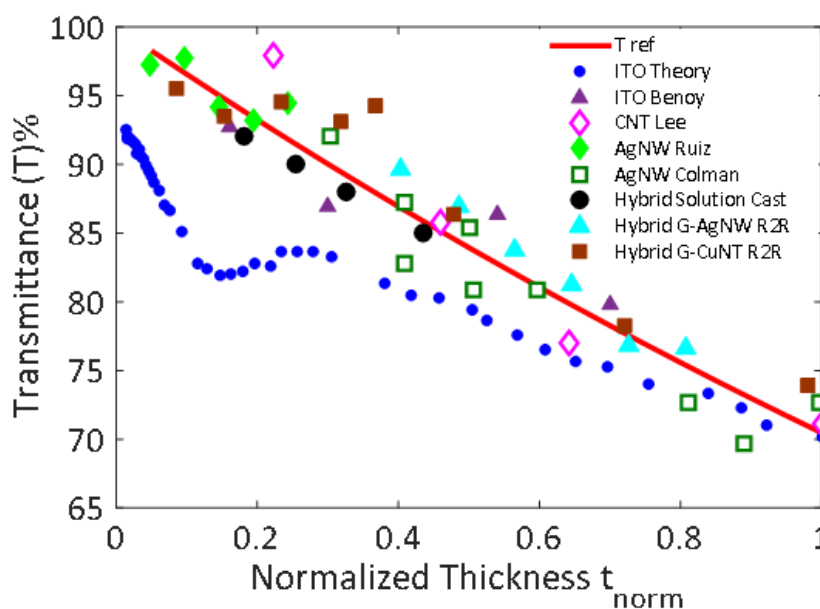


Fig. 2.2: Optical transmittance vs. normalized thickness for representative studies on various types of transparent conductors. A linear relationship (Eq. (2.5)) is also shown for reference. The various studies are summarized in the text.

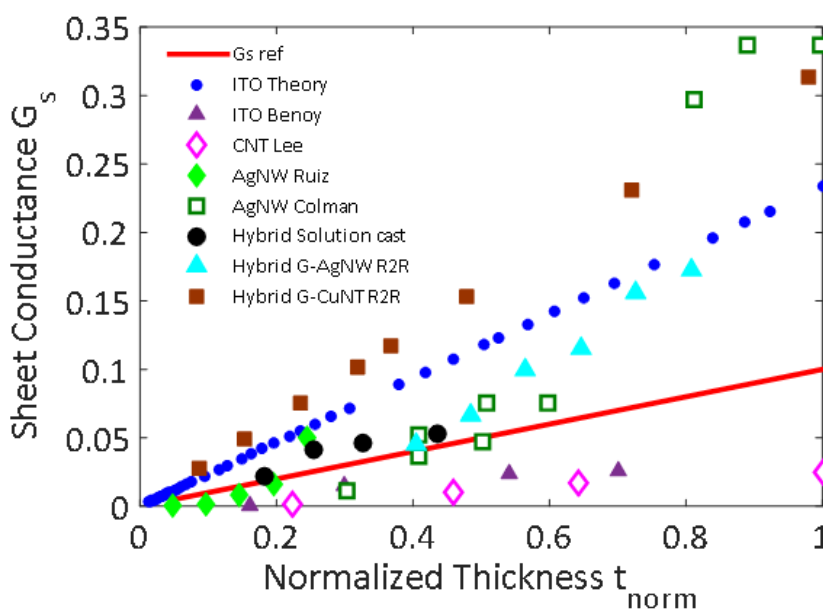


Fig. 2.3: Sheet Conductance versus normalized thickness for representative studies on various types of transparent conductors. A linear relationship (Eq. (2.4)) is also shown for comparison. The various studies are summarized in the text.

In Table 2.1, the value of  $t_{eff}$  corresponding to  $T = 0.7$  is shown, along with the thickness/density parameter reported in the corresponding paper. The  $t_{eff}$  values shown in bold correspond to samples in which density/thickness not provided. The  $\alpha_{eff}$  values obtained by fitting the reported transmittance versus effective thickness relationships over the range of reported values (effectively using Eq. (2.5)) are also shown. In the case of hybrid samples, a pre-factor corresponding to the transmittance of single-layer graphene is employed. The optical transmittance in the “ITO Theory” report does not follow the relationship in Eq. (2.5), so a single value for  $\alpha_{eff}$  is not suitable to describe the overall relationship.

Table 2.1: Comparison of  $t_{eff}$  for representative studies on various classes of TCEs

TCE type	$t_{eff}$ (nm) at 70% T	Density (wires/mm <sup>2</sup> )	Density (g/m <sup>2</sup> )	Thickness (nm)
ITO Theory	<b>500</b>			
ITO Benoy	500			80 - 350
AgNW Ruiz	6900		3.5 – 17.7	
AgNW Colman	210			64 - 532
Hybrid, Solution Cast	28	$2 \times 10^4 - 4.8 \times 10^4$		
Hybrid Graphene/ AgNW R2R	3.5	$2.5 \times 10^4 - 5 \times 10^4$		
Hybrid Graphene/ Nanotrough R2R	<b>8</b>			
CNT Lee	50			11 - 87

In case of the three classes of TCEs in our discussion, experimental data shows significant deviations from these equations. For transparent thin film coatings like ITO (e.g. ITO Theory [43]),  $G_S$  follows the classical equation, but  $T$  deviates at lower thickness regime ( $T$  actually goes down). Moreover, fitting of the  $T$  vs  $t$  data shows a pre-factor of 0.9 (instead of 1). Both these effects are likely related to the reflection loss due to multiple scattering from the backside of the material that becomes significant at the low thickness regime. The experimental study considered in this paper (ITO Benoy [43]) contains a relatively small number of data points, so this effect is difficult to observe. However, experimental reports considering a larger number of data points exhibit  $T$  vs  $t$  relationships that deviate from that presented in Eq. (2.3).

In case of percolating system like AgNW network (AgNW Ruiz [21] and AgNW Colman [23]),  $T$  follows the bulk equation showing a linear gradual decrease with  $t_{eff}$  as

expected, but  $G_S$  does not – rather it shows a sudden decrease in  $G_S$  as  $t_{eff}$  decreases. The reason behind this is straightforward: below the percolation threshold, the network components cannot form a continuous thin film, which is reflected in its poor sheet conductance,  $G_S$ . The  $t_{eff}$  value at which this occurs (corresponding to the percolation threshold) varies with NW dimensions and potentially with deposition technique.

For coperculating network systems (Hybrid, Solution Cast, Hybrid Graphene/Silver NW R2R and Hybrid Graphene/Nanotrough R2R), both  $T$  and  $G_S$  follow the classical equations, i.e.  $G_S$  increases and  $T$  decreases linearly with  $t_{eff}$ . Fitting of the experimental  $T$  vs  $t_{eff}$  shows a pre-factor of 0.97 (instead of 1). This number represents the transmission of monolayer graphene (97%) when  $t=0$ , i.e. when the NW network is absent. As will be discussed in detail in a later section, coperculation results in a linear  $G_S$  versus  $T$  relationship, even at  $t_{eff}$  values that would correspond to the “below percolation threshold” regime in single-component nanostructured networks.

### 2.2.5 Physical Validity of Typical Figure of Merit

From the discussions above, it can be stated that both thin film (ITO) and percolating networks deviate from expected bulk behavior for film thickness below a critical dimension (due to  $T$  effects for ITO and roll-off in  $G_S$  for percolating network). With ITO, it may not be possible to attain high  $T$  even if the  $G_S$  can be increased by doping or thickness. In the case of AgNW or CNT percolating networks, it may not be possible to get high  $G_S$ , if one wishes to retain high  $T$ . For photovoltaics applications, however, both  $T$  and  $G_S$  must be high simultaneously. Coperculating network systems like graphene/metal NWs and/or graphene/metal nanotrough bridge the gap and ensure high  $G_S$  (low  $R_S$ ) regime, without compromising high  $T$  (i.e. at lower  $t$ ).

A figure of merit (FOM) should allow comparison of the performance of different types of transparent electrodes. The comparison is valid only in the regime where the physical model that has been utilized to construct the FOM accurately describes the behavior of a given TCE. For percolating networks, such comparisons are valid only above the percolation threshold regime. In this study, we employ a modified Jain/Gordon figure of merit [7, 47], namely  $FOM \equiv \frac{\sigma_{eff}}{\alpha_{eff}}$ . This FOM is consistent with the physical model (e.g. Eq. (2.4) and Eq. (2.5)) discussed in the previous section. It should be noted that neither  $\sigma_{eff}$  nor  $\alpha_{eff}$ , in isolation, represent a valid figure of merit for a TCE; one must

consider the two together, along with a thickness range over which relationships comparable to Eq. (2.4) and Eq. (2.5) apply.

Besides comparing the performances of different TCEs, a useful FOM should also allow extrapolation of the behavior of a specific TCE over a broad  $t_{eff}$  regime, i.e., to accurately predict how  $T$  and  $R_S$  change as  $t_{eff}$  changes. For coperculating network systems, the thickness dependencies of both  $T$  and  $G_S$  follow the relationships presented in Eq. (2.4) and Eq. (2.5), so the  $FOM \equiv \frac{\sigma_{eff}}{\alpha_{eff}}$  is valid for a broader range of  $t_{eff}$ , specifically to the regime corresponding to  $T > 90\%$ . The presence of a second layer in the hybrid systems (e.g. graphene in the samples reported to date) introduces a pre-factor in Eq. (2.5), corresponding to the transmittance of the graphene layer. This is generally a perturbation on the expected  $T$  vs  $t_{eff}$  relationship, modifying the FOM extracted for the material but not qualitatively changing the  $T$  vs  $t_{eff}$  relationship. On the other hand, in case of percolating systems, within the regime below the percolation threshold,  $G_S$  falls rapidly as  $t_{eff}$  decreases. Therefore, a single  $\frac{\sigma_{eff}}{\alpha_{eff}}$  value cannot be valid for both the percolating and sub-percolating regime. Efforts have been made [22, 42] to define a different FOM for the regime below the percolation threshold. However, the traditional FOMs for TCEs, including the one considered in this study, can only quantify the behavior in the regime above the percolation threshold. While ITO generally follows a linear  $G_S$  versus thickness relationship over a large range of thicknesses, the  $T$  dependence deviates significantly from the expected relationship (Eq. (2.5)), due to reflection/multiple reflection effects. Because of this, ITO does not generally follow the overall relationship implied in the FOM. Therefore, different values of FOM will be extracted in various thickness regimes.

### 2.3 Conclusion

In this chapter, we have compared several different TCO-alternative technologies. While the  $T$  vs  $R_S$  relationship allows direct performance comparison between two data points, a more physical-based understanding of the potential performance requires consideration of the dependences of  $T$  and  $R_S$  on  $t_{eff}$ . We have discussed the importance of defining regimes over which a FOM is applicable, in order to allow meaningful comparison between various studies.

### 3. FABRICATION AND MEASUREMENT TECHNIQUES

#### 3.1 Fabrication of Non-homogenous Networks

In this section, we describe the fabrication steps of the two types of non-homogenous network used in this work: silver nanowire (NW) based percolating network and graphene-silver nanowire based hybrid network. *The content of this chapter is taken from our publication in IEEE Transactions on Nanotechnology [2], and thus copyrighted by Institute of Electrical and Electronics Engineers (IEEE).*

Fig. 3.1 illustrates flow chart of the basic fabrication steps. Silver NWs (purchased from Blue-nano, average diameter 90 nm, average length 40  $\mu\text{m}$ ) were drop-cast from solution on quartz substrates with a density, controlled by concentration of solution and number of drops. Four different types of samples are fabricated with NW densities ranging from  $\sim 2 \times 10^6$  to  $\sim 4.8 \times 10^6$  NW/cm<sup>2</sup> as shown in Fig. 3.2(c). From these, the networks with the highest density of NWs have been chosen for electro-thermal (i.e. transient thermoreflectance imaging, explained later) measurements. For hybrid network, SLG grown by chemical vapor deposition (CVD) (purchased from ACS materials) with an average grain size of 1  $\mu\text{m}$  was transferred over the NW network using wet transfer method. The samples were then annealed in forming gas at 300°C for 1 hour. Fig. 3.2(a) and (b) shows the schematics of the side view of the silver NW and hybrid samples respectively. Electrical contacts were fabricated by depositing Ti/Pd/Au with thicknesses of 1 nm/30 nm/20 nm, respectively, by electron-beam evaporation and patterning in a circular transmission-line model (TLM) geometry by photolithography and subsequent lift-off. The circular TLM configuration allows confinement of the current without the need to pattern the channel (e.g. for determination of sheet resistance), and also provides a geometry for current flow and heat spreading which can be used, with appropriate models, for comparison of the spatial dependencies of self-heating and heat spreading (Chapter 4). The choice of contact geometry (e.g. circular versus rectangular) impacts these quantities quantitatively due to different current distributions and heat source/flow geometries, but the qualitative behavior is expected to be comparable. The distance between the inner and the outer contact (i.e. the channel) is 100  $\mu\text{m}$ . A CCD image of hybrid network as captured by a 20x lens is shown in Fig. 3.3.

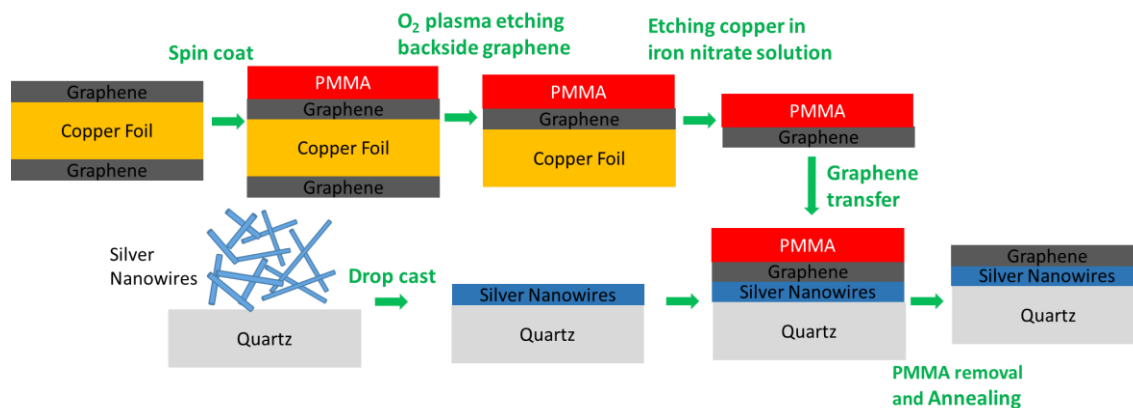


Fig. 3.1: Fabrication steps of silver NW and graphene-silver NW based hybrid non-homogenous network.

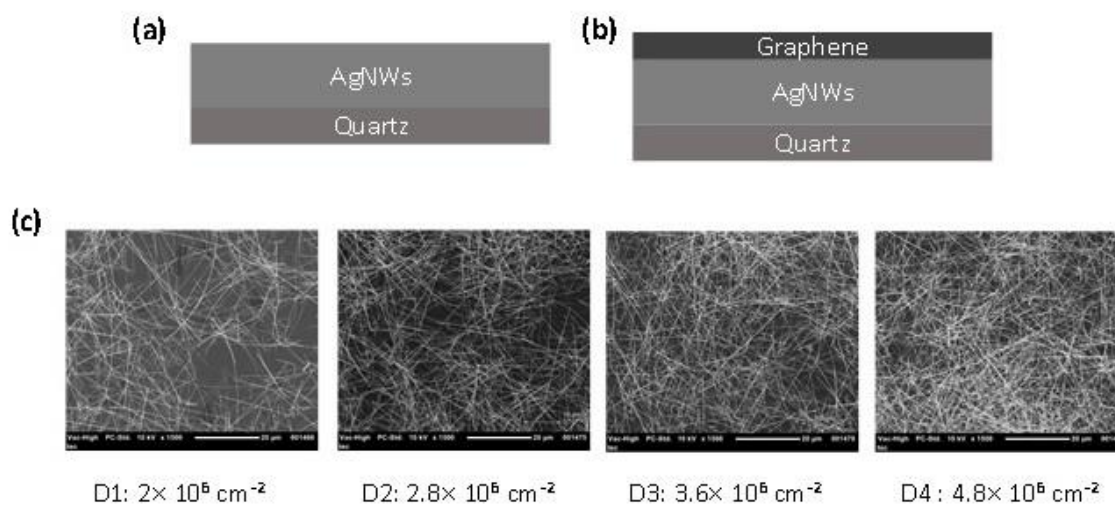


Fig. 3.2: (a) Schematics of silver NW network; (b) Schematics of graphene-silver NW hybrid network; (c) Samples prepared with 4 different densities of silver NWs.

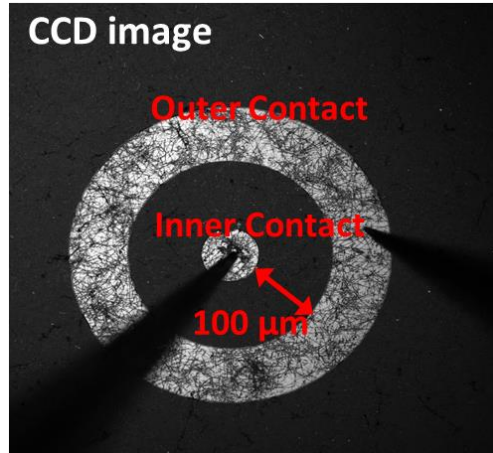


Fig. 3.3: CCD image of a hybrid network as captured by a 20x lens showing the concentric circular inner and outer electrical contact pads along with the electrical probes used for electro-thermal (i.e. transient thermoreflectance) measurements.

### 3.2 Transient Thermoreflectance Imaging Technique

In this work, we use high-resolution transient thermoreflectance (TR) imaging technique to understand electro-thermal response of non-homogenous networks. This imaging technique enables spatial mapping of the self-heating as a function of time following the application of a voltage pulse (heating cycle) or following the end of the voltage pulse (cooling cycle). Previously this technique has been used to obtain transient thermal characteristics of bulk material and devices like field-effect transistors, supercapacitors, thermo-electric materials, power transistors and micro-refrigerators [48-57]. Compared to other measurement techniques (e.g. inverted optical microscopy, infrared optical sensor etc.) that have been used to observe the dynamics of hotspot formation and/or current conducting paths in NW and CNT based system [36, 58] as shown in Fig. 1.5, TR imaging can provide high spatial and temporal resolution simultaneously, along with the ability to provide large field of view. With high-resolution TR imaging,  $\mu\text{s}$  resolution is achievable with fast scanning rate over a large region (more than  $600\ \mu\text{m} \times 600\ \mu\text{m}$ ) [59-62]. Moreover, TR method is contactless and thermal images are simultaneously obtained with CCD images so that the physical features (i.e. NW body, NW-NW junction in this case) can be mapped with thermal images side by side.

TR imaging measures the small change ( $\Delta R$ ,  $\sim 10^{-5}$ - $10^{-4}$ ) in surface optical reflectance ( $R$ ) as a material undergoes temperature change due to self-heating in response

to an applied voltage pulse across the device. By employing a lock-in technique and high-resolution CCD camera system (14 bit), thermal images with 50 mK temperature resolution along with sub-micron spatial resolution can be acquired. Since optical reflectance is very sensitive to temperature change, this technique gives much higher resolution than traditional IR imaging techniques. Fig. 3.4 shows the experimental set-up along with the applied bias (i.e. device heating pulse DHP) and the LED pulse to probe the relative change in surface reflectivity ( $\frac{\Delta R}{R}$ ). A 530 nm LED has been used in this experiment. The total LED power over the channel area ( $\sim 3 \mu W$ ) is much lower than the applied electrical power ( $\sim 70 mW$ ), and the duration of the LED pulse is significantly lower than the heating pulse. Therefore, heating from the LED pulse is insignificant compared to the Joule heating. Electrical contact to the devices was made by placing probes on the concentric circular contacts. Two different experiments consisting of 450  $\mu s$  and 10  $\mu s$  long DHPs were designed with a 10% duty cycle at a rate of 222 Hz and 10 KHz respectively in order to periodically heat the device, then allow the device to cool. By controlling the delay of the LED pulse (as shown in the Fig. 3.4(c)) with respect to the beginning of the DHP ( $\tau_D$ ), the  $\frac{\Delta R(t)}{R}$  (which is proportional to  $\Delta T(t)$ ) for the entire heating and cooling cycle can be probed. The 450  $\mu s$  heating pulse allowed observation of heating transients for a sufficiently long interval to allow quantification of the observed long time constant as well as to start the cooling cycle at or near a saturated  $\Delta T$ . In order to keep overall measurements time reasonable, the step in  $\tau_D$  is 10  $\mu s$ . The 10  $\mu s$  pulse allows a smaller step in  $\tau_D$  (200 ns) and can therefore resolve time constants below 1  $\mu s$ . A pulse length of 10  $\mu s$  is sufficiently long to reach saturation in the local self-heating temperature; somewhat longer pulses could be employed, but would include increased contributions from heat spreading. The data is averaged over 10 minutes of heating-cooling cycles to improve the signal to noise ratio.  $\frac{\Delta R}{R}$  at each pixel in the image is then divided by the TR coefficient ( $C_{TH}$ ) in order to convert it to a map of temperature change ( $\Delta T$ ). Extraction of the appropriate TR coefficient for the hybrid network is given in detail in [24]. In short, TR coefficient of bulk gold is used to derive  $\Delta T$  in the gold inner contact. Then, assuming  $\Delta T$  between gold contact (with known TR coefficient) and nearby hybrid network is similar over a short distance ( $\sim 100$  nm), TR coefficient for hybrid network is estimated from near-contact regions of the TR image. Since the TR signal is normalized to  $R$  and the latter is dominated by contributions from the NWs in the representative hotspots considered in this study, inhomogeneity of the network, e.g. spatial variation in number of NWs per hotspot region,

is expected to have minimal effect on the TR coefficient. For 530 nm LED illumination at 20x magnification, estimated TR coefficient for hybrid network was  $1.5 \times 10^{-4} \text{ K}^{-1}$ . The temperature resolution of the setup is 50mK, and the 20x lens (NA= 0.4) with a field of view of  $\sim 450 \mu\text{m} \times 450 \mu\text{m}$  gives a pixel resolution of  $\sim 670 \text{ nm}$ .

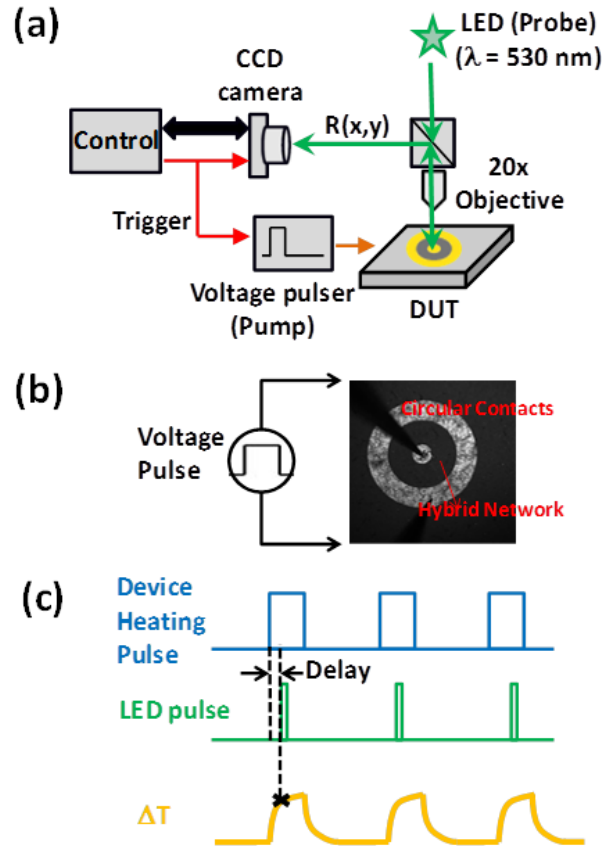


Fig. 3.4: (a) Experimental set-up of TR measurement (b) 20x CCD image of a hybrid device showing the circular contacts along with the probes (c) Schematics of the transient TR measurements showing the device heating pulse, heating and cooling cycle and delay  $\tau_D$  of the LED pulse.

To study the electro-thermal response of microscopic hotspots formed at the NW-NW junctions in silver NW network (Chapter 5), a high magnification 100x objective lens (NA = 0.75) with a field of view  $\sim 100 \mu\text{m} \times 100 \mu\text{m}$  is employed. An Andor CCD camera with  $512 \times 512$  active pixels captures the reflected light from the surface of the silver NWs. This provides a higher spatial resolution of  $\sim 200 - 400 \text{ nm}$  (discussed in detail in Chapter 5).  $C_{TH}$  for silver NW network is extracted in a similar way and is described in detail in

[24]. At 100x magnification 530 nm LED illumination, we estimated  $C_{TH}$  for silver NW network  $\sim 1.2 \times 10^{-4} \text{ K}^{-1}$ . Finally, since high magnification measurements are more prone to spatial drift towards X, Y, Z directions due to thermal expansion, extrinsic vibrations etc. compared to low magnification measurements, two additional things are considered specifically for measurements in 100x magnification. Firstly, a laser-based auto-focus system was utilized to focus on the surface of the NWs and then auto-correct the focus in case of perturbations along the Z direction. Secondly, to correct any spatial drift in the X-Y plane, customized MATLAB image processing scripts are developed to plot the CCD profiles along a sharp feature at different  $\tau_D$  s to check if the location remains the same at different time instants  $\tau_D$  s (i.e. if they occur around the same pixels). All the thermal images are adjusted accordingly with respect to  $\tau_D = 0$ .

## 4. TRANSIENT THERMAL RESPONSE OF HOTSPOTS IN GRAPHENE-SILVER NANOWIRE HYBRID TRANSPARENT CONDUCTING ELECTRODES

### 4.1 Overview

In this chapter, we report transient temperature responses of local hotspot regions within a hybrid network to quantify their electro-thermal properties. During both the heating and cooling cycles, we observe two distinct time constants. We have determined how the time constants and associated temperature amplitudes of the hotspots change as a function of distance from the contact. We found that the short time constant is associated with the local self-heating of the nanowire (NW)-NW junctions within the hotspot region and the long time constant with heat diffusion through the channel region. We have used heat diffusion equations to develop a physically-based explanation of the results. The spatial and temporal response of self-heating due to the electrical current at the hotspots can provide information on the coupled electro-thermal response and a means to separate the effects of local self-heating from those of heat spreading from electrical contacts as well as qualitative understanding of current pathways within the network. *The content of this chapter is taken from our previous publication in IEEE Transactions on Nanotechnology [2], and thus copyrighted by IEEE.*

### 4.2 Transient Response of Hotspots

In the following, we take transient thermal images of the device to see the temporal evolution of the hotspots. Fig. 4.1 shows representative TR images ( $\Delta T$ ) captured at various time instants ( $\tau_D$ ) after the start of a 450  $\mu\text{s}$  voltage pulse. The applied voltage is 1.4 V, which induces a current of  $\sim 50$  mA. Certain localized areas in the network are seen to have much higher  $\Delta T$  (as high as 60 K) than surrounding areas and are recognized as “hotspots (HS)”. The hotspots are inhomogeneous both in spatial location and in temperature. In this analysis, a  $4 \mu\text{m} \times 4 \mu\text{m}$  area ( $\sim 36$  pixels), generally encompassing several NW-NW junctions (microscopic hotspots, with dimensions of  $\sim$  hundreds of nanometers), is selected for each hotspot. Fig. 4.2 shows a schematic of such a  $4 \mu\text{m} \times 4$

$\mu\text{m}$  hotspot ( $\sim 36$  pixels) that consists of multiple microscopic hotspots formed at the NW-NW junctions.

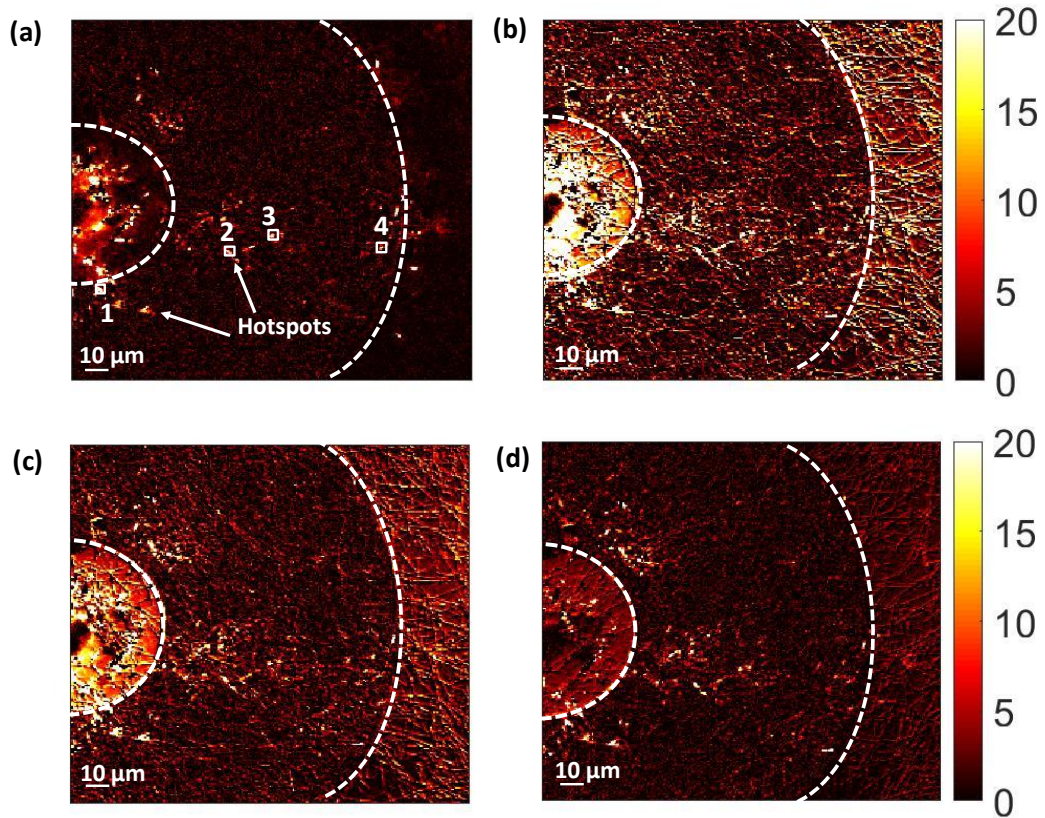


Fig. 4.1: Transient response at different  $\tau_D$  s showing formation of hotspots during heating cycle at (a)  $10 \mu\text{s}$ , and (b)  $450 \mu\text{s}$  respectively and during cooling cycle at (c)  $520 \mu\text{s}$ , and (d)  $980 \mu\text{s}$  respectively. Left and right dotted lines represent the inner and the outer contacts respectively. Four different hotspots located  $46$ ,  $71$ ,  $87$ , and  $134 \mu\text{m}$  away from the center of the inner contact are labelled and denoted as hotspots 1-4, respectively, throughout the chapter.

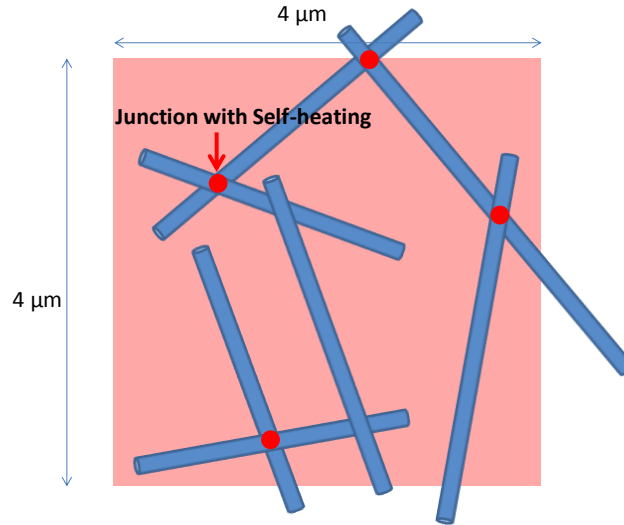


Fig. 4.2: Schematic of a hotspot.

Fig. 4.3(a) shows the temperature evolution of several hotspots at different spatial locations as a function of time, obtained using long range pulse (DHP of 450 μs, 5 μs LED pulse width, and 10 μs steps in  $\tau_D$ ). For each of these hotspots, there is a sharp temperature increase at the beginning, followed by a slower saturating trend in  $\Delta T$ .

In order to observe  $\Delta T$  in the fast part of the transient, we also performed a separate TR imaging with a higher temporal resolution, by applying a short range pulse (DHP of 10 μs, 200 ns LED pulse width, and 200 ns steps in  $\tau_D$ ) as shown in Fig. 4.4(a). The combination of the short and the long DHP allow us to observe the time dynamics from several hundred ns to ms range. Clearly, the transient heating exhibits two distinct thermal time constants. Similar two distinct time constants are also observed for cooling periods following the long and short range pulses, respectively, as shown in Fig. 4.3(b) and Fig. 4.4(b).

To quantify the two step transient dynamics, we fitted the heating data with  $\Delta T = A_{1H} (1 - e^{-\frac{t}{\tau_{1H}}}) + A_{2H} (1 - e^{-\frac{t}{\tau_{2H}}})$  where  $\tau_{1H}$  and  $\tau_{2H}$  are the short and long thermal time constants, and  $A_{1H}$  and  $A_{2H}$  the corresponding amplitudes, respectively (see solid lines in Fig. 4.3 and Fig. 4.4). Similarly, the cooling transient data has been fitted with  $\Delta T = A_{1C} e^{-\frac{t}{\tau_{1C}}} + A_{2C} e^{-\frac{t}{\tau_{2C}}}$ . The long range heating (cooling) data is used to obtain  $\tau_{2H}$  ( $\tau_{2C}$ ),  $A_{1H}$  ( $A_{1C}$ ), and  $A_{2H}$  ( $A_{1C}$ ). The short range heating (cooling) data is used to obtain  $\tau_{1H}$  ( $\tau_{1C}$ ). In this way, we obtain thermal time constants for different hotspots with  $\tau_{1H} < 1 \mu s$  and  $\tau_{2H}$  in the range  $\sim 350-1000 \mu s$ . Cooling cycles exhibit  $\tau_{1C} < 1 \mu s$  and  $\tau_{2C} \sim 450-3000 \mu s$ .

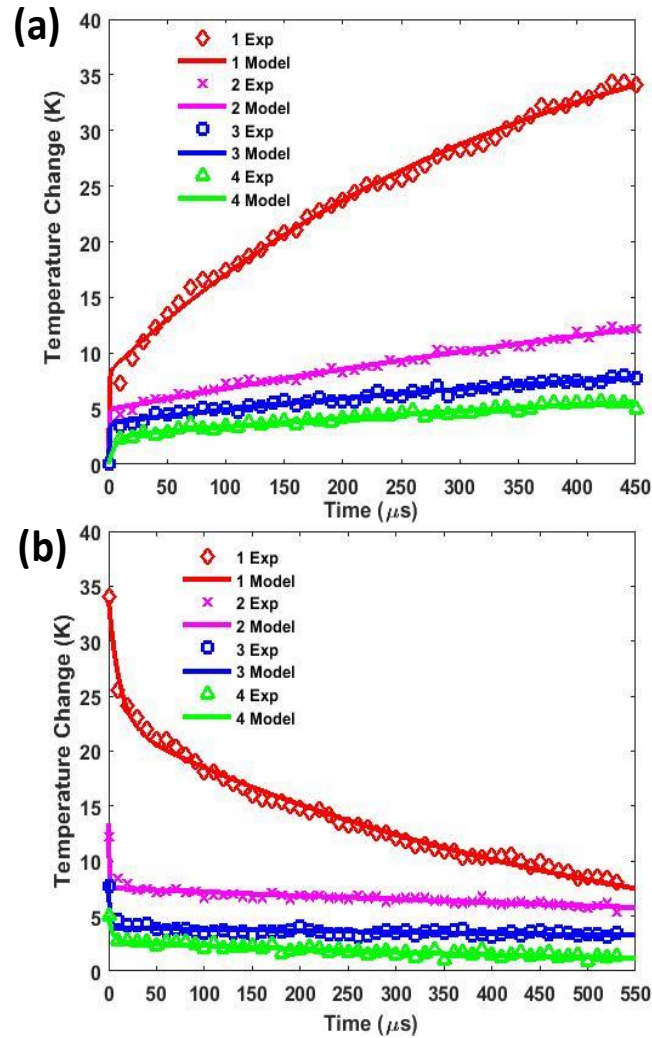


Fig. 4.3:  $\Delta T$  vs time (i.e.  $\tau_D$ ) for long device heating pulse of 450  $\mu\text{s}$  (a) heating cycle (b) cooling cycle for hotspots 1- 4 (Fig. 4.1).

Different hotspots within the network show qualitatively similar behavior, but with varying time constants, maximum temperature change and relative weighting of the two time constants (shown in Fig. 4.5). Switching of current pathways under bias have been observed in previous TR studies on NW networks, including those with longer square-wave bias pulses [30]. In the current study, no evidence of switching of pathways or turn-on/turn-off of specific hotspots was observed over the time duration of the measurements. In comparison to the prior studies which exhibited switching, the improved device stability is attributed to both the lower sheet resistance of hybrid networks, leading to lower power

dissipation at comparable current levels, as well as improved stability associated with passivation and local heat spreading effects of the graphene layer [43]. In the following, we examine the spatial dependence in order to understand the physical origin of such transients.

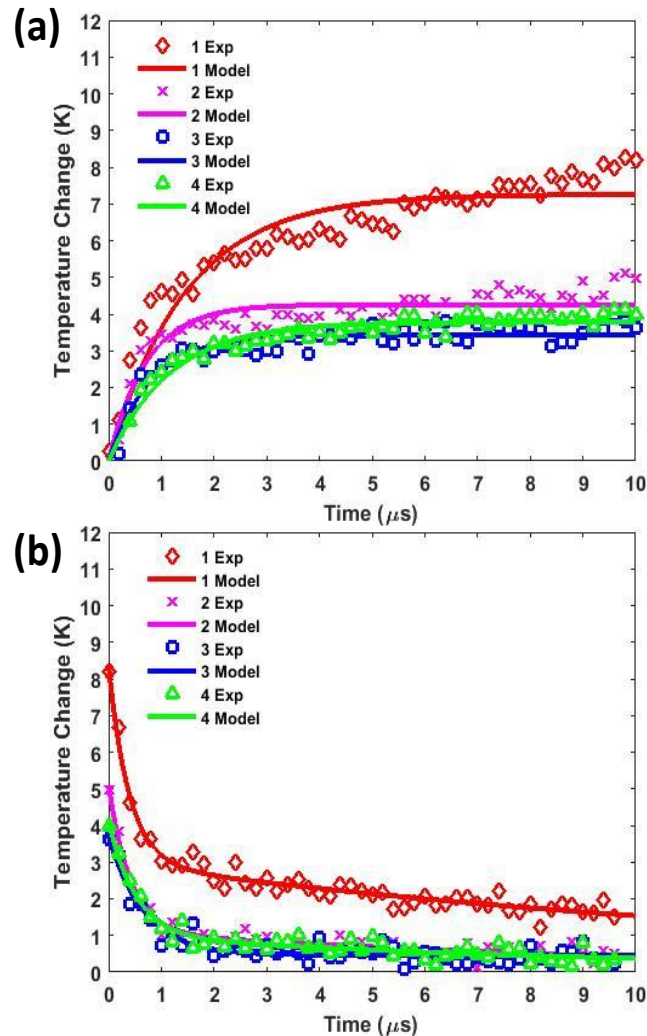


Fig. 4.4:  $\Delta T$  vs time (i.e.  $\tau_D$ ) for short device heating pulse of 10  $\mu\text{s}$  (a) heating cycle (b) cooling cycle for hotspots 1- 4 (Fig. 4.1).

### 4.3 Radial Dependence of Time Constants and Amplitudes of Hotspots

Fig. 4.5 shows the time constants and amplitudes, respectively, extracted from hotspots and non-hotspots (discussed later) as functions of distance  $r$  from the center of the

inner contact. Note that the radius of the inner contact is  $40\ \mu\text{m}$  and the inner radius of the outer contact is  $140\ \mu\text{m}$ . The first important observation is that the short time constant ( $\tau_{1H}$  or  $\tau_{1C}$ ) remains relatively constant as a function of  $r$  while the long time constant ( $\tau_{2H}$  or  $\tau_{2C}$ ) systematically varies with  $r$ , with the longest time constants observed near the midpoint between the two contacts. The values of  $\tau_{2H}$  and  $\tau_{2C}$  are comparable, and almost 3 orders of magnitude larger than those of  $\tau_{1H}$  and  $\tau_{1C}$ . Apart from the above differences in time constants, the steady state magnitudes of the two responses ( $A_1$  and  $A_2$ ) also show distinct behavior. For example, Fig. 4.5(b) and Fig. 4.5(c) show the amplitudes  $A_{1H}$ ,  $A_{1C}$ , and  $A_{2H}$ ,  $A_{2C}$  respectively as a function of  $r$ . The magnitude of  $A_1$  (both  $A_{1H}$  and  $A_{1C}$ ) systematically decreases with  $r$ , while that of  $A_2$  (both  $A_{2H}$  and  $A_{2C}$ ) are higher near the two contacts, but decreasing towards the center. Both of the above observations play an important role in understanding the origin of the hotspot transients as we explain below:

A hotspot originates at locations where local conductance inhomogeneity such as within the NW-NW junction results in higher heat dissipation. Temperature at the hotspot region rises very fast (less than  $1\ \mu\text{s}$ ) due to this local self-heating, with time constant  $\tau_1$ . Note that  $\tau_1$  entirely depends on thermal properties in the vicinity of a NW-NW junction and thus we do not see a systematic variation of  $\tau_1$  with  $r$  (Fig. 4.5(a)). However, the steady state temperature due to this local self-heating does depend on the local power dissipation. Since we have used a concentric radial device structure, there is a systematic  $r$  dependence of the local power dissipation (described in the next section). As a result, we see that the steady state hotspot temperature component ( $A_1$ ) decreases with  $r$  (Fig. 4.5(b)). On top of this local self-heating, the hotspot temperature transient is also influenced by the heat spreading through the channel— this comprises the long-time-constant portion of the transients ( $A_2, \tau_2$ ). In the samples considered in this study, self-heating in the contact regions induces a relatively large temperature rise within the contacts, and heat diffusion from the contacts into the channel region dominates this long-time constant regime. Heat generated at the contacts (or stored, in case of the cooling cycle) diffuses into the channel region, resulting to a contribution to  $\Delta T$  with longer time constant ( $\tau_2$ ) and larger spatial extent than that of the local self-heating. This component of  $\Delta T$  depends on the thermal properties and diffusion geometry, including the distance from the hotspot location to the nearest heat source/sink. Thus, the hotspots further away from either contact (middle area of the channel, see Fig. 4.5(a) and Fig. 4.5(c)) have higher  $\tau_2$  and lower steady state amplitude ( $A_2$ ), as confirmed quantitatively using a heat diffusion model shown in the next section. In this experiment, the observed  $A_{1H}$  ( $A_{1C}$ ) is generally about half as large as  $A_{2H}$

( $A_{2C}$ ). Thus, in order to study the local self-heating of hotspots, one must be careful to exclude the extrinsic  $A_{2H}$ ,  $\tau_2$  transients.

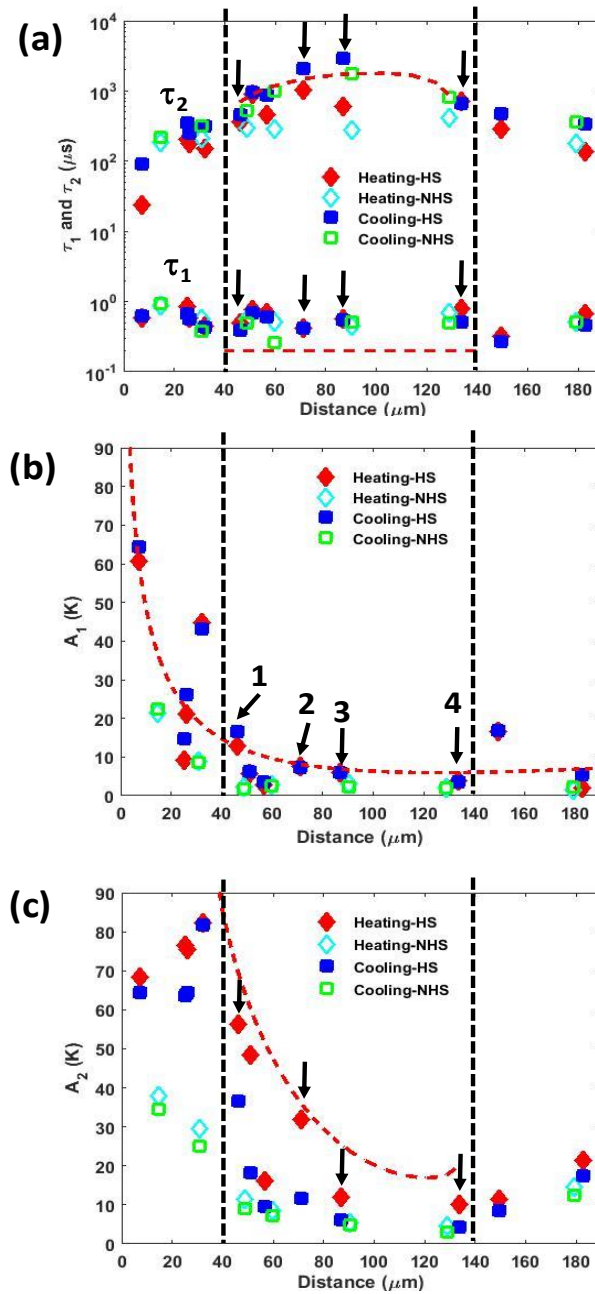


Fig. 4.5: (a)  $\tau_1$ ,  $\tau_2$  vs distance ( $r$ ) for hotspots (HSs) and non-hotspots (NHSs). Dashed line represents simulation (calculated) results for  $\tau_{2H}$  ( $\tau_{1H}$ ). (b)  $A_1$  vs  $r$  for the same. Dashed line represents the analytical solution for  $A_{1H}$ . (c)  $A_2$  vs  $r$  for the same. Dashed line represents the simulation results for  $A_{2H}$ . The simulations and the analytical results

are for HSs during the heating cycle.  $r < 40 \mu\text{m}$  and  $r > 140 \mu\text{m}$  represent the inner and the outer electrical contact regions respectively. Vertical dashed lines correspond to the boundaries between contacts and channel region.  $\tau_1$ ,  $\tau_2$ ,  $A_1$ , and  $A_2$  values of hotspots 1-4 are shown in arrows.

#### 4.4 Self-Heating and Heat Diffusion Model

We use a heat transfer model describing local self-heating and/or heat diffusion in order to model the radial dependencies of the amplitudes and time constants shown in Fig. 4.5. The general heat transfer equation for a homogeneous thermal conductor is:

$$\frac{\delta\Delta T}{\delta t} = \frac{\kappa}{\rho C} \nabla^2(\Delta T) + \frac{1}{\rho C} Q_r \quad (4.1)$$

Here,  $\rho$  is the mass density,  $C$  is the specific heat,  $\kappa$  is the thermal conductivity, and  $Q_r$  is the generated heat per unit volume (unit  $\text{W}/\text{m}^3$ ) at position  $r$  for the system under consideration. With appropriate geometries and source/boundary terms, the equation can be used to model either local generation, e.g. in the vicinity of a hotspot, or long-range diffusion of heat through the channel region.

#### 4.5 Local Self-heating

##### 4.5.1 Local Self-heating at Hotspots

First, consider the local self-heating at the hotspots, quantified by  $A_1$  and  $\tau_1$ . In order to find the steady state temperature ( $A_1$ ), ideally one should consider  $Q_r$  as localized functions ( $Q_L$ ) corresponding to heat generation at the center of each hotspot. Over the course of a characteristic length  $L_0$ , determined by the relative values of the thermal parameters within the local hotspots with respect to the values within the overall 2D network, heat will propagate through the network and eventually to the substrate and  $\Delta T$  will return to the “background” value within that region of the larger network. Here,  $Q_L = \frac{I_{Local}^2 R_{Local}}{V_{Local}}$ ;  $I_{Local}$  is the local current,  $R_{Local}$  is the local electrical resistance of the hotspot region, and  $V_{Local}$  is the effective volume of the hotspot. The modeled local temperature distribution around a hotspot would then qualitatively be:  $A_1(r_0) \propto Q_L \text{erfc}\left(\frac{r_0}{L_0}\right)$  with  $\tau_1 = \frac{L_0^2}{D_{Local}}$  where  $r_0$  is the distance from the center of the hotspot, and  $D_{Local}$  is the thermal diffusion coefficient corresponding to local heat flow. Since neither  $I_{Local}$  nor  $R_{Local}$  are

known for a given hotspot, it is not possible to accurately predict the relative values of  $A_1$  for various hotspots nor an explicit dependence of  $A_1$  on  $r$ .

To calculate  $\tau_1$ , we approximate  $L_0 \cong 4 \mu m$  for various hotspots at different  $r$ . Experimentally, we observe most hotspots to be contained within a  $4 \mu m \times 4 \mu m$  hotspot area, indicating that  $L_0$  for our hybrid network is less than or equal to  $4 \mu m$ . Assuming that heat spreading within the network dominates over a distance  $L_0$  (before heat transfers into the quartz substrate), the relevant diffusion coefficient is  $D \cong D_{Hybrid}$  (effective thermal diffusion coefficient of hybrid network). Using  $D_{Hybrid} = 4.2 \times 10^{-1} \frac{\mu m^2}{\mu s}$ , as estimated from reported values for Ag NW networks and graphene (discussed in details later in section 4.8), we calculate  $\tau_1 = \frac{L_0^2}{D_{Hybrid}} \cong 0.2 \mu s$ , which is in line with experimentally observed values.

#### 4.5.2 Local Self-heating in Homogenous Conductor

In order to understand how the observed radial ( $r$ ) dependence of local self-heating compares with that expected from a homogeneous conductor, the heat transfer equation can be solved for a spatially uniform conductor with concentric circular geometry. In this case,  $Q_r$  is denoted as  $Q_H$ , and corresponds to spatially-distributed Joule heating ( $r$  dependent heat generation) caused by total current  $I$  that flows radially from inner to outer contact. Here,  $Q_H = I^2 \frac{\rho_{rs}}{(2\pi d)^2} \frac{1}{r^2}$  where  $\rho_{rs}$  and  $d$  are the resistivity and the thickness of the electrical conductor respectively. Since the short time constant regime corresponds to relatively short-range heat diffusion (compared to the long time constant regime), it is assumed that the heat diffusion is also 2D and thermal conduction through the bulk of the quartz substrate can be ignored. Under this assumption, an analytical solution can be developed. The steady state solution of Eq. (4.1), valid for  $t \gg \tau_1$  has the form of

$$A_1(r) = \Delta T(r) = B [[\log(r)]^2] + C_1 \log(r) + C_2 \quad (4.2)$$

Where,

$$B = \frac{1}{\kappa} Q_H r^2 = I^2 \frac{\rho_{rs}}{\kappa (2\pi d)^2} \quad (4.3)$$

Details of the derivation are presented in the next section. The dashed line in Fig. 4.5(b) shows fitting of the analytical solution for HSs for the heating cycle which qualitatively agrees with the experimental dependence of  $A_1$  on  $r$ . This indicates that the

decrease of  $A_1$  with  $r$  is consistent with spatial variations in local power generation ( $Q_r$ ) rather than due to significant changes in the local thermal properties ( $\kappa$ ,  $C$  etc.).

#### 4.5.2.1 Analytical Model of Local Self-heating in Homogenous Conductor

Using heat diffusion equation, we can find out how  $A_1$  is expected to change with distance  $r$  in case of a uniform thin film. Let's consider a strip of width  $dr$  at distance  $r$  from the center of the inner contact in a uniform thin film of thickness  $d$ , resistivity  $\rho_{rs}$ , and thermal conductivity  $\kappa$ .  $Q_r$  is the generated heat per unit volume ( $\frac{W}{m^3}$ ) of the strip due to Joule heating caused by current  $I$  that flows radially uniformly from the inner contact to the outer contact.

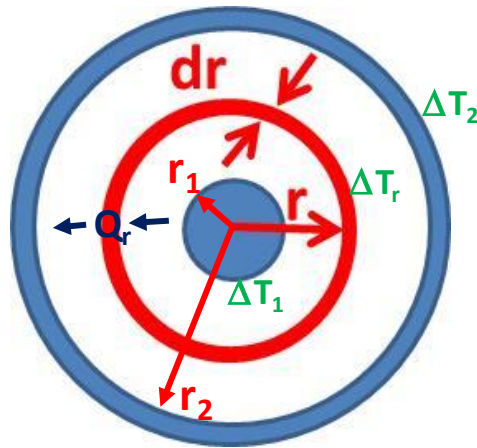


Fig. 4.6: Geometry considered for analytical model of self-heating in homogenous conductor e.g. metal thin film

Now,

$$Q_r = \frac{I^2 R'}{V'} \quad (4.4)$$

Where  $R'$  is the total resistance and  $V'$  is the volume of the  $dr$  strip.  $R'$  and  $V'$  can be expressed as:

$$R' = \frac{\rho_{rs} dr}{2\pi r d} \quad (4.5)$$

$$V' = 2\pi r d dr \quad (4.6)$$

Plugging these in the  $Q_r$  expression in Eq. (4.4) gives,

$$Q_r = I^2 \frac{\rho_{rs}}{(2\pi d)^2} \frac{1}{r^2} \quad (4.7)$$

From heat continuity equation,

$$\frac{\delta \Delta T}{\delta t} = \frac{\kappa}{\rho C} \nabla^2(\Delta T) + \frac{1}{\rho C} Q_r \quad (4.8)$$

Here,  $\rho$  and  $C$  are the mass density and specific heat capacity of the uniform film. Expanding  $\nabla^2(\Delta T)$  in this equation gives,

$$\Rightarrow \frac{\delta \Delta T}{\delta t} = \frac{\kappa}{\rho C} \left[ \frac{1}{r} \frac{\delta}{\delta r} \left( r \frac{\delta \Delta T}{\delta r} \right) \right] + \frac{1}{\rho C} Q_r \quad (4.9)$$

using cylindrical coordinate and no  $z$  and  $\theta$  dependence ( $\frac{\delta \Delta T}{\delta \theta} = 0, \frac{\delta \Delta T}{\delta z} = 0$ ).

In order to find an analytical expression for  $A_1$ , we consider steady state condition  $\frac{\delta \Delta T}{\delta t} = 0$ . From Eq. (4.9) we get,

$$\begin{aligned} \Rightarrow 0 &= \frac{\kappa}{\rho C} \left[ \frac{1}{r} \frac{\delta}{\delta r} \left( r \frac{\delta \Delta T}{\delta r} \right) \right] + \frac{1}{\rho C} Q_r \\ \Rightarrow 0 &= \left[ \frac{\delta}{\delta r} \left( r \frac{\delta \Delta T}{\delta r} \right) \right] + \frac{1}{\kappa} Q_r r ; \quad \text{divided by } \frac{\kappa}{\rho C} \frac{1}{r} \\ \Rightarrow 0 &= \left[ \frac{\delta}{\delta r} \left( r \frac{\delta \Delta T}{\delta r} \right) \right] + \frac{B'}{r} ; \quad B' = I^2 \frac{\rho_{rs}}{\kappa (2\pi d)^2} \\ \Rightarrow \left[ \frac{\delta}{\delta r} \left( r \frac{\delta \Delta T}{\delta r} \right) \right] &= -\frac{B'}{r} \\ \Rightarrow \int_{r_1}^r \left[ \frac{\delta}{\delta r} \left( r \frac{\delta \Delta T}{\delta r} \right) \right] dr &= -\int_{r_1}^r \frac{B'}{r} dr \\ \Rightarrow r \frac{\delta \Delta T}{\delta r} &= -B' \log\left(\frac{r}{r_1}\right) + C1' \\ \Rightarrow \frac{\delta \Delta T}{\delta r} &= -B' \frac{\log(r)}{r} + \frac{C1}{r} \end{aligned}$$

$$\begin{aligned}
&\Rightarrow \int_{r_1}^r \frac{\delta \Delta T}{\delta r} dr = - \int_{r_1}^r B' \frac{\log(r)}{r} dr + \int_{r_1}^r \frac{C1}{r} dr \\
\Rightarrow \Delta T(r) - \Delta T(r_1) &= -\frac{B'}{2} [[\log(r)]^2 - [\log(r_1)]^2] + C1 \log\left(\frac{r}{r_1}\right) + C2' \\
\Rightarrow \Delta T(r) &= B [[\log(r)]^2] + C1 \log(r) + C2 \tag{4.10}
\end{aligned}$$

Here,  $\Delta T$  is the steady state temperature profile i.e.  $A_1$ .

We fitted the experimental  $A_1$  data with this analytical model using the ‘‘Curve fitting tool’’ in MATLAB ( $B$ ,  $C1$ , and  $C2$  are the fitting parameters). The fitting of the HSs during the heating cycle is shown in dashed line in Fig. 4.5(b).

#### 4.6 Heat Diffusion through Channel Region

In order to model temperature rise exclusively due to heat diffusion (e.g. heat generated within the contacts and diffusing into the channel region, quantified by  $(A_2, \tau_2)$ ), we solve Eq. (4.1) with  $Q_r = 0$  considering the time dependent temperature rise of the electrical contacts. As mentioned before, within time interval of 0-10  $\mu\text{s}$  after the application of the 450  $\mu\text{s}$  wide voltage pulse, temperature rises mainly due to self-heating. After 10  $\mu\text{s}$ , temperature rise (as high as twice the increase due to local self-heating) is primarily due to heat spreading from the contacts. Therefore,  $\Delta T$  at any spatial location of the network (including the hotspots) is the superposition of temperature rise due to local self-heating and heat propagation from contacts. This spreading of heat from the contacts is predominantly through the substrate (quartz, 500  $\mu\text{m}$  thick) since it provides the least thermally resistive pathway compared to the thin hybrid network of effective thickness  $\sim 30$  nm (calculations of thermal resistances are provided in section 4.9). Therefore, we have solved Eq. (4.1) for quartz using a finite element analysis tool ‘‘PDETool’’ in MATLAB. In Fig. 4.5(a) and Fig. 4.5(c), the dashed lines show the simulated results for  $\tau_{2H}$  and  $A_{2H}$  respectively for HSs for the heating cycle. The simulation utilized reported material properties for quartz and the cylindrical geometry of the device. A boundary condition consisting of the time-dependent  $\Delta T$  of the inner contact was calculated from the experimental temperature transients for hotspots within the contact; otherwise, no fitting parameters were used. Details of the simulation, materials parameters and procedure for

extracting  $\tau_{2H}$  and  $A_{2H}$  from simulation are provided in the next section. In both the figures, the simulated plots capture the trend of how  $A_{2H}$  and  $\tau_{2H}$  change over distance  $r$ .

#### 4.6.1 Simulation of Diffusion of Heat from Electrical Contacts

The partial differential Eq. (4.1) has been solved using finite element analysis with heat generation  $Q = 0$  within the network/quartz and the electrical contacts as heat sources over the time interval  $\tau_D = 0 - 450 \mu s$ . Since the thermal resistance of quartz is 3 orders smaller than that of hybrid network (details of thermal resistance are discussed later), we did the simulation for system containing only the quartz substrate ( $500 \mu m$  thick) to see if the temperature rise due to heat diffusion from the contacts is consistent with heat diffusion through quartz. The spatial domain is chosen such that  $r' = 280 \mu m$  corresponds to the center of the inner contact ( $r = 40 \mu m$ ). The boundary conditions for this system include Dirichlet boundary conditions corresponding to  $\Delta T$  at  $r' = 240 - 320 \mu m$  (representing the inner contact) and  $r' = 100 - 140 \mu m$  and  $420 - 460 \mu m$  (representing the outer contact) which are specified as  $f(t)$  since  $\Delta T$  within the contacts takes time to rise to its steady state value. The expression for the boundary condition for the inner (outer) contact has been obtained by fitting experimental transient  $\Delta T$  of the hotspot at  $r = 32 \mu m$  ( $150 \mu m$ ), the measurement point closest to  $r = 40 \mu m$  ( $140 \mu m$ ) and within the electrical contacts, with  $A_{1H} (1 - e^{-\frac{t}{\tau_{1H}}}) + A_{2H} (1 - e^{-\frac{t}{\tau_{2H}}})$ . Fig. 4.7 shows the experimental data and the fit for the hotspot at  $r = 32 \mu m$  during the heating cycle.

The resulting boundary condition for the inner contact is:

$$\Delta T (r', t) = 52.5 * \left(1 - \exp\left(-\frac{t}{8.5}\right)\right) + 78 * \left(1 - \exp\left(-\frac{t}{185}\right)\right); | r' = 240 - 320 \mu m$$

The boundary condition for the outer contact is:

$$\begin{aligned} \Delta T (r', t) &= 11.12 * \left(1 - \exp\left(-\frac{t}{4.8}\right)\right) + 8 * \left(1 - \exp\left(-\frac{t}{414}\right)\right); | r' \\ &= 100 - 140 \mu m, 420 - 460 \mu m \end{aligned}$$

For the boundary representing the interface between quartz and the copper heat sink, we assume Neumann boundary,  $\kappa_{Quartz} grad(\Delta T) = h \Delta T$

Here  $h$  represents the heat transfer coefficient between quartz and underneath copper heat sink. Considering the thickness of the quartz, since it takes more than  $45 ms$

(verified by simulation for  $\tau_D = 0 - 45 \text{ ms}$ ) to reach to the bottom interface,  $h$  can be an arbitrary value in the simulation for  $\tau_D = 0 - 450 \text{ } \mu\text{s}$  time domain.

For all other boundaries, we assume  $grad(\Delta T) = 0$  i.e. no incoming or outgoing heat flux.

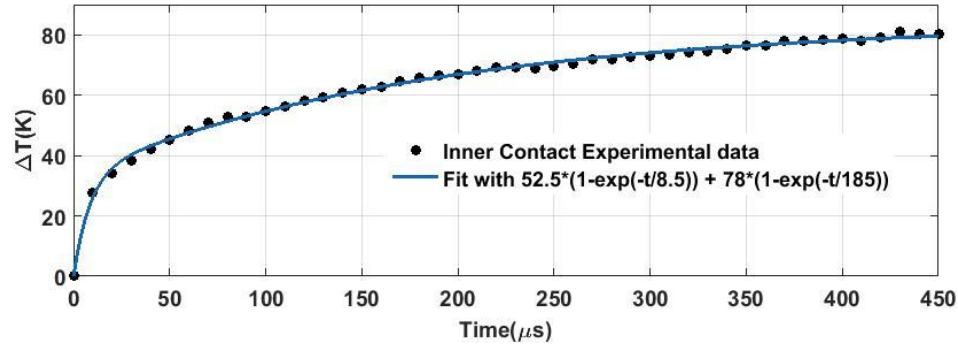


Fig. 4.7: Thermal transient of the hotspot at the edge of the inner contact (at  $r = 32 \text{ } \mu\text{m}$ ) used to obtain boundary condition for temperature rise in the inner contact.

#### 4.6.2 Transformation of Heat Diffusion Equation from 3-D Cylindrical Geometry to a 2-D Cartesian Geometry

Heat diffusion from the electrical contacts is a 3-D cylindrical heat problem. Since the “Partial Differential Equation Toolbox” of MATLAB supports 2-D geometry and requires the equation to be in Cartesian coordinates, we performed the transformation according to [63] in the following way.

The heat diffusion equation for the channel region is:

$$\rho C \frac{\partial \Delta T}{\partial t} - \nabla \cdot (\kappa \nabla (\Delta T)) = Q \quad (4.11)$$

For heat diffusing through the network from the electrical contacts,  $Q = 0$ . Using Cylindrical coordinate system and plugging  $Q = 0$  in Eq. (4.11),

$$\rho C \frac{\partial \Delta T}{\partial t} - \nabla \cdot (\kappa \nabla (\Delta T)) = 0$$

$$\Rightarrow \rho C \frac{\partial \Delta T}{\partial t} - \frac{1}{r} \frac{\partial}{\partial r} \left( \kappa r \frac{\partial \Delta T}{\partial r} \right) - \frac{1}{r^2} \frac{\partial}{\partial \theta} \left( \kappa \frac{\partial \Delta T}{\partial \theta} \right) - \frac{\partial}{\partial z} \left( \kappa \frac{\partial \Delta T}{\partial z} \right) = 0 \quad (4.12)$$

The problem is axisymmetric i.e.  $\frac{\partial \Delta T}{\partial \theta} = 0$ . Since the Partial Differential Equation Toolbox requires the equations to be in Cartesian coordinates, the transformation from Cylindrical to Cartesian is performed according to [63]. Multiplying both sides of Eq. (4.12) with  $r$ ,

$$\rho r C \frac{\partial \Delta T}{\partial t} - \frac{\partial}{\partial r} \left( \kappa r \frac{\partial \Delta T}{\partial r} \right) - \frac{\partial}{\partial z} \left( \kappa r \frac{\partial \Delta T}{\partial z} \right) = 0 \quad (4.13)$$

Defining  $r$  as  $x$  and  $z$  as  $y$  (i.e.  $x$  axis represents  $r$  direction and  $y$  axis represents  $z$  direction), we get,

$$\rho x C \frac{\partial \Delta T}{\partial t} - \nabla \cdot (\kappa x \nabla (\Delta T)) = 0$$

### 4.6.3 Simulation Results

Fig. 4.8 shows the simulation results at  $\tau_D = 450 \mu\text{s}$ . The  $\rho$ ,  $C$ ,  $\kappa$  parameters of quartz used in the simulation are summarized in Table 4.1. The temperature profile at  $\tau_D = 450 \mu\text{s}$  shows that heat diffuses  $\sim 50 \mu\text{m}$  into the quartz over this time interval. We plotted the temperature profile at the surface of the quartz vs distance at different  $\tau_{DS}$  as shown in solid line in Fig. 4.9. In the same figure, we also plotted experimentally extracted  $(\Delta T - A_{IH})$  with distance for various hotspots. By removing the contribution from local self-heating ( $A_{IH}$ ),  $(\Delta T - A_{IH})$  corresponds to the component of  $\Delta T$  due to only heat diffusion. As seen from the figure, the simulation results qualitatively capture the experimental trends with distance.

In Fig. 4.10, we plotted experimental  $\Delta T - A_{IH}$  vs time ( $\tau_D$ ) for different hotspots along with the simulation values for the corresponding radii. Here, we also see that the simulation results show the trends of the experimental data.

In order to obtain  $A_{2H}$  vs distance from the simulation, we plotted  $\Delta T - A_{IH}$  vs  $\tau_D$  for a longer  $\tau_D = 3000 \mu\text{s}$  as shown in Fig. 4.11. Even though we see that the profiles do not reach steady state due to the thickness of the quartz,  $3000 \mu\text{s}$  time interval is still consistent with the time needed for heat to diffuse at least to the middle of the  $100 \mu\text{m}$  channel ( $\sim 60 \mu\text{m}$  as seen from Fig. 4.5(c)) according to  $\frac{L^2}{D_{quartz}} = \frac{(60 \times 10^{-6})^2}{1.4e-6} \cong 2600 \mu\text{s}$ . Here,  $D_{quartz}$  is the thermal diffusivity of quartz. We took  $\Delta T - A_{IH}$  value at  $3000 \mu\text{s}$  as  $A_{2H}$  and the time it takes to reach 63% of it (analogous to  $\frac{1}{e}$  point for a simple exponential rise) as  $\tau_{2H}$ . In Fig. 4.5(a) and Fig. 4.5(c), these  $A_{2H}$  and  $\tau_{2H}$  are shown respectively in dashed line with respect to  $r$ .

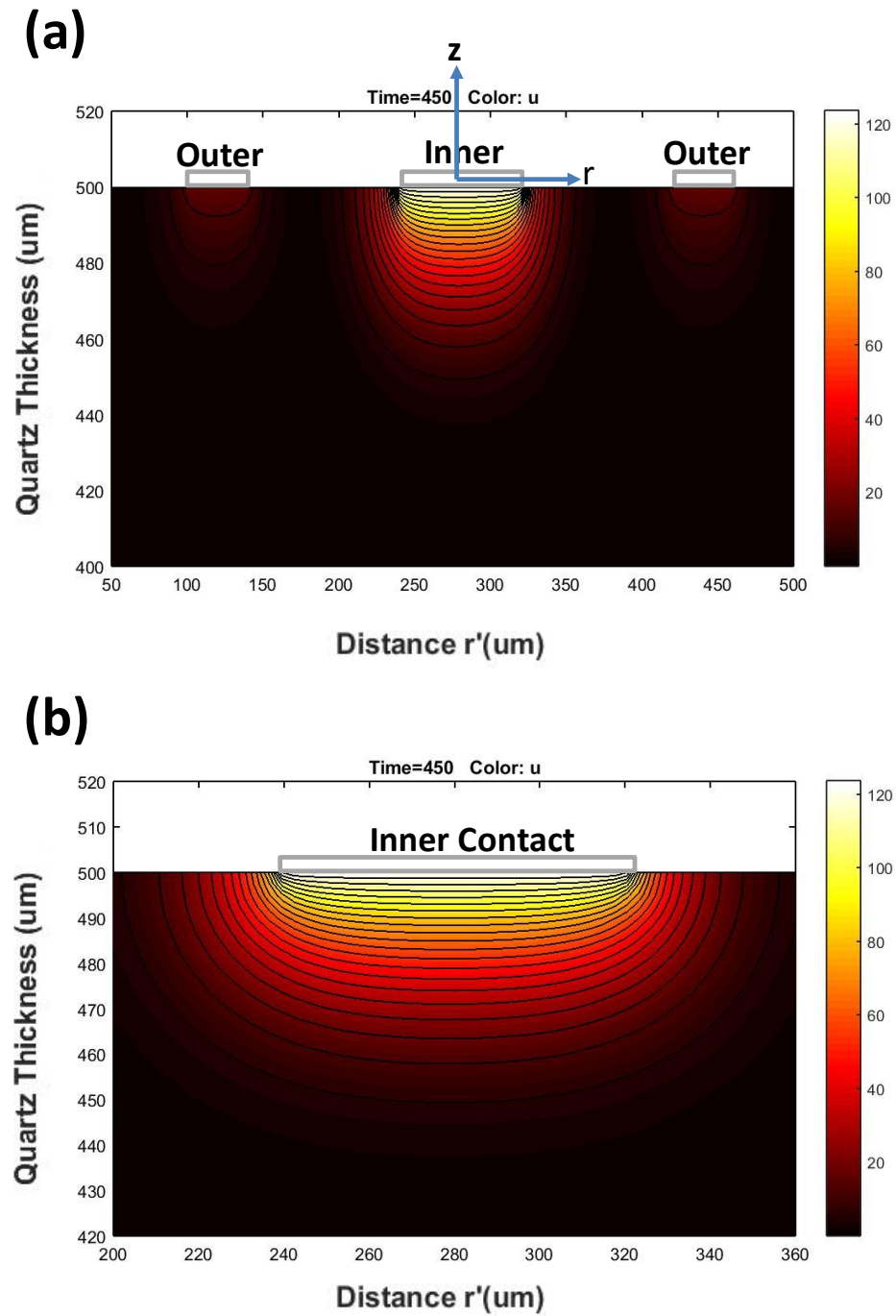


Fig. 4.8: (a) PDE simulation results at  $450 \mu\text{s}$  across quartz. The cross-sectional view of the inner and outer contacts are also shown. (b) Zoomed out view of (a). Here,  $r' = 280 \mu\text{m}$  corresponds to the center of the inner contact i.e.  $r = 0$ .

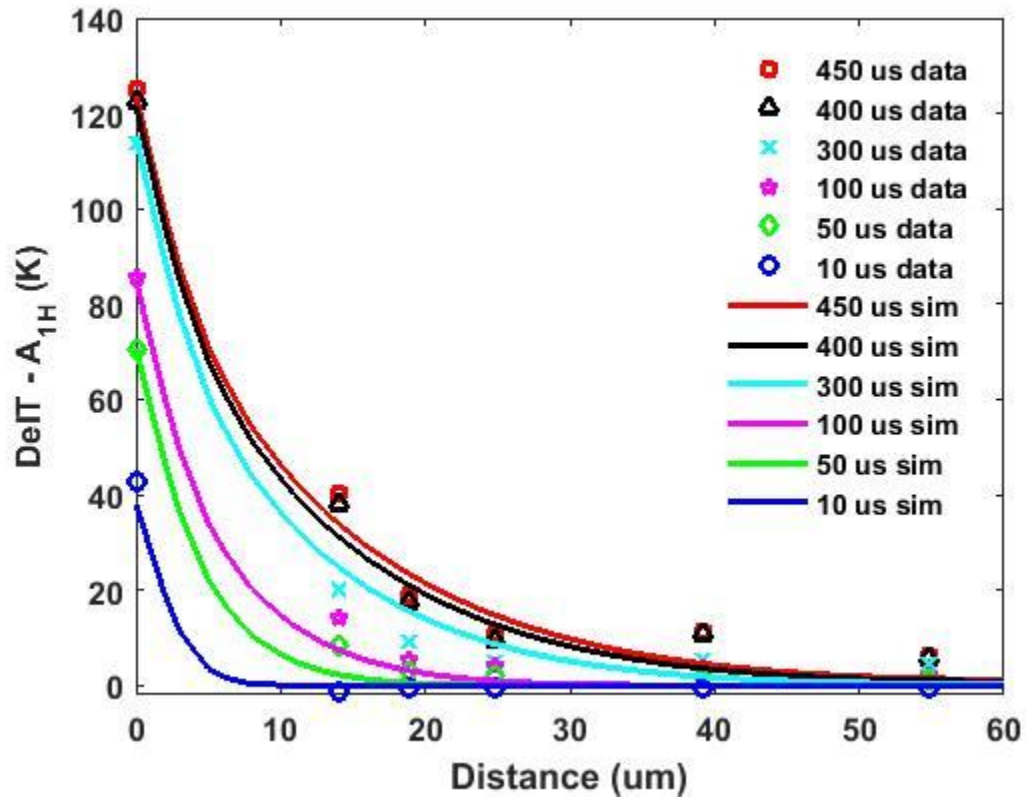


Fig. 4.9: Experimental  $\Delta T - A_{1H}$  (i.e. temperature rise due to diffusion only) vs distance at different time ( $\tau_D$ ).  $A_{1H}$  is different for different HSs. Solid lines represent plots generated from PDE simulation. Simulation plots show the trends of the experimental data. Here, distance corresponds to distance from the edge of the inner contact towards the right outer contact ( $r' = 320 - 380 \mu\text{m}$  from Fig. 4.8).

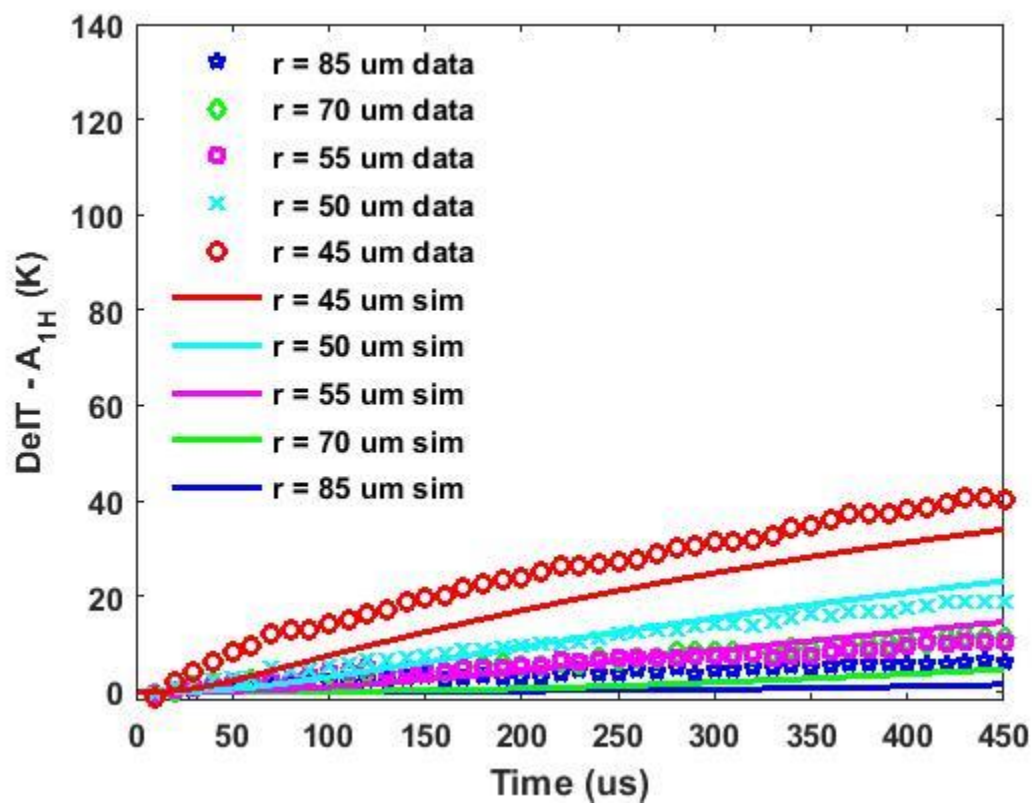


Fig. 4.10: Experimental  $\Delta T - A_{1H}$  vs time ( $\tau_D$ ) for different HSs located at different distances. Solid lines represent plots generated from PDE simulation. Simulation plots represent the trends of the experimental data.

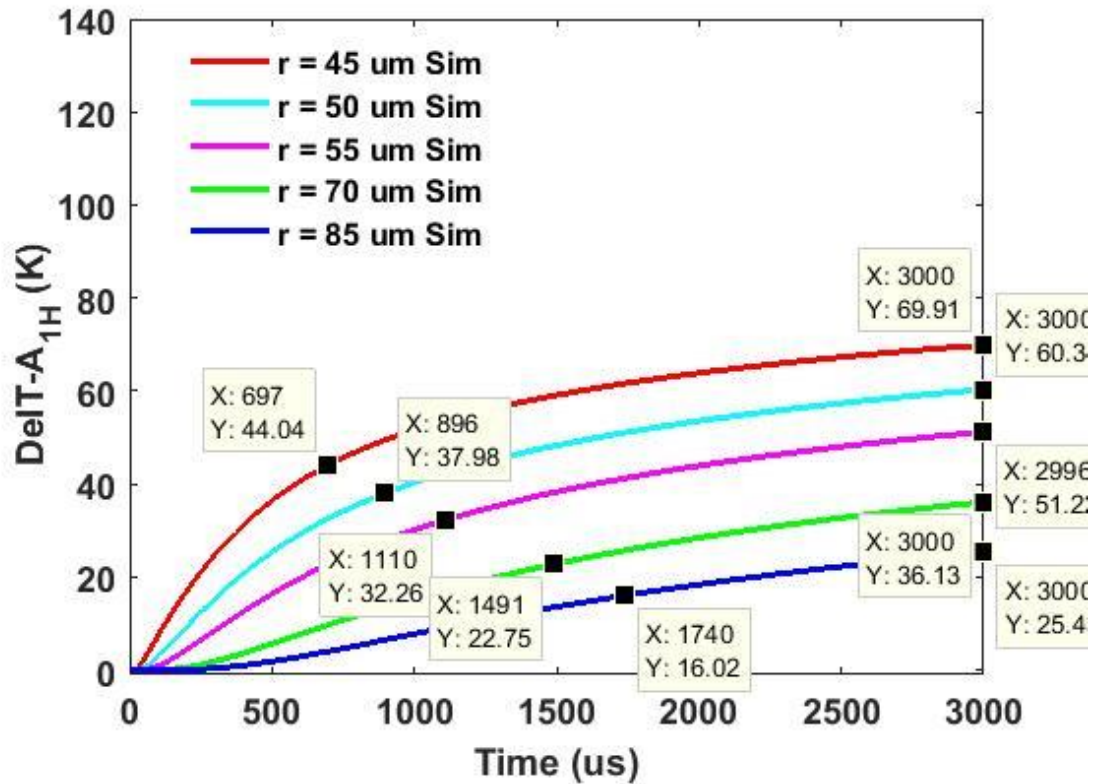


Fig. 4.11: Simulation of  $\Delta T - A_{1H}$  vs time ( $\tau_D$ ) for  $\tau_D = 3000 \mu s$ .

We also performed a separate PDE simulation of a system consisting of thin silver film (thickness = 30 nm) on top of quartz using bulk silver material parameters as listed in Table 4.1. The simulation results show that silver film reaches thermal equilibrium (same  $\Delta T$ ) with quartz in the time interval of  $\tau_D = 0- 450 \mu s$  which generates similar  $\Delta T$  profiles shown in Fig. 4.9, Fig. 4.10, and Fig. 4.11 within the film.

#### 4.7 Transient Response of Non-Hotspots

In order to verify the generality of the transient response, we also extracted  $A$  and  $\tau$  values for regions close to the hotspots but with lower  $\Delta T$  (we designate these regions as “non-hotspots” (NHS)). Thermal image in Fig. 4.12 illustrates temperature profile of a hotspot and nearby non-hotspot.  $\Delta T$  vs distance scan shows  $\Delta T$  is lower for a non-hotspot.

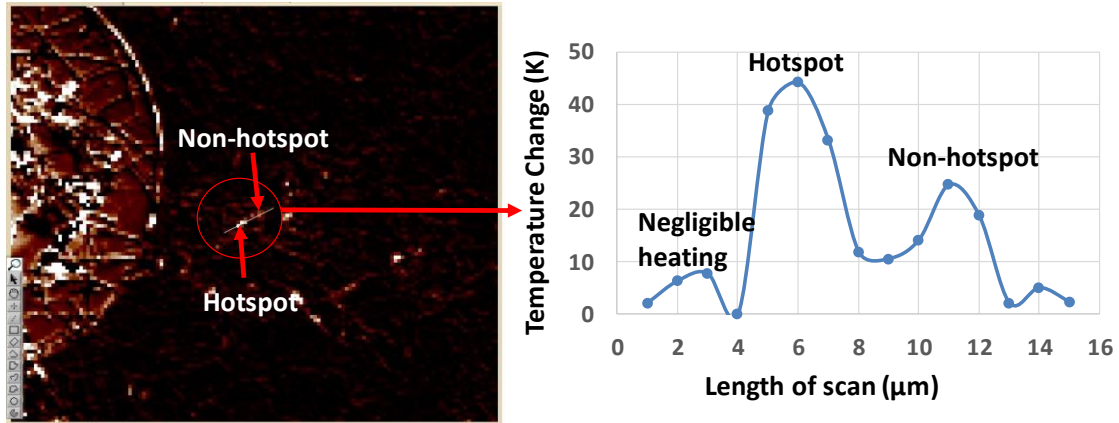


Fig. 4.12:  $\Delta T$  profile for a hotspot and nearby non-hotspot.

In general, the trends in  $\tau_1$ ,  $\tau_2$ ,  $A_1$  and  $A_2$  with  $r$  in the NHSs are similar to those in the hotspots as shown in Fig. 4.5. The  $\tau_1$  and  $\tau_2$  values for NHSs are in the same order as those for HSs. This is expected since  $\tau_1$  and  $\tau_2$  depend on how fast/slow heat is generated and/or propagated through the network irrespective of the actual  $\Delta T$ . In general, the  $A_1$  values (i.e. temperature rise due to local Joule heating) are lower at the NHS areas, which would be consistent with less self-heating. The overall time response of most NHS regions with respect to that of nearby HS regions is consistent with results expected for superposition of the initial temperature rise, with  $A_1$  of NHS  $<$   $A_1$  of HS, and comparable longer-time responses, i.e.  $A_2$  of NHS  $\cong$   $A_2$  of HS. The latter is expected since  $A_2$  is associated with long-range heat diffusion through the channel region. However, for NHS regions within or near the inner contact, the value of  $A_2$  is lower than those in nearby HS regions. One possible explanation is that the HS regions are in stronger thermal contact with the contacts regions, e.g. through dense local pathways within the network. In addition to the weak electrical coupling to the network, the NHS regions may also be more weakly thermally coupled to the network. Regardless of different NW-NW junction orientation (resulting in varying junction resistance and spatially varying  $\Delta T$ ), heterogeneity of the network, distance from the contacts or different device geometry,  $A_1, \tau_1$  tell qualitatively the local thermal and electrical connectivity of the NW junctions present in that region and  $A_2, \tau_2$  tell qualitatively how heat diffuses from a nearby heat source (e.g. electrical contacts) to that region of the network.

## 4.8 Determination of Network Material Parameters

Table 4.1: Physical properties used for calculation of  $\rho_{Hybrid}$ ,  $C_{Hybrid}$ ,  $\kappa_{Hybrid}$

	Mass Density $\rho$ (Kg/m <sup>3</sup> )	Thermal Conductivity $\kappa$ (W/mK)	Specific Heat $C$ (J/KgK)
Monolayer Graphene	2000	600 (on Si)[64]	748[64]
AgNW Network	-	37 (in-plane)[65]	232[35]
Quartz	2203	1.3	740
Bulk Silver	10490	406	238.64

Mass Density of Hybrid Network,  $\rho_{Hybrid}$ :

Sample size is 1 cm  $\times$  1 cm and NW density is  $\sim 4.8 \times 10^6$  cm<sup>-2</sup>. We calculated previously in [1] that the effective thickness of the silver nanowire (NW) network  $d_{AgNW Network}$  is  $\sim 28$  nm.  $d_{Graphene} = 0.34$  nm.

$$\rho_{Hybrid} = \frac{m_{AgNW Network} + m_{Graphene}}{Total\ volume}$$

$$= \frac{(4.8 \times 10^6 \times \pi \times (45 \times 10^{-9})^2 \times 40 \times 10^{-6} \times 10490) + (2000 \times 10^{-4} \times 0.34 \times 10^{-9})}{10^{-2} \times 10^{-2} \times 28.34 \times 10^{-9}} = 4.54 \times 10^3 \text{ Kg/m}^3$$

Taking graphene and AgNW network as two parallel thermal conductors, expressions for effective  $\kappa_{Hybrid}$  and  $C_{Hybrid}$  are obtained. The values are then calculated using parameters shown in the Table 4.1.

Effective Thermal conductivity of Hybrid network,  $\kappa_{Hybrid}$ :

$$\kappa_{Hybrid} = \frac{\kappa_{Graphene} d_{Graphene} + \kappa_{AgNW network} d_{AgNW Network}}{d_{Graphene} + d_{AgNW Network}} \cong 45 \text{ W/mK}$$

Effective Specific heat of Hybrid network,  $C_{Hybrid}$ :

$$C_{Hybrid} = \frac{\rho_{Graphene} d_{Graphene} C_{Graphene} + \rho_{AgNW network} d_{AgNW Network} C_{AgNW network}}{\rho_{Graphene} d_{Graphene} + \rho_{AgNW Network} d_{AgNW Network}} =$$

$$\frac{2 \times 10^3 \times 0.34 \times 748 + 4.571 \times 10^3 \times 28 \times 232}{2 \times 10^3 \times 0.34 + 4.571 \times 10^3 \times 28} \cong 234 \text{ J/KgK}$$

Both  $\kappa_{Hybrid}$  and  $C_{Hybrid}$  approximates to silver NW network values  $\kappa_{AgNW\ network}$  and  $C_{AgNW\ network}$  respectively due to thicker NW network compared to monolayer graphene.

Effective Thermal diffusion coefficient of Hybrid network,  $D_{Hybrid}$ :

$$D_{Hybrid} = \frac{\kappa_{Hybrid}}{\rho_{Hybrid}C_{Hybrid}} = 4.2 \times 10^{-5} \text{ m}^2/\text{s}$$

#### 4.9 Determination of Thermal Resistances of Network and Substrate

Cross-plane (vertical) thermal resistance of Quartz:

Cross-plane thermal resistance of 500  $\mu\text{m}$  thick quartz with a cross sectional area of  $\pi(r_2^2 - r_1^2) = \pi(140^2 - 40^2) \mu\text{m}^2$  is,

$$\theta_{Quartz-cross\ plane} = \frac{1}{1.3} \frac{0.5 \times 10^{-3}}{\pi(140^2 - 40^2) \times 10^{-12}} = 6.8 \times 10^3 \text{ K/W}$$

In-plane (horizontal) thermal resistance:

In-plane thermal resistances of the channel region ( $r_1 = 40 \mu\text{m}$  to  $r_2 = 140 \mu\text{m}$ ) are calculated in the following way. Thermal conductivity values are from literature as summarized in Table 4.1. Thickness of AgNW layers and graphene are taken as 28 nm ( $d_1$ ) and 0.34 nm ( $d_2$ ) respectively.

$$\theta_{AgNW-Inplane} = \frac{1}{\kappa_{In-plane\ AgNW\ network}} \int_{r_1=40\ \mu\text{m}}^{r_2=140\ \mu\text{m}} \frac{dr}{2\pi r d_1} = \frac{1}{37} \frac{\log(\frac{140}{40})}{2\pi \times 28 \times 10^{-9}} = 1.9 \times 10^5 \text{ K/W}$$

$$\theta_{Graphene-Inplane} = \frac{1}{600} \frac{\log(\frac{140}{40})}{2\pi \times 0.34 \times 10^{-9}} = 9.8 \times 10^5 \text{ K/W}$$

Taking these two layers as parallel to one another, thermal resistance of the hybrid network is obtained.

$$\theta_{Hybrid-Inplane} = \theta_{Th-AgNW} \parallel \theta_{Graphene} = 1.6 \times 10^5 \text{ K/W}$$

In-plane thermal resistance of quartz (thickness 500  $\mu\text{m}$ ) is,

$$\theta_{Quartz-Inplane} = \frac{1}{1.3} \frac{\log(\frac{140}{40})}{2\pi \times 0.5 \times 10^{-3}} = 3 \times 10^2 \text{ K/W}$$

In-plane  $\theta_{Quartz-Inplane}$  is 3 orders smaller than in-plane  $\theta_{Hybrid-Inplane}$  which suggests that heat from the electrical contacts flows predominantly through quartz.

## 4.10 Conclusion

In this chapter, we have investigated transient thermal characteristics of hybrid graphene-AgNW TCEs using high-resolution TR imaging technique. The observation of transient temperature change in hotspots provides significant insights about how heat is generated locally and diffused through the network and substrate. Two distinct thermal time constants are observed, and the spatial dependencies of both time constants and amplitudes have been studied for hotspot and non-hotspots. Our results quantitatively determine the thermal time constants of the hotspots and show their dependence on distance. Collectively, these studies allow the temperature rise to be decoupled into separate contributions from local self-heating and heat spreading from the contacts. Such decoupling is extremely important to study the intrinsic local electrical and thermal characteristics of the network. A heat diffusion model indicates that the long time constant response is due to heat diffusion from the electrical contacts through the channel region and can qualitatively explain the observed dependence on radius. The diffusion model is also consistent with the explanation of the short time constant response corresponding to local self-heating within a given hotspot region. The approach and experimental method for decoupling local self-heating from long-range diffusion can be universally applied to other device geometries and to various materials, including homogeneous thin films or other percolating/copercolating networks. This approach of temporal imaging and quantifying thermal constants can be very useful in reliability studies for example in electro-migration etc. to detect the weakest links and also in designing and fabricating better TCEs both in terms of conductance and heat dissipation.

## 5. TRANSIENT SELF-HEATING AT NANOWIRE JUNCTIONS IN SILVER NANOWIRE NETWORK CONDUCTORS

### 5.1 Overview

As discussed in the previous chapters, nano-structured networks have drawn attention as potential replacements for bulk-material approaches in applications including transparent conducting electrodes (TCEs). As TCEs, these systems can provide relatively low sheet resistances in the high optical transmission regime along with mechanical flexibility [19-21, 23, 44, 66]. Silver nanowire (NW) networks have been widely studied and offer the potential for relative cost-effectiveness [7], large scale mass printing [8-11], and ease of fabrication and integration with device structures [12-16]. In these networks, NW-NW junction resistances dominate the sheet resistance, and self-heating due to current flow through these junctions induces hotspots in the vicinity of these junctions. This self-heating can potentially redistribute and/or turn off percolating conductive current pathways due to elevated temperatures and thus impose reliability concerns [17, 18]. Different techniques have been employed to minimize the effects of these transport bottleneck including thermal annealing, laser annealing, introduction of an additional layer/coating [9, 19-23] and fabricating junction-free networks [17, 19], at the cost of additional fabrication steps. Most prior experimental studies have focused on large-area steady state exploration of electrical and optical properties or microscopic studies of single/few junctions within the networks [24]. Comprehensive studies about the hotspots, particularly their microscopic origin, thermal characteristics and evolution with time, are necessary to understand fully percolating transport in these network systems as well as the coupled electro-thermal response.

In this chapter, we discuss the thermal transients of microscopic hotspots formed at NW-NW junctions employing high-resolution thermoreflectance (TR) imaging techniques. Previously, TR imaging has been employed to obtain temporal characteristics of bulk materials and devices such as field effect transistors, thermo-electric materials, super-capacitors, micro-refrigerators, and power transistors [48-52, 54, 67-70]. Recently, TR has been employed as a powerful tool to study intrinsic inhomogeneous network systems due to its spatial, temporal and temperature resolution along with its simultaneous ability to provide fast acquisition of thermal images over a large field of view [24, 30].

Using this measurement system, *ns* scale temporal and *nm* scale spatial resolution is achievable with a fast scanning rate over a large region ( $\sim 600 \mu\text{m} \times 600 \mu\text{m}$ ), thus providing the means to study multiple junctions simultaneously within the network with high-resolution. These attributes are advantageous compared to other thermal imaging techniques (scanning Joule expansion microscopy, inverted optical microscopy, infra-red optical sensor) that have been used to study the dynamics of hotspot formation and/or current conducting pathways in NW and CNT based systems [32, 34-36, 58-62, 71-73]. Moreover, the TR method is contact-less, making it easier to image hard-to-fabricate samples. Most importantly, since thermal images and CCD images are obtained concurrently, the microscopic origin of the hotspots can be readily mapped to physical features (NW-NW junction, NW body in this case) by overlaying both images [70, 74, 75]. Previously in Chapter 4, we studied the temporal response of hotspot regions comprised of areas encompassing several NW-NW junctions using a transient TR technique [76]. These experiments allowed study of both short-range (in the vicinity of the hotspot region) and long-range (network) thermal behavior, but could not resolve the dynamics of individual microscopic hotspots formed at the NW-NW junctions.

In this chapter, we experimentally study local self-heating in individual hotspots in a silver NW network, including high-resolution spatial and temporal evolution. We quantitatively determine the thermal time constants and temperature rises of the microscopic hotspots. For both heating and cooling cycles, we observe thermal time constants less than  $1 \mu\text{s}$  at various hotspots. For a representative hotspot, line scans along two crossing NWs, taken at different time instants ranging from 0-2  $\mu\text{s}$ , show the temporal and spatial evolution of the temperature profile. We estimate the van der Waals force ( $\sim 4.0244 \text{ N}$ ), contact width ( $\sim 5 \text{ nm}$ ), and interface thermal resistance ( $\sim 1.6 \times 10^5 \text{ K/W}$ ) between NWs and underlying substrate. We develop a heat transfer model that considers local power generated at a hotspot, local coupling between the NWs and substrate, heat conduction along the NWs and heat transfer into the substrate and use the model to interpret the experimental data. The heat transfer model and experimental temperature profile help to quantify the local power generated at the hotspot due to Joule heating and the fraction of this power propagating along each wire. Parameters including thermal time constants, interface thermal resistance and power generated at the hotspots provide valuable insights about coupled electro-thermal conduction within silver NW networks and will thus help guide development of future TCE technologies.

## 5.2 Thermal Transients of Microscopic Hotspots in Silver Nanowire network

TR imaging at 100x magnification provides image of the entire channel length (illustrated in Fig 5.1(b) and (c)) with higher spatial resolution ( $\sim 200 - 400$  nm) allowing simultaneous characterization of all hotspots within a quadrant of the circular TLM. Grayscale CCD images of the silver NW network (e.g. Fig 5.1(b)), clearly show the NW bodies and NW-NW junctions. Corresponding TR images (e.g. Fig 5.1(c)) show that certain localized areas in the network have much higher  $\Delta T$  (as high as 25 K) than surrounding areas and are mostly formed at the NW-NW junctions. These regions are recognized as “microscopic hotspots”. Due to the inhomogeneous nature of the network, microscopic hotspots are non-uniform both in spatial location and in temperature.

Fig. 5.2 shows representative high temporal resolution TR images of the entire network captured within the field of view of the 100x lens, at various  $\tau_D$  after the start of a 10  $\mu$ s voltage pulse. Left (right) column represents time points within the heating (cooling) cycle. During the heating cycle,  $\Delta T$  at the hotspots initially increases with increasing time, then saturates at  $\sim 1$  or 2  $\mu$ s. During the cooling cycle,  $\Delta T$  monotonically decreases.

For thermal transient analysis, we have used customized MATLAB scripts to realize a masking algorithm to produce binary images from the high-resolution CCD images to select only the NW bodies and junctions and to eliminate the substrate. Details of the construction of the binary image is given in section 5.6.

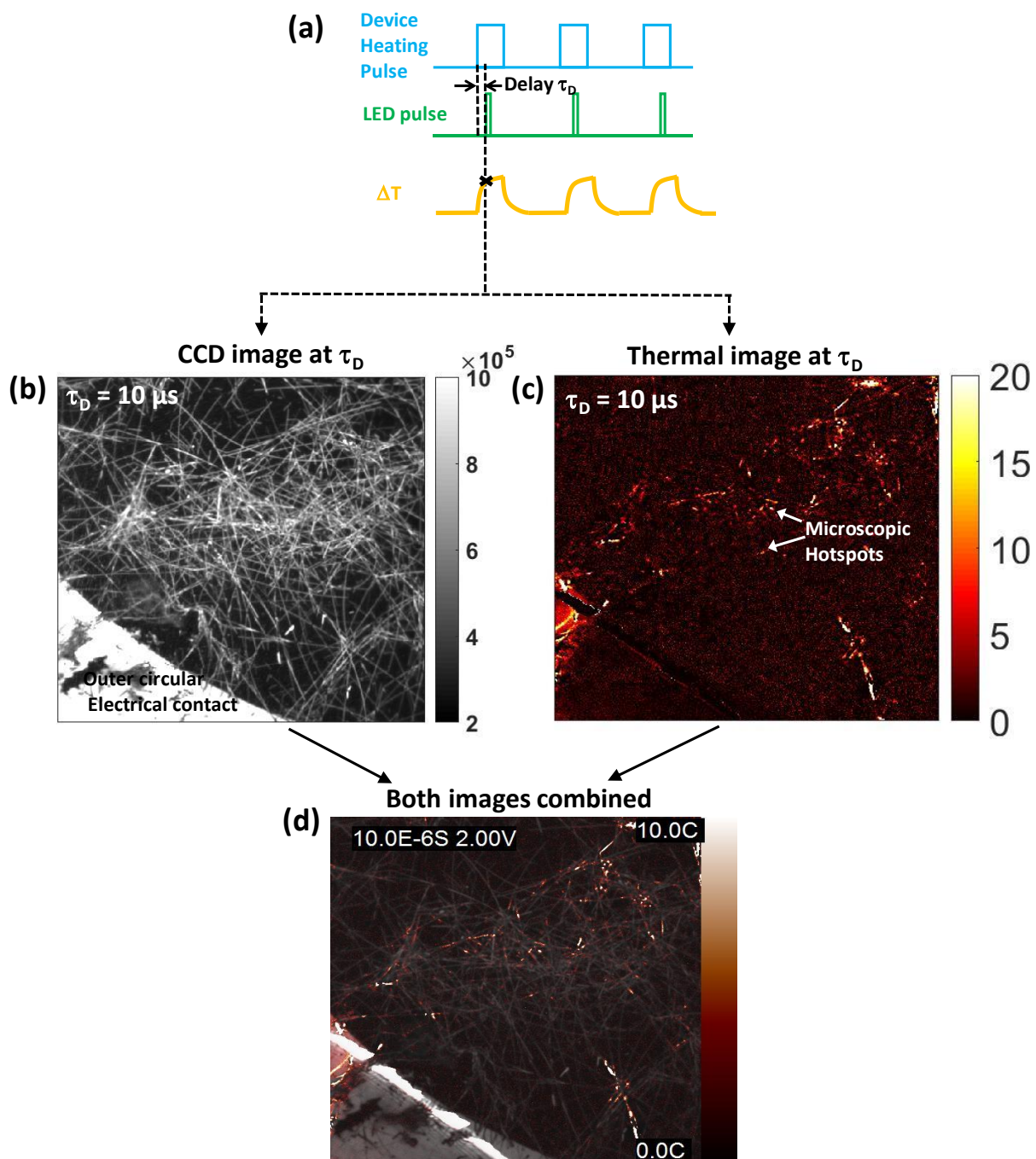


Fig 5.1: (a) Relative timing diagrams of applied voltage pulse, LED pulse showing delay  $\tau_D$ , and temperature rise/fall during the heating (voltage pulse “on”) and cooling cycle; (b) CCD image at  $\tau_D = 10 \mu\text{s}$  of the portion of the silver NW network visible within the field of view of 100x lens; (c) Corresponding thermal image at  $\tau_D = 10 \mu\text{s}$ ; (d) CCD image superimposed on the thermal image to illustrate the physical location of hotspots with respect to the NW junctions.

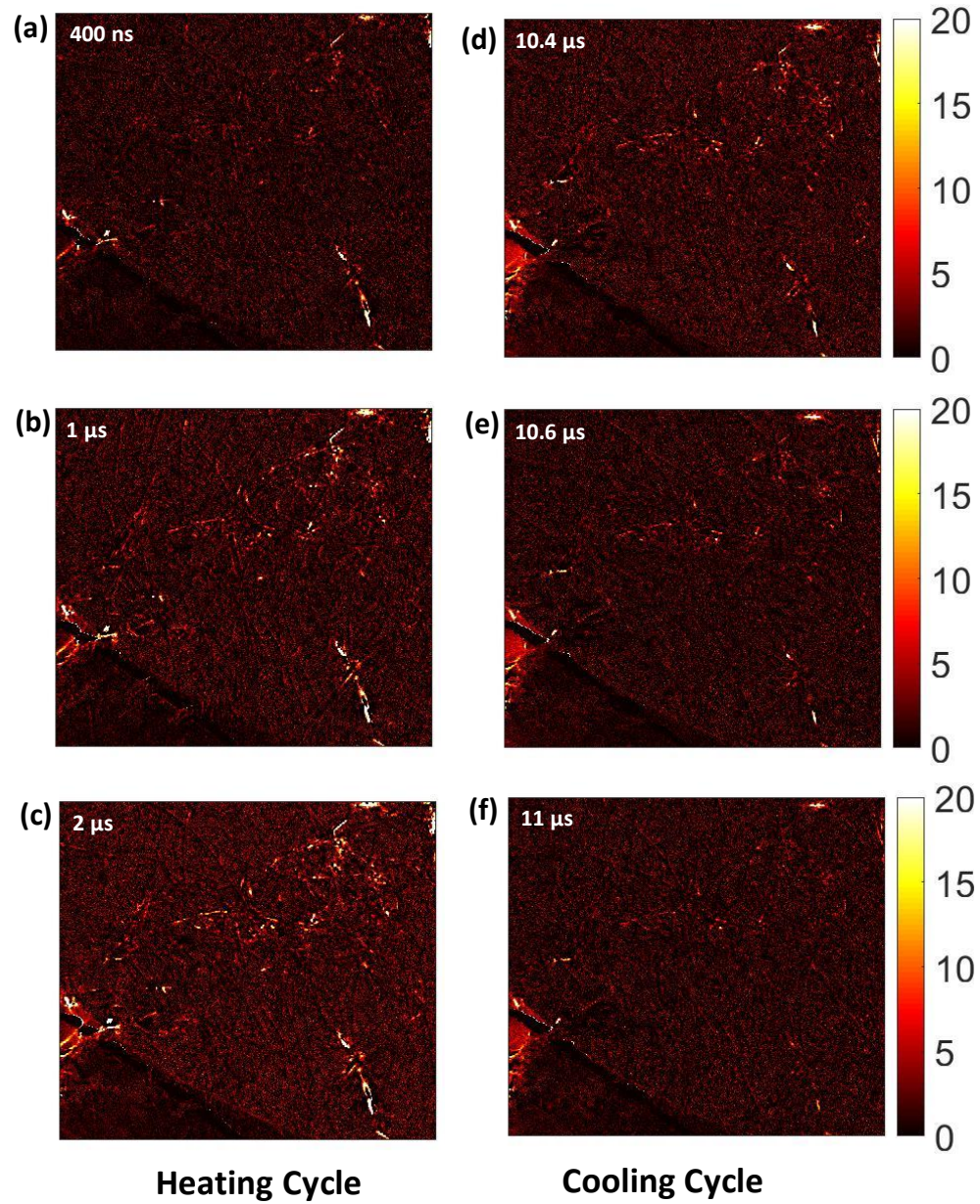


Fig. 5.2: Thermal images at different time (i.e.  $\tau_D$ ) during the heating cycle at (a) 400 ns (b) 1  $\mu\text{s}$  (c) 2  $\mu\text{s}$  and during the cooling cycle at (d) 10.4  $\mu\text{s}$  (e) 10.6  $\mu\text{s}$  (f) 11  $\mu\text{s}$ .

### 5.2.1 Temporal Evolution of Microscopic Hotspots

In order to analyze the behavior at a single microscopic hotspot, we considered a representative region within the network. Fig. 5.3(a) is a false color CCD image of the

region at  $\tau_D = 1 \mu\text{s}$ , showing several NWs and junctions. Two crossing NWs (NW #1 and NW #2) are indicated by red lines in the image; the junction formed at their intersection (location 1) is the site of a hotspot. (The same CCD image without the red lines is presented in Fig. 5.4). Fig. 5.3(b) shows a superimposed CCD image and TR image at  $\tau_D = 1 \mu\text{s}$ , illustrating that the hotspot location coincides with the junction at location 1. Although the overall fields of view are different, the yellow rectangles in Fig. 5.3(a) and Fig. 5.3(b) denote the same region. Fig. 5.5 represents the transient thermal images of this hotspot at different time delays ( $\tau_D$  s) which clearly shows the self-heating and spatial extent in the vicinity of the junction at location 1. The radius of the red circle is  $\sim 500 \text{ nm}$ .

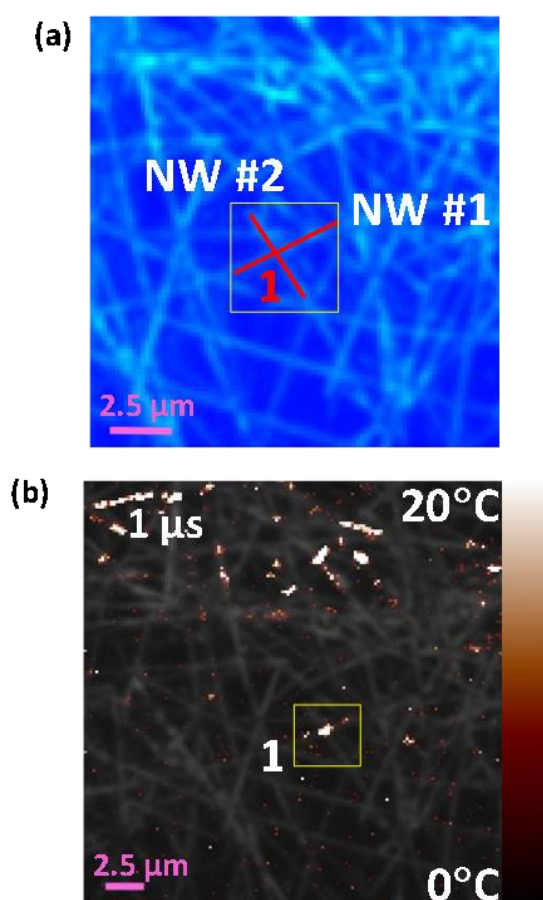


Fig. 5.3: (a) False color CCD image of randomly dispersed silver NW network showing several NWs and junctions with NW #1 and NW #2 highlighted in red lines; (b) TR image superimposed on grayscale CCD image to show the physical location of the hotspot at the junction. Yellow rectangles in (a) and (b) denote the same region (“location 1”).

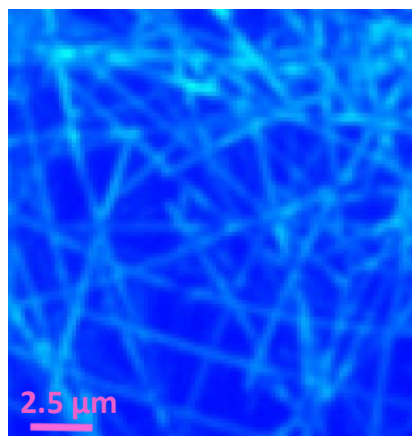


Fig. 5.4: False color CCD image of randomly dispersed silver NW network near location 1 showing several NWs and junctions.

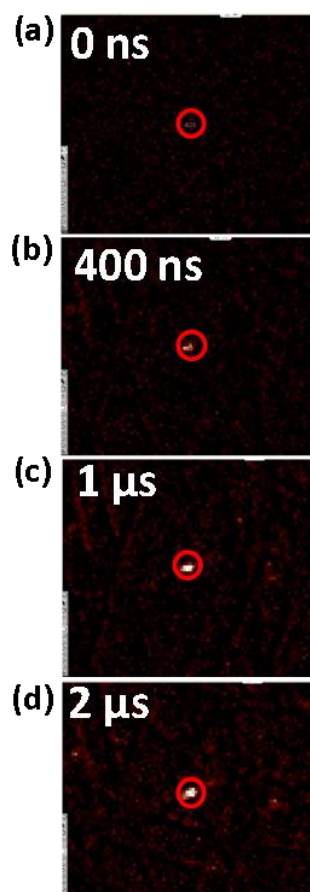


Fig. 5.5: TR images at different time (i.e. delay  $\tau_D$ ) show evolution of the local heating near the microscopic hotspot at location 1 at (a) 0 ns (b) 400 ns (c) 1 μs (d) 2 μs.

## 5.2.2 Determination of Thermal Time Constants

Fig. 5.6(a) shows a CCD image of another representative region of the network containing several NW-NW junctions. From the corresponding TR image (Fig. 5.6(b)) and merged CCD/TR image (Fig. 5.6(c)) at  $\tau_D = 1 \mu\text{s}$ , we see that only few of these NW-NW junctions (marked as location 2, 3 and 4 in Fig. 5.6(a)) form hotspots. The marked NW-NW junctions (hotspots) in Fig. 5.6 are spaced  $\sim 1 \mu\text{m}$  apart. This illustrates the inhomogeneity of the network and supports the observation that only a subset of the hotspots exhibit significant self-heating. The criterion used to define a hotspot is an average  $\Delta T \geq 3\text{K}$  within a  $7 \times 7$  pixel area ( $1.26 \mu\text{m} \times 1.26 \mu\text{m}$ ), generally encompassing a single NW-NW junction (i.e. a microscopic hotspot with dimensions of  $\sim$  hundreds of nanometers). For closely spaced hotspots, non-overlapping  $7 \times 7$  pixel areas have been chosen, with several pixels with  $\Delta T < 3\text{K}$  present in between the regions. As we discuss later (Fig. 5.10), this chosen spatial dimension is sufficient to enclose the local spatial profile associated with self-heating in the vicinity of a junction. The choice of a region consisting of multiple pixels also allows continuous monitoring of the time evolution in spite of small spatial drift (which we correct systematically), and results in an effective averaging of the local temperature profile over this multi-pixel region.

Fig. 5.7(a) shows the temperature evolution of the microscopic hotspots at location 2, 4, and 6 as a function of  $\tau_D$  during the heating cycle, obtained using 200 ns steps in  $\tau_D$  within the 0 - 10  $\mu\text{s}$  interval. The transient heating exhibits a single thermal time constant. Fig. 5.7(b) shows the  $\Delta T$  vs time during the cooling cycle.  $\Delta T$  decreases gradually until it reaches  $\sim 0.5\text{K}$ . A single thermal time constant is also observed in the cooling cycle.

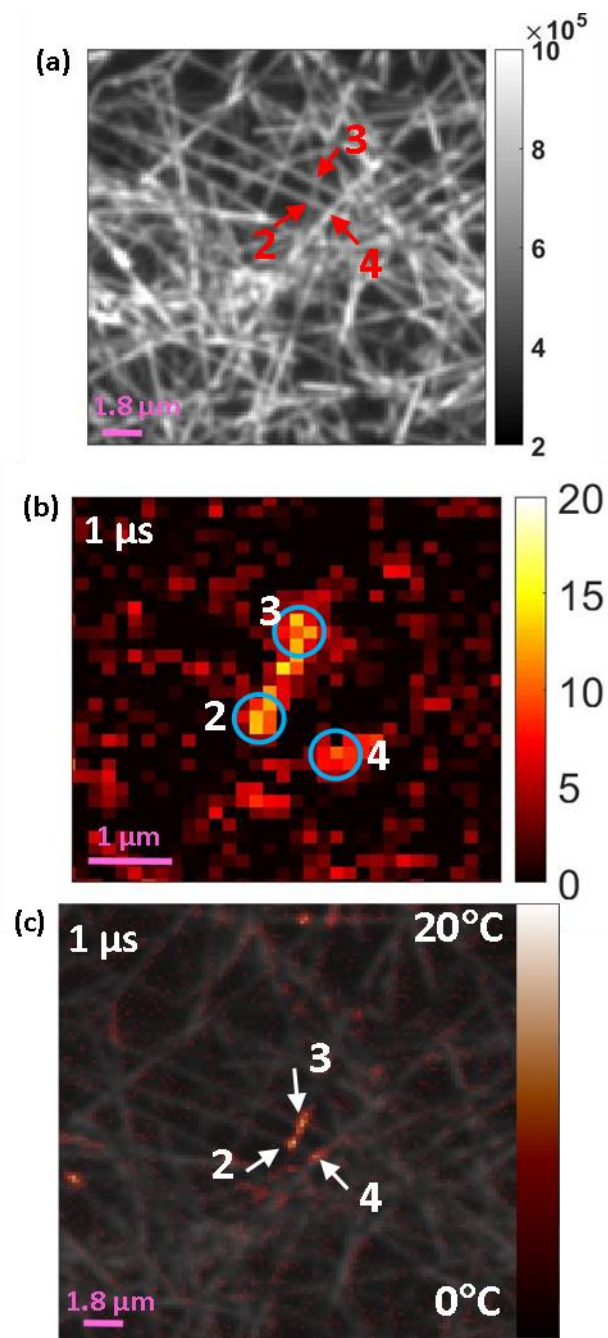


Fig. 5.6:(a) Several NW-NW junctions (location 2,3,and 4) are shown in a 100x grayscale CCD image of AgNW network; (b) Corresponding TR image at  $1 \mu\text{s}$ ;(c) Merged CCD and TR image at  $1 \mu\text{s}$  show formation of the microscopic hotspots at these NW-NW junctions.

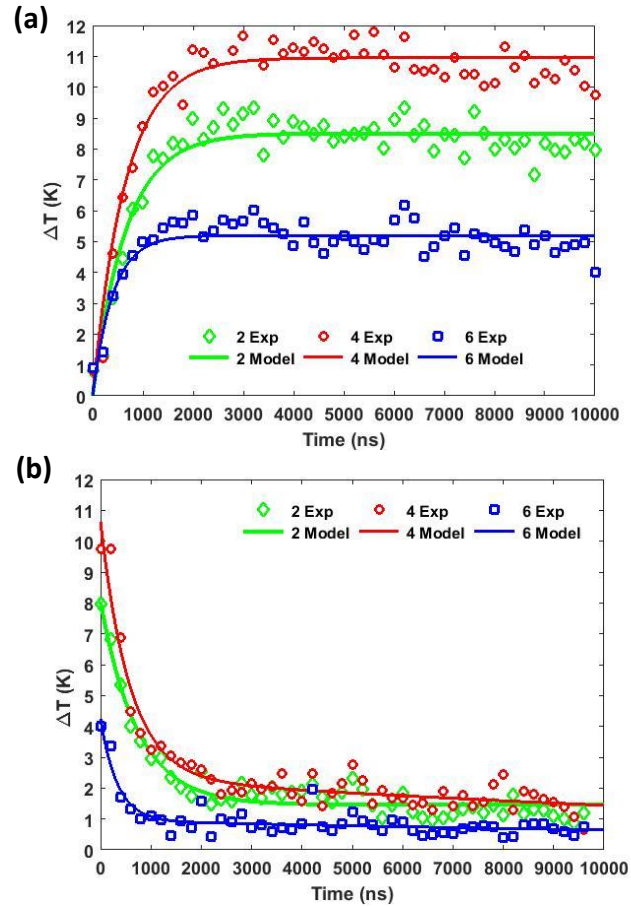


Fig. 5.7:  $\Delta T$  vs.  $\tau_D$  profiles of the hotspots located at 2, 4, and 6 during the (a) heating cycle (b) cooling cycle.

To quantify the transient dynamics, we fitted the data from the heating portion of the pulse with  $\Delta T = A_H (1 - e^{-\frac{t}{\tau_H}})$  where  $\tau_H$  is the thermal time constant, and  $A_H$  is the corresponding amplitude (see red solid line in Fig. 5.7(a)). Similarly, the cooling transient data has been fitted with  $\Delta T = A_C e^{-\frac{t}{\tau_C}}$ , where  $\tau_C$  and  $A_C$  are the time constant and amplitude, respectively. The thermal time constants and related steady state amplitudes are listed in Table 5.1.

Various hotspots within the network show qualitatively similar behavior with similar time constants, but varying maximum temperature change and weighting of the time constant. Table 5.1 shows  $\tau_H$ ,  $\tau_C$ ,  $A_H$ , and  $A_C$  values of representative hotspots at various locations within the network. A thermal image showing all these locations and the

probed hotspots is presented in Fig. 5.8. Note that hotspots located in close proximity (e.g. locations 2-4 or 5-6) do not necessarily have the same amplitude nor time constant.

Table 5.1: Amplitudes and thermal time constants of different hotspots

	Heating Cycle		Cooling Cycle	
	$A_H$ (K)	$\tau_H$ (ns)	$A_C$ (K)	$\tau_C$ (ns)
Location 1	$5.3 \pm 0.2$	$358 \pm 134$	$3.3 \pm 0.6$	$469 \pm 162$
Location 2	$8.5 \pm 0.2$	$663 \pm 100$	$6.1 \pm 0.6$	$563 \pm 118$
Location 3	$13.4 \pm 0.3$	$696 \pm 104$	$9.7 \pm 0.9$	$591 \pm 110$
Location 4	$11 \pm 0.2$	$655 \pm 93$	$8.3 \pm 0.9$	$581 \pm 134$
Location 5	$5.2 \pm 0.1$	$401 \pm 105$	$3.3 \pm 0.6$	$336 \pm 130$
Location 6	$5.2 \pm 0.3$	$345 \pm 138$	$3.6 \pm 0.6$	$296 \pm 96$
Location 7	$6.7 \pm 0.2$	$687 \pm 171$	$3.9 \pm 1$	$594 \pm 314$

The TR image at 400 ns (Fig. 5.8) shows the locations of the microscopic hotspots listed in Table 5.1. The zoomed CCD and thermal images of the microscopic hotspots located at location 4 and 6 are shown in Fig. 5.9. Thermal transient responses of these microscopic hotspots during the heating and the cooling cycle are shown in Fig. 5.7. Although the hotspots at locations 4 and 6 are close to other hotspots (2-3 and 5, respectively), the observed transients are qualitatively similar to those observed at location 1 as shown in Fig. 5.7 and Table 5.1.

Our prior study on graphene-silver NW based hybrid networks [76], performed at a lower magnification (20x) to observe heat-spreading effects through the channel, showed that the local self-heating at NW-NW junctions exhibited a significantly different thermal time constant than that of macroscopic heat-spreading through the channel ( $<1 \mu\text{s}$  vs.  $> 400 \mu\text{s}$ , respectively), and therefore these two effects (local self-heating at junctions vs. heat spreading through the network) could be isolated by considering the response components associated with the two distinctive time constants. In the current study, the observation of a single thermal time constant ( $\tau_H, \tau_C$ ) for time response to a  $10 \mu\text{s}$  pulse is consistent with the results of that prior local self-heating study. In both cases, the time constants are less than  $1 \mu\text{s}$  and do not vary systematically with distance from the electrical contacts within the channel region, but rather depend on the properties of the junction.

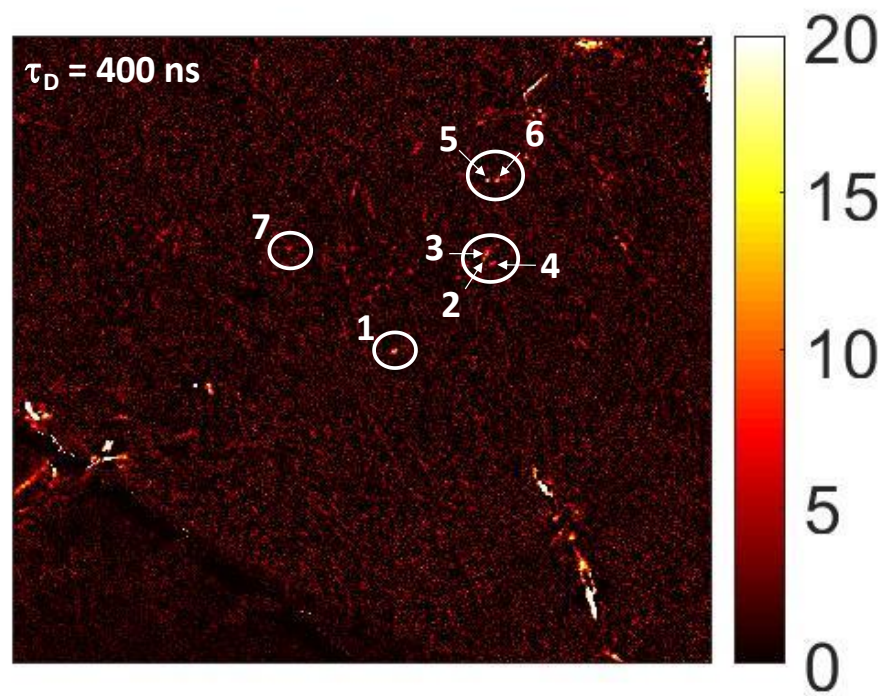


Fig. 5.8: TR image at 400 ns showing various microscopic hotspots. The values of amplitudes  $A$  and  $\tau$  of the circled hotspots are listed in Table 5.1.

It is unlikely that self-heating induced by the pulsed bias used in this experiment can significantly change the morphology of the NW-NW junctions of a previously-annealed silver NW network. The maximum hotspot  $\Delta T$  (25°C) observed within the channel region is much less than the typical annealing temperature (180°C - 300°C) [77-81]. However, higher-current operation would induce correspondingly higher junction temperatures, which would induce more substantial annealing effects [82].

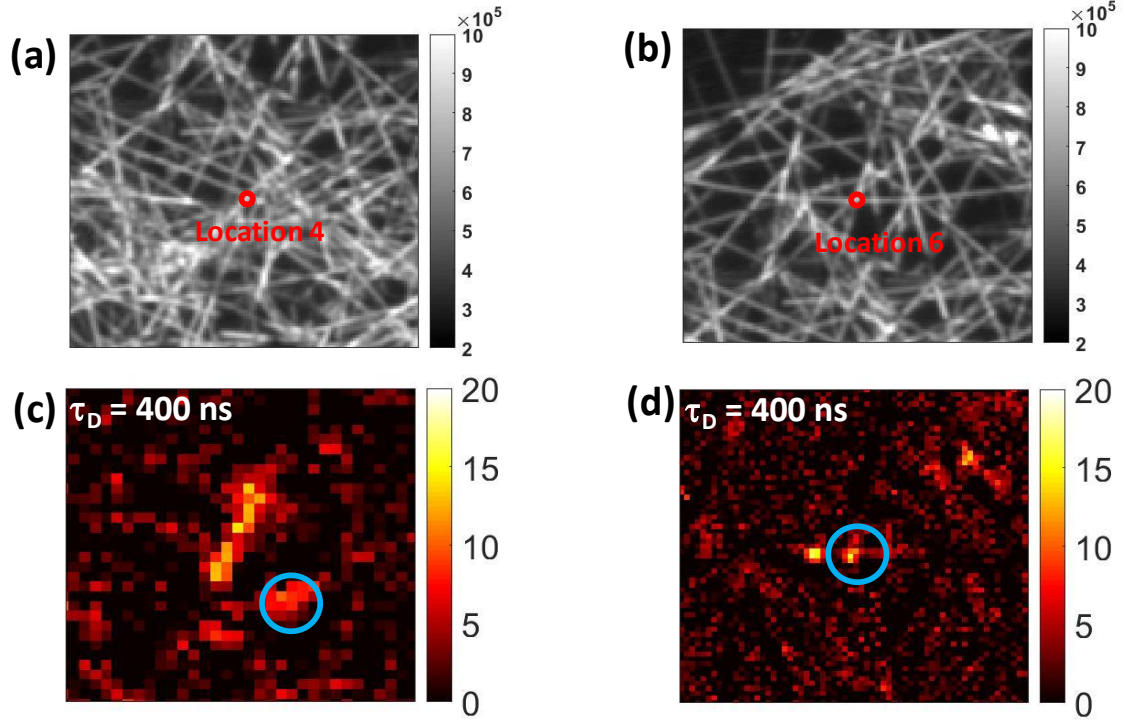


Fig. 5.9: (a,b) CCD images; (c,d) TR images at 400 ns of the microscopic hotspots located at locations 4 and 6.

### 5.3 Temperature Rise Vs Length Profile

Next, we quantify the spatio-temporal evolution of  $\Delta T$  of microscopic hotspots using high-resolution transient TR imaging which is essential to the knowledge of current transport in these networks. In order to understand the spatio-temporal dynamics of the hotspot at location 1 (Fig. 5.3(b)), we take  $\Delta T$  profiles along the lengths NW #1 and NW #2 (Fig. 5.3(a)) at different delay times ranging from 0-2  $\mu$ s, shown in Fig. 5.10. For both NWs, the profiles show distributed peaks near the NW-NW junction, and peak amplitude  $\sim 25$  K is reached at 2  $\mu$ s. It is interesting to observe that the widths of the two temperature profiles are different, with full width at half maximum (FWHM) of  $\sim 1$   $\mu$ m and  $\sim 500$  nm for NW #1 and NW #2, respectively. We will discuss the implication of this observation later. High spatial resolution obtained by TR imaging thus helps to probe  $\Delta T$  vs length profiles of adjacent hotspots that are spaced very close to each other. The parameters in our heat transfer model are obtained from fitting to the experimental  $\Delta T$  vs length profiles.

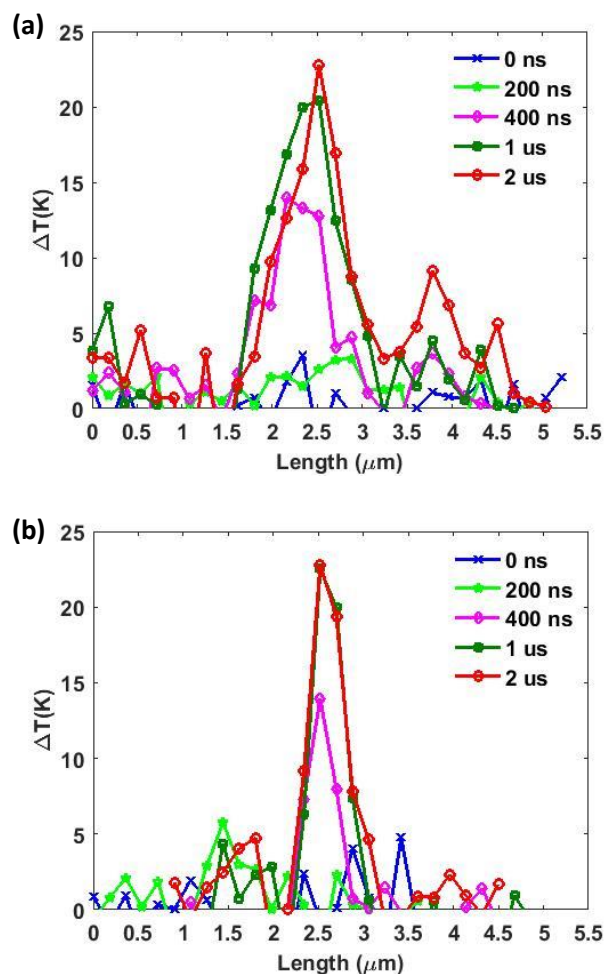


Fig. 5.10: (a)  $\Delta T$  vs length profiles along NW #1 and NW #2 at different time delays (0 ns – 2  $\mu\text{s}$ ).

#### 5.4 High-resolution Imaging of Adjacent Hotspots

Fig. 5.11 demonstrates another example of the ability of TR imaging to resolve closely-spaced hotspots. CCD image (Fig. 5.11(a)) shows several NW-NW junctions are present in these portion of the network. TR image at 400 ns (Fig. 5.11(c) and (d)) show two closely-spaced hotspots (distance  $\sim 1 \mu\text{m}$ ) at the intersection of NWs *B1* and *B2* (location 5) and NW *B1* and *B3* (location 6) respectively (labelled NWs are shown in Fig. 5.11(b)). In addition, there is another hotspot at the junction of NWs *B1* and *B4*, which is located  $\sim 900 \text{ nm}$  away from the junction of NWs *B1* and *B3*. Note that the fields of view are different but the yellow rectangles in Fig. 5.11(c) and Fig. 5.11(d) denote the same region.

Fig. 5.11(e) shows 0 – 2  $\mu$ s time evolution of  $\Delta T$  vs length profiles along NW B1. Thermal images illustrates that hotspots are formed selectively at few NW-NW junctions.

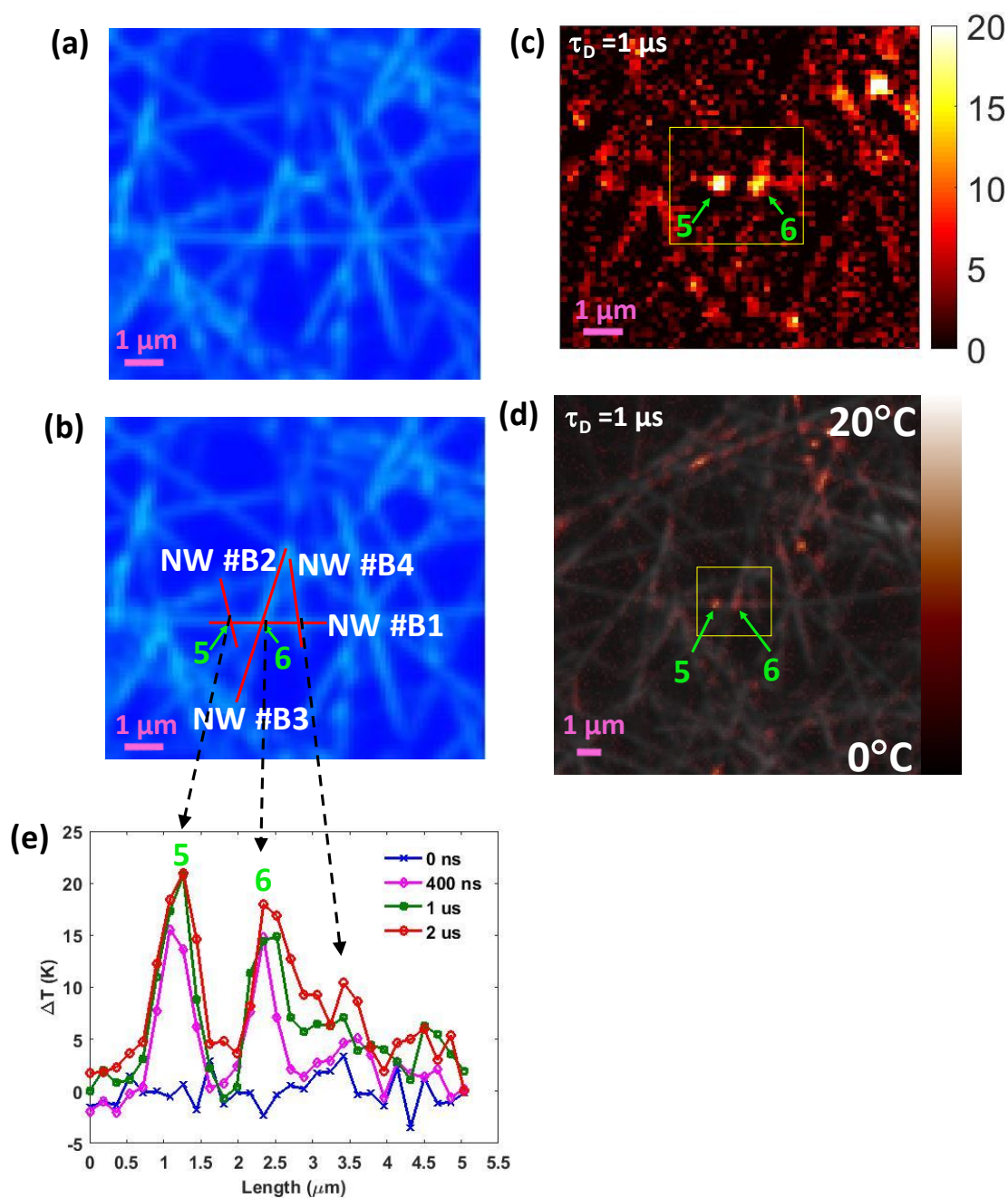


Fig. 5.11: (a) False color CCD image of portion of silver NW network showing several NW-NW junctions. (b) 4 NWs are labelled NW B1, B2, B3 and B4 that form junctions. (c) TR image at 1  $\mu$ s. Two hotspots within the yellow rectangle region are 5 pixels ( $\sim 1$

$\mu\text{m}$ ) apart. (d) CCD images and thermal image are merged to confirm that the hotspots (within yellow rectangle region) coincide with the NW-NW junctions. (e)  $\Delta T$  vs length profiles along NW B1 at different delays. Arrows indicate  $\Delta T$  peaks corresponding to each of the three indicated NW-NW junctions.

The observation of distinct profiles at the two hotspots indicates that the TR imaging technique can resolve the temperature profiles and that the length scale over which heat transfers from a NW into the quartz substrate is smaller than this distance. The temperature profiles and time dependence at closely-spaced hotspots (e.g. clusters of hotspots at locations 2-4 and 5-6) are qualitatively similar to those at isolated hotspots (e.g. locations 1 and 7), with significant quantitative variations observed even within a cluster (Table 5.1). The parameters in our heat transfer model are obtained from fitting to the experimental  $\Delta T$  vs length profiles.

## 5.5 Heat Transfer Model

### 5.5.1 Single Nanowire-Nanowire Junction Analysis

We develop a heat model with an aim to predict, within the limitations inherent to this complex, stochastic ensemble, the spatial temperature variation along the NW pair forming a hotspot at a junction as shown in Fig. 5.10 and also to determine the local thermal power generated at the junction. We consider a pair of NWs along with the underlying substrate as illustrated in Fig. 5.12(a). We assume geometrical symmetry such that the wires are of equal length and intersect each other at their respective centers. In order to model the observed hotspot, a junction heat rate,  $Q_C(W)$ , is considered to be generated at the intersection of the two wires. An amount of heat,  $Q_{top}$ , flows to the top wire, while  $Q_{bot}$  flows to the bottom wire. Heat flow rates going to the top and bottom wires are considered to be equally distributed on either side of the junction. In addition to the junction heat, a total uniform heat generation rate,  $q'''$  is also present due to Joule heating within the NW body. However, the effect of  $q'''$  is considered negligible compared to  $Q_C(W)$  in this analysis.

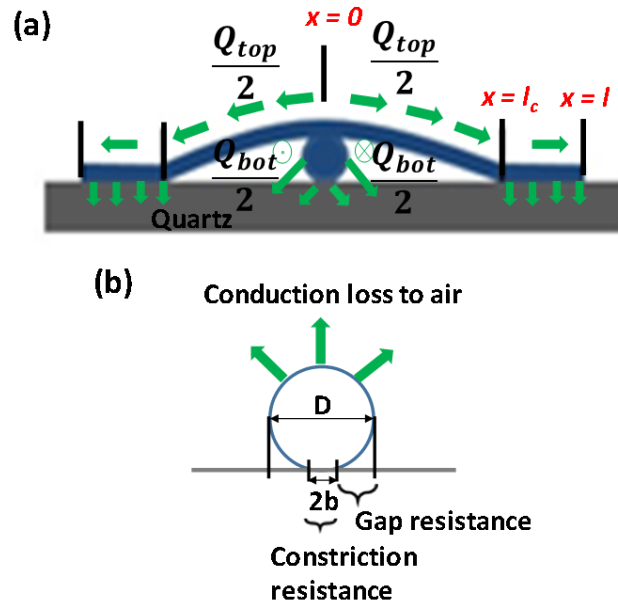


Fig. 5.12: Geometry for the heat transfer model. (a) Symmetry considered for the model and configuration of the top and the bottom NW along with the contact length  $l_c$ . (b) Thermal interface resistances (constriction and gap thermal resistance).

The bottom NW is assumed to be in contact with the quartz substrate, and therefore there is a heat loss pathway through conduction from the bottom NW to the substrate. This effect is considered through an interfacial thermal resistance between the NW and quartz. The interaction of the top NW with the bottom NW is restricted to the junction heat that it receives. Both NWs also lose heat through conduction to air at 300 K, but natural convection is not predominant at these small length scales.

Invoking symmetry, half the length of each NW is modeled as a one-dimensional transient fin problem with appropriate boundary conditions and heat loss terms. An additional consideration for the top NW is that it is in contact with the quartz substrate after a length  $l_c$ . Therefore, the only heat loss term before this contact is conduction to air. After the contact length  $l_c$ , both conduction loss to air and the quartz substrate are considered.

From a conventional energy balance equation and neglecting radiation effects,

$$E_{in} - E_{out} = E_{stored}$$

$$q_x - q_{x+dx} - q_{cond} - q_{subs} = E_{stored} \quad (5.1)$$

where  $q_{cond}$  is the conduction loss to air and  $q_{subs}$  is the conduction loss to substrate.

Now,  $q_{cond}$  can be written in the form of a heat transfer coefficient  $h$ . The value of  $h$  is derived from the conduction limit Nusselt number for flow over a cylinder [83]. The detailed calculation of  $h$  are given in section 5.7.  $q_{cond}$  involves the entire perimeter  $P$  when there is no contact with the substrate and only the half perimeter  $\frac{P}{2}$ , when the wire touches the substrate, because the other half is incorporated in the contact loss to the substrate.

$$q_{cond} = \begin{cases} h P (T(x) - T_{inf}) dx ; & x < l_c \\ h \frac{P}{2} (T(x) - T_{inf}) dx ; & x \geq l_c \end{cases} \quad (5.2)$$

Regarding  $q_{subs}$ , for a differential element of length  $dx$  it can be written as,

$$q_{subs} = \frac{(T(x) - T_{subs})}{R_{tot}'} dx \quad (5.3)$$

This equation is valid throughout the length of the bottom NW and for  $x > l_c$  for the top NW. Here,  $R_{tot}' \left(\frac{Km}{w}\right)$  is the interface thermal resistance normalized by contact length between the NW and the substrate.

Substituting  $q_{cond}$  and  $q_{subs}$  in Eq. (5.1), the governing equation for the bottom NW becomes,

$$\frac{\partial^2 T}{\partial x^2} - \frac{h \frac{P}{2} (T - T_{inf})}{kA} - \frac{(T - T_{subs})}{R_{tot}' kA} = \frac{\rho C}{k} \frac{\partial T}{\partial t} \quad (5.4)$$

The top NW is in contact with the substrate for  $x > l_c$  and is therefore governed by,

$$\begin{cases} \frac{\partial^2 T}{\partial x^2} - \frac{h P (T - T_{inf})}{kA} = \frac{1}{\alpha} \frac{\partial T}{\partial t} ; x < l_c \\ \frac{\partial^2 T}{\partial x^2} - \frac{h \frac{P}{2} (T - T_{inf})}{kA} - \frac{(T - T_{subs})}{R_{tot}' kA} = \frac{\rho C}{k} \frac{\partial T}{\partial t} ; x \geq l_c \end{cases} \quad (5.5)$$

The boundary conditions are the junction heat rate at the center of the wire and an isothermal tip condition ( $T = T_{inf}$ ) at the end of the wire  $l$ .

$$\left\{ \begin{array}{l} T = T_{inf}; \quad x = l \\ -k A \frac{\partial T}{\partial x} = \frac{Q_{top}(or Q_{bot})}{2}; \quad x = 0^+ \end{array} \right. \quad (5.6)$$

Details of the determination of the thermal interface resistance ( $R_{tot}$ ) is provided next.

### 5.5.2 Determination of Thermal Interface Resistance between Nanowire and Quartz

Thermal resistance  $R_{tot}$  is modeled based on the analysis presented in [84]. This overall interface resistance between the bottom NW and the substrate is a parallel network of the constriction resistance  $R_{cons}$  and the gap resistance  $R_{gap}$  as illustrated in Fig. 5.12(b).  $R_{cons}$  is the thermal resistance due to contact with the substrate and depends on the contact width  $2b$  which is a function of the van der Waals interaction energy between the wire and the substrate. On the other hand,  $R_{gap}$  comprises another heat flow pathway where the wire is not in direct contact with the substrate and the heat flow is expressed in terms of the thermal conductivity of the surrounding fluid (air)  $k_{air}$ . After estimating the contact width  $2b$  based on the van der Waals interaction force and the material properties of the wire ( $k_w$ ) and substrate ( $k_s$ ), the thermal resistances are determined according to [84]. The equations are as follows,

$$R_{cons} = \frac{1}{\pi k_w(dx)} \ln\left(\frac{2D}{b}\right) - \frac{1}{2k_w(dx)} + \frac{1}{\pi k_s(dx)} \ln\left(\frac{D}{\pi b}\right) \quad (5.7)$$

$$R_{gap} = \frac{1}{2 k_{air} (dx) [\cot\left(\sin^{-1}\left(\frac{2b}{D}\right)\right) - \left(\frac{\pi}{2} + 1\right)]} \quad (5.8)$$

$$R_{tot} = \frac{R_{cons} R_{gap}}{R_{cons} + R_{gap}} \quad (5.9)$$

The surface approach separation distance  $l_s$  and the Hamaker constant  $A_H$  are key parameters in determining the van der Waals force of interaction and eventually the contact width  $2b$ . Hamaker constant  $A_H$  is a material property that measures the relative strength of attractive van der Waals force between two surfaces. A separation distance  $l_s$  of 0.2 nm

is a reasonable assumption for this case [85]. The Hamaker constant for the NW-quartz-air system  $A_H$  is calculated as shown below from the Hamaker constants for silver ( $20.3 \times 10^{-20}$  J) and silicon dioxide ( $6.55 \times 10^{-20}$  J) [86] and is determined to be ( $11.53 \times 10^{-20}$  J). Note that the value for silicon dioxide is used instead of quartz.

$$\begin{aligned} A_H(\text{AgNW} - \text{air} - \text{quartz}) &\approx A_H(\text{AgNW} - \text{air} - \text{SiO}_2) \\ &= \sqrt{A_H(\text{Ag} - \text{Ag}) A_H(\text{SiO}_2 - \text{SiO}_2)} \end{aligned}$$

The contact width,  $2b$ , is calculated the following way:

$$2b = \left( \frac{16 F_{vdw} E_m D}{\pi} \right)^{\frac{1}{2}} \quad (5.10)$$

Here,  $E_m$  is the effective modulus of elasticity defined as

$$E_m = \frac{1}{2} \left[ \frac{1 - \nu_s^2}{E_s} + \frac{1 - \nu_w^2}{E_w} \right] \quad (5.11)$$

Here,  $\nu_s$  and  $\nu_w$  are the Poisson ratios of substrate and NW respectively.  $E_s$  and  $E_w$  are the modulus of elasticity of substrate and the NW respectively.

The van der Waals force  $F_{vdw}$  is calculated the following way,

$$F_{vdw} = - \frac{A_H}{\pi} \int_0^D \frac{\sqrt{(D-y)y}}{(y+l_s)^4} dy \quad (5.12)$$

Here,  $A_H = 11.53 \times 10^{-20}$  J is the Hamaker constant discussed earlier and  $l_s = 0.2$  nm is the separation distance between two bodies approaching contact.

Using the above analysis, the estimated  $R_{tot}$  is used to calculate the conduction loss term to the substrate  $q_{subs}$ .

Table 5.2 summarizes the material and thermal parameters that are used for calculation of  $R_{tot}$  and are used in the simulation. Calculated values of  $R_{tot}$  and other derived parameter values are summarized in Table 5.3.

Table 5.2: Summary of the material and thermal properties.

Material Parameters	Values
Mass density of silver, $\rho$	10490 Kg/m <sup>3</sup>
Specific heat capacity of silver, C	235 J/KgK
Heat transfer coefficient, h	1.2×10 <sup>5</sup> W/m <sup>2</sup> K
Thermal conductivity of silver NW, $k_w$	200 W/mK[87]
Thermal conductivity of quartz, $k_s$	2 W/mK
Thermal conductivity of fluid (air), $k_{air}$	0.026 W/mK
Poisson ratio of quartz, $\nu_s$	0.17
Poisson ratio of silver NW, $\nu_w$	0.37[88]
Modulus of elasticity of quartz, $E_s$	71.6×10 <sup>9</sup> N/m <sup>2</sup>
Modulus of elasticity of silver NW, $E_w$	83×10 <sup>9</sup> N/m <sup>2</sup> [88, 89]

Table 5.3: Summary of the derived parameters.

Material Parameters	Values
Hamaker constant, $A_H$	11.53×10 <sup>-20</sup> J
Effective modulus of elasticity, $E_m$	1.198×10 <sup>-11</sup> N/m <sup>2</sup>
van der Waals force, $F_{vdw}$	-4.0244 N
Contact width, 2b	4.9554 ×10 <sup>-9</sup> m
Constriction thermal resistance, $R_{cons}$	2.27×10 <sup>5</sup> K/W
Gap thermal resistance, $R_{gap}$	5.44×10 <sup>5</sup> K/W
Interface thermal resistance, $R_{tot}$	1.605×10 <sup>5</sup> K/W
Thermal conductance between NW and Quartz, $G$	3.45 W/Km

The two unknown parameters are the junction heat rate  $Q_C$  and the contact length  $l_C$ , which are estimated by fitting the experimental and simulated temperature profiles. Therefore, the model detailed here can estimate the temperature profile of each individual NW and the temperature evolution with time based on a macroscale 1-D transient fin analysis. We have taken the value of the thermal conductance ( $G = \frac{1}{R_{tot}}$ ) between the NW and the quartz substrate to be 10 times the estimated value from the thermal model ( $G_{Theoretical} = 3.45 \frac{W}{mK}$ ) since the actual thermal conductance could be greater than the theoretical value if the NW-substrate contact area is higher than the ideal line contact that

has been assumed in the theoretical model. This premise is experimentally verified using AFM measurements, the details of which are described in section 5.9. Therefore, an estimate of the local heat generated at the junction of the two NWs is obtained using this model.

The governing differential equations (Eq. (5.4) and Eq. (5.5)) with the boundary condition (Eq. (5.6)) are solved using a finite volume approach in which an equation is discretized into a system of algebraic equations. An implicit time advancement scheme is used in the discretization and the resulting algebraic equations are solved using Gauss-Seidel iteration. 20 elements are used to mesh the half length of the NW of  $2.7 \mu\text{m}$ , and a time step of  $20 \text{ ns}$  is used. The fitting parameters  $l_c$ ,  $Q_{top}$  and  $Q_{bot}$  are varied to match the temperature at the center of the NWs with that observed from the TR measurements. The time at which the match is checked is a quasi-steady state value of  $1 \mu\text{s}$ . The substrate and air temperatures are assumed to be  $300 \text{ K}$ . An initial temperature of  $300 \text{ K}$  is set at all grid points, and the temperature field is allowed to evolve in time, with the temperature profile iterated to converge at each time step.

Fig. 5.13 shows the simulated temperature profiles for the top and bottom wires in solid lines. The peak temperature matches the experimental results when a junction heat of  $0.16 \text{ mW}$  ( $Q_{top}$ ) goes to the top wire and  $0.25 \text{ mW}$  ( $Q_{bot}$ ) goes to the bottom wire, with a substrate contact length for the top wire of  $l_c = 270 \text{ nm}$ . Therefore, total power generated at this hotspot is  $P_{Model} = 0.16 + 0.25 = 0.41 \text{ mW}$ . Also, the bottom NW exhibits a slightly steeper fall as expected because it is in contact with the substrate. Thermal power going to the bottom NW ( $\sim 60\%$ ) is greater than that for the top NW ( $\sim 40\%$ ) due to contact with the substrate in the immediate vicinity of the junction. This also implies that the experimental profiles observed in Fig. 5.10 can be interpreted as NW #1 on top of NW #2. The numerical results obtained from the heat transfer model are compared to the experimental results of Fig. 5.10. The simulation results correctly capture the experimental trends with distance along the NW. In addition, we find that the substrate contact length  $l_c = 270 \text{ nm}$  assumed in the heat transfer model is consistent with the configuration of the NWs in the network as confirmed by AFM measurements (Fig. 5.17).

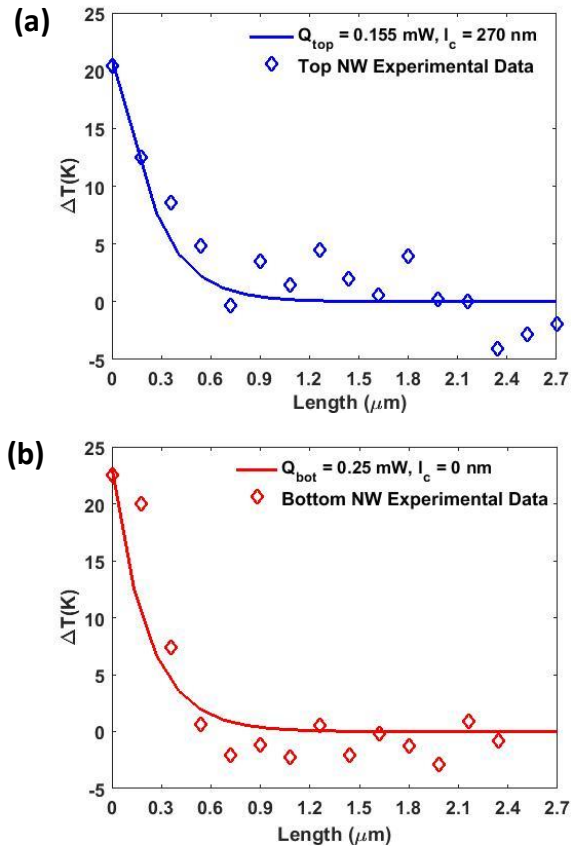


Fig. 5.13: Comparison of experimental data at  $1 \mu\text{s}$  with numerical results from the heat transfer model (a) for the top NW (i.e. NW #1) (b) bottom NW (i.e. NW #2).

Next, we compare the total electrical power dissipated in the network (voltage times current) against an estimate of the sum of microscopic power at all the hotspots calculated from the heat transfer model. The total electrical power,  $P_{\text{Measured}} \sim 1.68 \text{ V} \times 50 \text{ mA} = 84 \text{ mW}$ . Using a binary image (discussed later section in 5.8, Fig. 5.16) created from the TR image at  $1 \mu\text{s}$  (a representative  $\Delta T$  at which most of the hotspots have reached steady state) and extrapolation to the overall device area yields an estimate for the total number of hotspots in the network of  $\sim 200$ . Details of construction of the binary image and extraction of the number of hotspots are presented in section 5.6. Therefore, one can estimate an average power at each hotspot,  $P_{\text{Average}} \approx \frac{84 \text{ mW}}{200} = 0.42 \text{ mW}$ . Assuming that the hotspot at location 1 is representative of those throughout the network, the estimated  $P_{\text{Average}}$  is in reasonable agreement with  $P_{\text{Model}}$ .

The heat transfer model can be extended to analyze multiple hotspots in close spatial proximity through the addition of appropriate boundary conditions at the junctions (next section). The spatial profiles obtained from the multiple-hotspot model show reasonable agreement with the measured profiles for two hotspots located within a distance of  $\sim 1.5 \mu\text{m}$ , including the profile along the common NW and those along the two crossing NWs.

The average electrical current per hotspot,  $I_{Average}$ , can be estimated by considering the channel as a series of concentric regions, each carrying the total current  $I_{Total} \approx 50 \text{ mA}$ . This yields  $I_{Average} \approx \frac{I_{Total}}{n_{Region}}$  where  $n_{Region}$  is the number of hotspots in each of the concentric regions. The resulting  $I_{Average} \approx 2 - 7 \text{ mA}$ , along with the average power at each hotspot, can be used to estimate an average NW-NW junction resistance,  $R_{Average} = \frac{P_{Average}}{I_{Average}^2} \approx 8 - 100 \Omega$  which falls within the range of typical NW-NW junction resistance reported in the literature [90, 91].

### 5.5.3 Multiple Nanowire-Nanowire Junctions Analysis

The heat model used in the single microscopic hotspot analysis is also applicable to analyze multiple hotspots within close proximity. The model can be used to estimate generated thermal power at the hotspots at location 5 (i.e. junction of NW B1 and B2) and location 6 (i.e. junction of NW B1 and B3) shown in Fig. 5.11. The heat model described in the study can be extended by including a boundary condition at the second junction. In this analysis, the length of the wires between the two junctions along NW B1 is modeled with the junctions as the boundaries. Also, the experimental  $\Delta T$  vs length profiles are not clearly indicative of the relative positions of the pair of wires with respect to being at the top or at the bottom, because the characteristic width of the temperature decay profile is nearly the same for all three wires. Therefore, we assume NW B1 to be the bottom NW at both junctions for the thermal analysis.

The heat transfer modeling aspects remain the same for the top NWs i.e. NW B2 and B3 at the two junctions. For NW B2, the junction heat rate is predicted to be  $Q_{Loc5 B2 Top} = 0.24 \text{ mW}$  and for NW B3  $Q_{Loc6 B3 Top} = 0.19 \text{ mW}$ . Fig. 5.14(a) and (b) show that a good agreement is obtained with the experimental profiles for these values of junction heat. For NW B1, the length between the junctions ( $\sim 0.8 \mu\text{m}$ ) is modeled. The junction heat rates at both boundaries are unknown and varied to fit the junction temperature at the two ends. Fig. 5.14(c) shows that a reasonable match with the

experimental  $\Delta T$  vs length profile of NW B1 is obtained. The temperature decay for the modeled profile is not as pronounced but the rise near the junctions is well predicted. Heat rates of  $Q_{Loc5 B1 Bot} = 0.26 \text{ mW}$  and  $Q_{Loc6 B1 Bot} = 0.18 \text{ mW}$  are obtained for NW B1 at junction location 5 and 6 respectively. The total heat produced at the hotspot at location 5 is determined to be  $Q_{Loc5} = Q_{Loc5 B2 Top} + Q_{Loc5 B1 Bot} = 0.24 + 0.26 = 0.50 \text{ mW}$  and the total heat produced at the hotspot at location 6 is  $Q_{Loc6} = Q_{Loc6 B3 Top} + Q_{Loc6 B1 Bot} = 0.19 + 0.18 = 0.37 \text{ mW}$ . As expected, the heat power is higher for the junction with higher temperature (i.e. location 5).

We see that for both locations, approximately equal percentage of the generated power goes to the top and the bottom NW. In location 5(6), 52% (49%) of the total generated power goes to the bottom NW and 48% (51%) goes to the top NW. Unlike the single junction analysis presented previously, a much shorter length has been analyzed for the two-junction scenario ( $0.8 \mu\text{m}$  compared to  $2.7 \mu\text{m}$  for the single junction). Therefore, even though the contact length ratios are the same (i.e.  $l_c = 0.1 l$ ), the total length in contact with the substrate for heat dissipation to the substrate from the bottom NW reduces. Moreover, the experimental  $\Delta T$  at the junction of the top and the bottom NW are almost the same for both locations ( $\sim 21 \text{ K}$  at location 5 and  $\sim 16 \text{ K}$  at location 6) as seen from the Fig. 5.11(e). Therefore, we see that the generated thermal power at a junction and the percentages that goes separately to the individual NWs can be determined from the  $\Delta T$  at the junction and spatial  $\Delta T$  vs length profiles along the NWs. Note that a higher value of thermal contact conductance between the NW and the quartz substrate will result in a better prediction of the temperature decay.

Furthermore, the power generated at location 5 and 6, as obtained from the fitting, can be qualitatively related to the local current flowing through the NW-NW junctions at those spatial locations. Since the silver NW network is annealed, we can assume that electrical junction resistances of the network at different spatial locations are similar [90]. Therefore,

$$Q_{Loc5} = 0.50 \text{ mW} = I_5^2 R, \text{ and } Q_{Loc6} = 0.37 \text{ mW} = I_6^2 R$$

where  $I_5$  and  $I_6$  are the local currents at the junctions at location 5 and 6 respectively and  $R$  is the junction resistance. Hence, we obtain,

$$\frac{I_5}{I_6} \cong 1.2$$

i.e., local current flowing through the junction at location 5 is  $\sim 1.2$  times higher compared to the local current flowing through the junction at location 6.

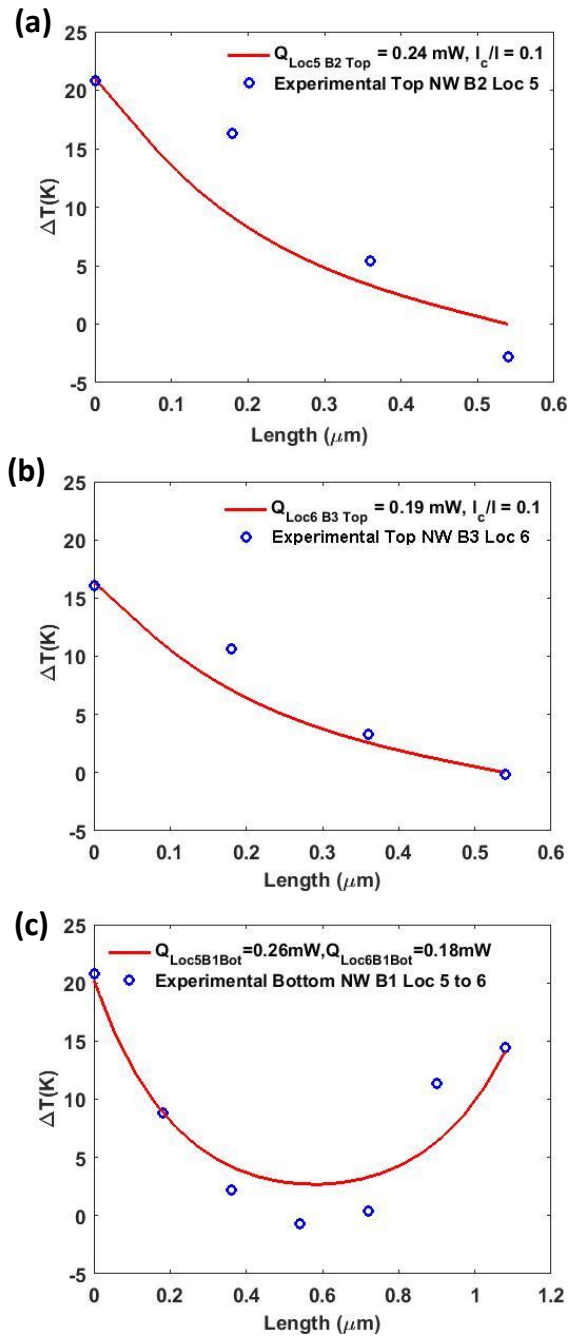


Fig. 5.14: Comparison of experimental data with numerical results from the heat transfer model (a) top NW B2 at location 5 (b) top NW B3 at location 6 (c) bottom NW B1 from location 5 to 6.

## 5.6 Construction of Binary Mask

For the thermal transient analysis, a masking algorithm was devised to select only the NW pixels and to eliminate substrate pixels. Fig. 5.15 shows the binary mask created from the grayscale CCD image where pixels with CCD intensity greater than a threshold intensity (Grayscale value  $\sim 375500$ ) have been selected for analysis. This threshold intensity is chosen in a way such that the percentage of pixels considered for analysis (representing NW bodies and junctions) matches the area fill factor of NWs ( $\sim 20\%$ ) in the fabricated NW network samples. Fill factor of fabricated sample is calculated in the following way:

$$\begin{aligned}
 \text{Fill factor} &= \frac{\text{Projected Area of NWs}}{\text{Area of sample}} \\
 &= \frac{\text{Total Number of NWs} \times \text{NW Length} \times \text{NW Width}}{\text{Area of Sample}} \\
 &= \frac{4.8 \times 10^6 \frac{1}{\text{cm}^2} \times 90 \times 10^{-7} \text{cm} \times 40 \times 10^{-4} \text{cm}}{1 \text{cm} \times 1 \text{cm}} \sim 20\%
 \end{aligned}$$

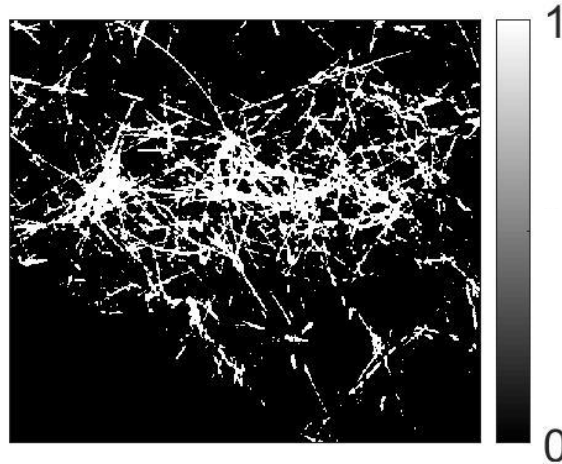


Fig. 5.15: Binary mask obtained from grayscale CCD image. This mask was used to select pixels corresponding to NW locations, and to eliminate pixels corresponding to areas without NWs.

## 5.7 Determination of Heat Transfer Coefficient $h$

The heat transfer coefficient,  $h$ , represents conductive and convective losses from the NW to the surrounding air. For a NW diameter of  $\sim 100$  nm, the natural convective losses can be neglected because the Rayleigh number ( $Ra = Gr \cdot Pr$ ) is very small (close to zero). Here,  $Gr$  is the Grashoff number and  $Pr$  is the Prandtl number. Therefore, the heat transfer coefficient can be taken in the conduction limit. From [83], a good approximation for the pure conduction limit  $Nu$  number for a body of any shape can be taken as 3.47. Using the relationship between  $Nu$  number and  $h$  ( $Nu = hL/k_{medium}$ ), we obtain a heat transfer coefficient  $h$  of  $1.2 \times 10^5 \frac{W}{m^2K}$ . Here, the characteristic length ' $L$ ' is taken as the square root of the surface area of a single NW ( $L = \sqrt{A}$ ) and  $k_{medium}$  is the thermal conductivity of the convective medium (air).

## 5.8 Determination of Number of Hotspots

In order to determine the total number of hotspots within the entire  $100 \mu\text{m} \times 100 \mu\text{m}$  network area (i.e. within the field of view of the 100x objective lens), we used a customized MATLAB script to construct a binary image from the corresponding TR image at  $1 \mu\text{s}$  (Fig. 5.16(a)) considering only the pixels that have  $\Delta T$  greater than or equal to a threshold temperature change (8K in this case). Joule heating due to the applied electrical power occurs mostly at these hottest hotspots. The binary image is shown in Fig. 5.16(b). This threshold temperature represents  $\sim 5\%$  of the hottest pixels within the network. The MATLAB script is then used to obtain the total number of hotspots in the network  $\sim 200$  from Fig. 5.16(b) from the total number of the islands of connected pixels.

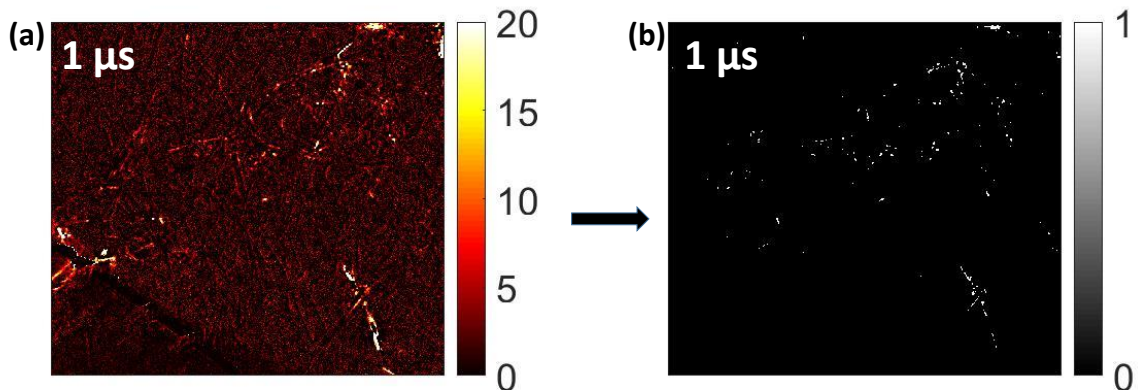


Fig. 5.16: (a) TR image at 1  $\mu$ s; (b) Binary image created from (a), showing all pixels with  $\Delta T$  greater than or equal to 8K. The binary image is used to calculate the approximate number of hotspots within the network.

## 5.9 Determination of Substrate Contact Length of Nanowire

In order to determine whether the value of the substrate contact length of the top NW,  $l_c$ , used in the model is consistent with the physical geometry, we performed AFM measurements of annealed silver NW networks. Conventional AFM measurements are done (DI3100, Bruker) in ambient conditions in tapping modes with the simultaneous acquisition of phase images. N type Si tip, purchased from AppNano, has been used for the measurements. Considering the flexibility of the NWs, a slow line scan rate of 1 Hz with scan speed of  $\sim 2.8 \mu\text{m/s}$  has been employed to acquire stable images. Fig. 5.17(a) shows topography of a NW-NW junction and Fig. 5.17(b) and (c) show 3-D views of the same junction from two different angles. The images show NW C1 (along profile 2) with diameter  $\sim 40 \text{ nm}$  and NW C2 (along profile 3) with diameter  $\sim 100 \text{ nm}$ . Since the overall height at the junction is the sum of these diameters, it appears that the two NWs are in contact at the junction. Height profiles along the NWs and the substrate are shown in Fig. 5.17(d) to determine  $l_c$ . Near the junction, profile 2 (taken along NW C1) is slightly wider than profile 3 (taken along NW C2) indicating that NW C1 is the top NW. In order to determine  $l_c$ , we first estimate the tip broadening factor from profile 3 using the width of the peak ( $\sim 170 \text{ nm}$ ) and the height of the peak ( $\sim 40 \text{ nm}$ ); tip broadening factor =  $170 - 40 = 130 \text{ nm}$ . We obtain  $l_c$  of the top NW C1 by deducting tip broadening factor from the distance between the peak of profile 2 and the baseline. Note that the distance between baseline and the peak in profile 2 are different for the two sides of the NW-NW junction along NW C1. For the left side,  $l_c = 455 - \frac{130}{2} = 390 \text{ nm}$  and for the right side,  $l_c = 150 - \frac{130}{2} = 85 \text{ nm}$ . This value is consistent with  $l_c = 270 \text{ nm}$  used in the heat transfer model. Based on the NW deposition method, annealing conditions etc. we expect similar  $l_c$  values for other NW pairs.

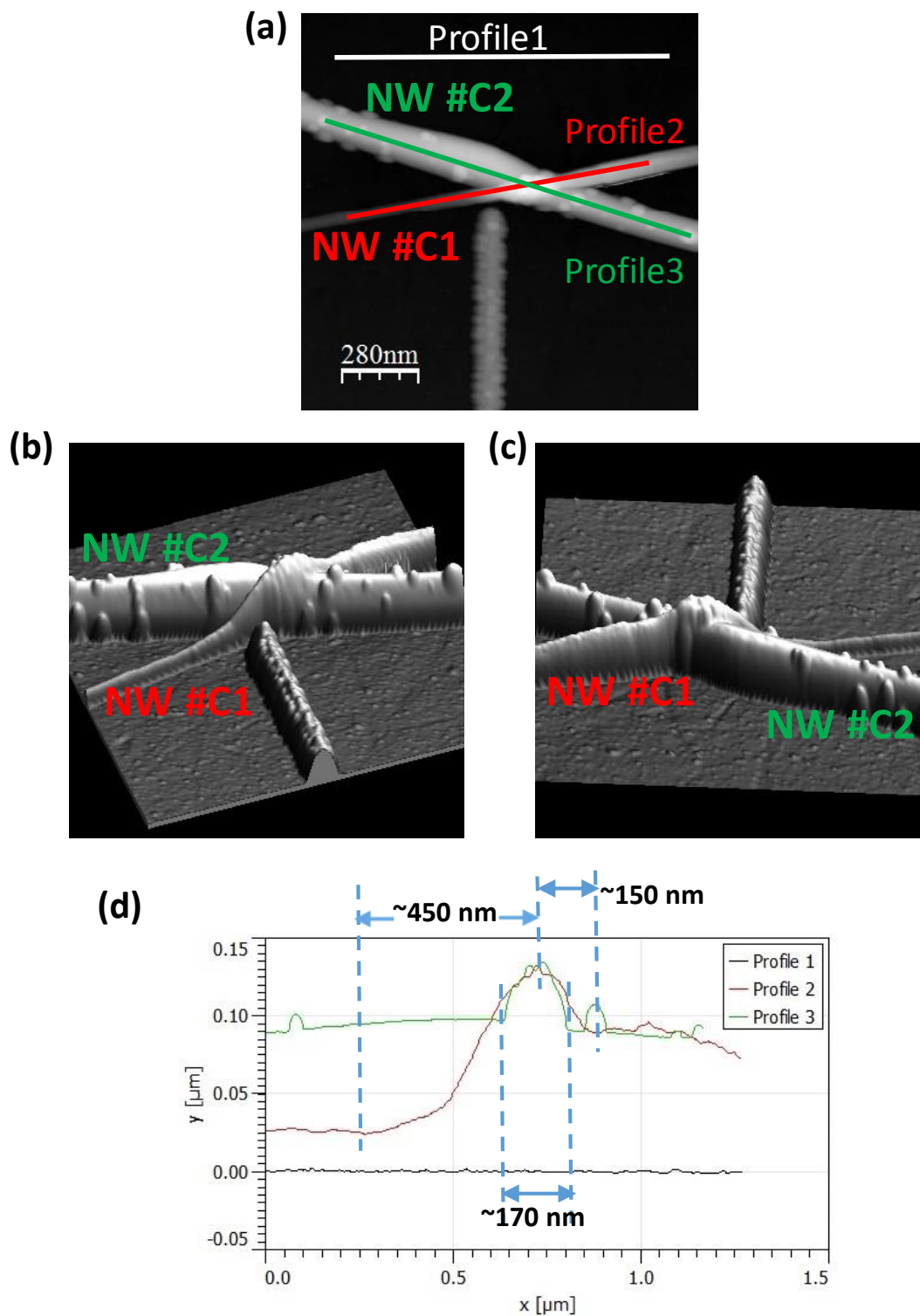


Fig. 5.17: AFM image showing configuration of a representative NW-NW junction (a) 2-D view; (b) (c) 3-D views from two different angles; (d) Height profiles for this NW pair.

### 5.10 Circuit Representation of Hotspots in Silver Nanowire Network

A silver NW network can be represented by a resistor network where each of the resistor component represents NW-NW junction resistance. Fig. 5.18 shows such a resistor network representing current conducting pathways through a portion of a silver NW network. Between the electrical contacts, two locally well-connected portions of the network (with lower effective resistance of  $R$ ) are connected through resistor  $R_1$  ( $R \gg R_1$ ) which are otherwise globally disconnected. Hotspots are formed at this high resistance point of the network. The maximum heating occurs at such weak points of the most current conducting pathways.

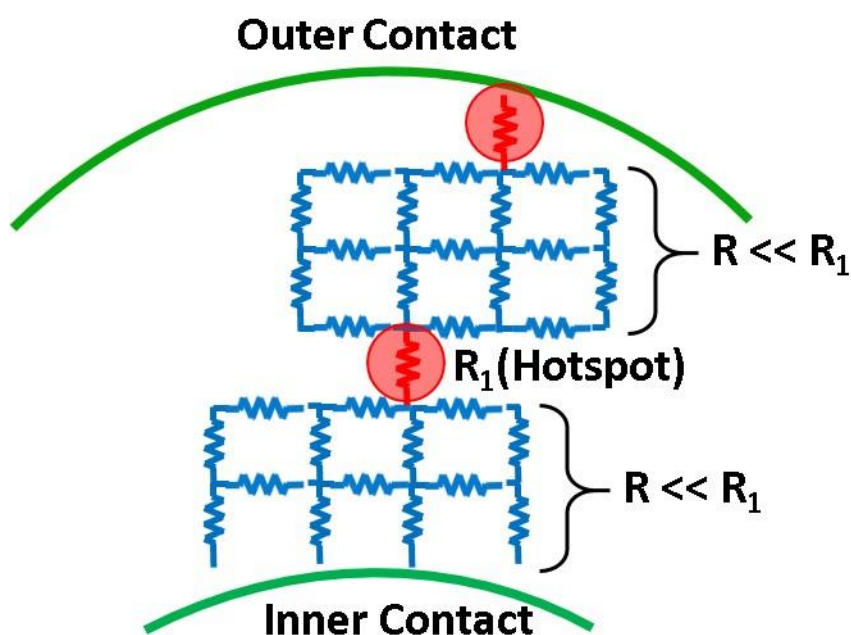


Fig. 5.18: A resistor network representing current conducting pathways in silver NW network.

## 5.11 Broadening of Temperature Profiles

Due to optical diffraction limit, TR imaging of sub-diffraction feature sizes leads to underestimation of hotspot temperature [92] and broadening of temperature profiles taken along NW lengths. The spatial resolution  $R$  of an imaging system can be defined by,

$$R = 1.22\lambda N = \frac{0.61 \lambda}{\text{Numerical Aperture}}$$

Here,  $N$  is the f-number of the objective lens. In this microscopic hotspot study, we have used a green LED ( $\lambda = 530 \text{ nm}$ ) to probe the relative surface reflectance change and the numerical aperture of the 100x objective lens used is 0.75. This gives,  $R \cong 430 \text{ nm}$ . Note that the pixel dimension in this TR measurement setting is  $\cong 200 \text{ nm}$ .

In order to find out the broadening of our experimental temperature rise ( $\Delta T$ ) vs length profiles due to the optical diffraction, we determine the spread of the surface reflectance profile considering that temperature rises as delta function (i.e. in pulses) at NW-NW junctions that encompass one pixel (-100 nm to 100 nm). The pulse temperature rise is shown in Fig. 5.19(a). The pulse height,  $\Delta T$ , is taken 25K here. We consider an optical energy profile  $f(r)$  (i.e. a point spread function) determined by Airy disk, and approximated by a Gaussian distribution [92],

$$f(r) \cong \frac{1}{\sqrt{2\pi}} \exp\left[-\frac{\left(\frac{2.44 r}{\lambda N}\right)^2}{2}\right] \quad (5.13)$$

The resulting temperature Gaussian profile ( $f(r) \times \Delta T$ ) is shown in blue in Fig. 5.19(b) where ~51% of the probed reflected optical energy is confined in that pixel (-100 nm to 100 nm) and ~22.5% spread to the immediate adjacent pixels. This also shows lowering of temperature at that pixel from 25K to ~ 14K. Taking FWHM as the effective broadening, we determine a spatial broadening of ~ 400 nm from the Gaussian profile. The red histograms at each of the pixels represent an average of the Gaussian profile. The function  $f(r)$  thus provides a weighing function to determine the broadening due to optical diffraction.

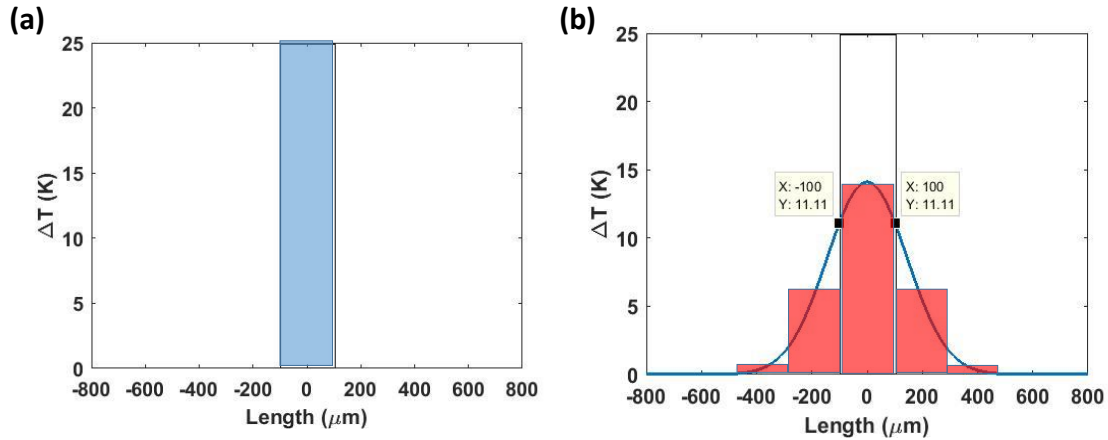


Fig. 5.19: (a) Pulse temperature rise at NW-NW junction; (b) the broader temperature profile (blue Gaussian curve) resulting from optical diffraction as captured by the 100x objective lens showing underestimation of temperature. Histogram (shown in red) is estimated by averaging the Gaussian temperature curve at each pixel.

## 5.12 Conclusion

In summary, we use high-resolution TR measurements to take thermal images of the microscopic hotspots that are formed at NW-NW junctions in a silver NW network. We have observed the spatial spreading of heat from the microscopic hotspot and discussed its temporal thermal response. We quantitatively determined the thermal time constants associated with local heating and cooling. We obtained temperature profiles along the length of the NWs ( $\Delta T$  vs length). We model the thermal behavior using heat transfer equations and a finite element analysis (FEA) taking into account the NW-substrate interactions and conduction loss to air. We obtained the interface resistance between NW and substrate. We also estimated the local power generated due to Joule heating by fitting the experimental  $\Delta T$  vs length profiles with numerical results from our heat model. TR thermal images along with the parameters we obtained e.g. thermal interface resistance, generated local power at the junctions, number of hotspots, hotspot temperatures and associated thermal transients, help us to understand the coupled electro-thermal transport in disordered network systems. The hotspots are expected to exhibit similar transient thermal responses even if NW length, density etc. are varied as long as the microscopic configuration (e.g. thermal environment) of the junctions remains the same with similar annealing condition and the junctions are separated by at least a distance equivalent to heat diffusion length of  $\sim 1 - 1.5 \mu\text{m}$ . Collectively, these parameters help quantify the

inhomogeneity of the network at a microscopic level, both in terms of the behavior at a single hotspot and in terms how the spatial distribution of hotspots correlates to that of NW-NW junctions. We see that hotspots exist at a subset of the NW-NW junctions within the network; for the specific network characterized in this study, hotspots occur at only  $\sim 15 - 20\%$  of the NW-NW junctions. Hotspots are mostly formed at the weak (i.e. highly resistive) links of the most current conducting pathways as illustrated in section 5.10. This indicates that the remainder of the junctions are either disconnected from the current pathways or exhibit very high or very low resistance (all resulting in negligible power generation). In a prior study [30], we have quantified clustering of hotspots in NW networks and hybrid graphene/NW networks. The clustering indicates the presence of subnetworks which are disconnected from the main conduction pathways but which contain interconnected internal pathways. Even in cases in which it is not possible to differentiate which of these conditions leads to negligible power at a given junction, TR imaging can provide at least indirect information regarding current pathways, e.g. in terms of the relative number of hotspots along various radial directions within the concentric circular channel or in comparisons between the relative behavior (spatial distribution and temperature rise) between networks employing different materials and fabrication conditions. Therefore, this technique is universally applicable to any NW/CNT network and even to junction free or metallic grid based networks.

## 6. COMPARATIVE STUDIES OF TRANSIENT THERMAL RESPONSES OF HOTSPOTS IN GRAPHENE-SILVER NANOWIRE NETWORK AND SILVER NANOWIRE NETWORK

### 6.1 Overview

In this chapter, we present a comparative study of thermal transients of hotspots in two non-homogenous networks: silver nanowire (NW) network where percolation based transport mechanism prevails and hybrid (graphene-silver NW) network where co-percolation based transport mechanism is predominant.

Among NW networks, silver NWs have been widely studied and various approaches have been utilized to improve the junction topography/configuration, including laser/thermal annealing and fabrication of junction-free networks [35, 58, 60, 93-95]. In many cases, highly resistive NW-NW junctions dominate the sheet resistance [62, 82, 91, 96, 97] and corrosion due to environment is of concern for long-term stability [98-100]. Hybrid approaches involving integration of a 2D layer (e.g. single-layer graphene) with a NW network have been utilized to improve the sheet resistance, particularly in the high transparency regime [1, 18, 19, 61, 101-103]. In hybrid networks, coperculation through the two sub-networks can overcome the transport bottlenecks at NW-NW junctions and graphene can serve as a protective layer for the underlying NW network [104-111]. Roll-to-roll production of NW and hybrid networks has been reported, illustrating the potential for large-scale manufacturing [40, 93, 101, 112-117]. Percolation and coperculation models have been developed to describe the general trends in sheet resistance and transmittance on NW density, including statistical models (e.g. using interconnected resistor networks) of current pathways [19]. However, prior experiments have not yielded details such as distributions of junction resistances and current pathways through the device. Most experimental studies on nanostructured TCE properties have focused on large area steady state exploration of electrical and optical properties or more microscopic studies of single/few junctions within the networks [36]. Approaches which allow more microscopic characterization of the electrical properties within the overall network would provide a more in-depth understanding of conduction processes/pathways through the

various types of networks as well as coupled electro-thermal response including local self-heating, which is expected to have a direct impact on reliability.

In previous chapters, we discussed transient studies using thermoreflectance (TR) imaging techniques, which provide information on self-heating at local hotspots within nano-structured networks with sub-micron spatial and *ns* range temporal resolution [2]. Spatial inhomogeneity and formation of hotspots at NW-NW junctions are some of the distinctive features of network based systems. Since hotspots form at the weakest link of the most conductive current pathways due to Joule heating, it is important to study the hotspots dynamics in NW and hybrid networks in order to understand the different current transport mechanisms. In this chapter, we present a comparative study of thermal transients of hotspots in silver NW and hybrid (graphene-silver NW) networks. In both networks, we find similar thermal time constants in the vicinity of a hotspot with comparable steady state temperature amplitudes. These thermal parameters have similar dependency with distance from a contact indicating the time constant arises due to the self-heating of NW-NW junctions. In a comparison of overall hotspot distributions at comparable bias condition, the hybrid network exhibited fewer hotspots ( $\sim 5x$ ), a lower average hotspot temperature ( $\sim 1.5x$ ) and a larger average power per hotspot ( $\sim 2.6x$ ), all in comparison to the NW network. Finally, we show that hotspots are more clustered in hybrid network, which indicates better connectivity of hybrid network. In this chapter, these observations are explained semi-quantitatively using representative resistor network topologies and estimations of the thermal resistances associated with local heat flow through NW and graphene. All these parameters help to understand qualitatively the underlying current transport mechanism in these two types of network.

The chapter is arranged in the following way. First, we compare/contrast thermal transient behavior of individual hotspots in both type of networks. Next, we analyze and compare temporal evolution of their collective thermal behavior in terms of their number, average temperature change  $\Delta T$ , and spatial distributions in both networks.

## 6.2 Comparative Transient Thermal Characteristics of Individual Hotspots

Fig. 6.1 shows representative TR images captured at different  $\tau_{DS}$ . We see that certain localized areas in both networks have much higher  $\Delta T$  (as high as 100K in silver NW network and 60 K in hybrid network) than surrounding areas and are mostly formed at the NW-NW junctions. These regions are recognized as “hotspots”. Due to the

inhomogeneous nature of the networks, these hotspots are non-uniform both in spatial location and in temperature. For thermal analysis, a  $4\ \mu\text{m} \times 4\ \mu\text{m}$  area ( $\sim 36$  pixels), generally encompassing several NW-NW junctions (microscopic hotspots, with dimensions of  $\sim$  hundreds of nanometers), is selected for each hotspot.

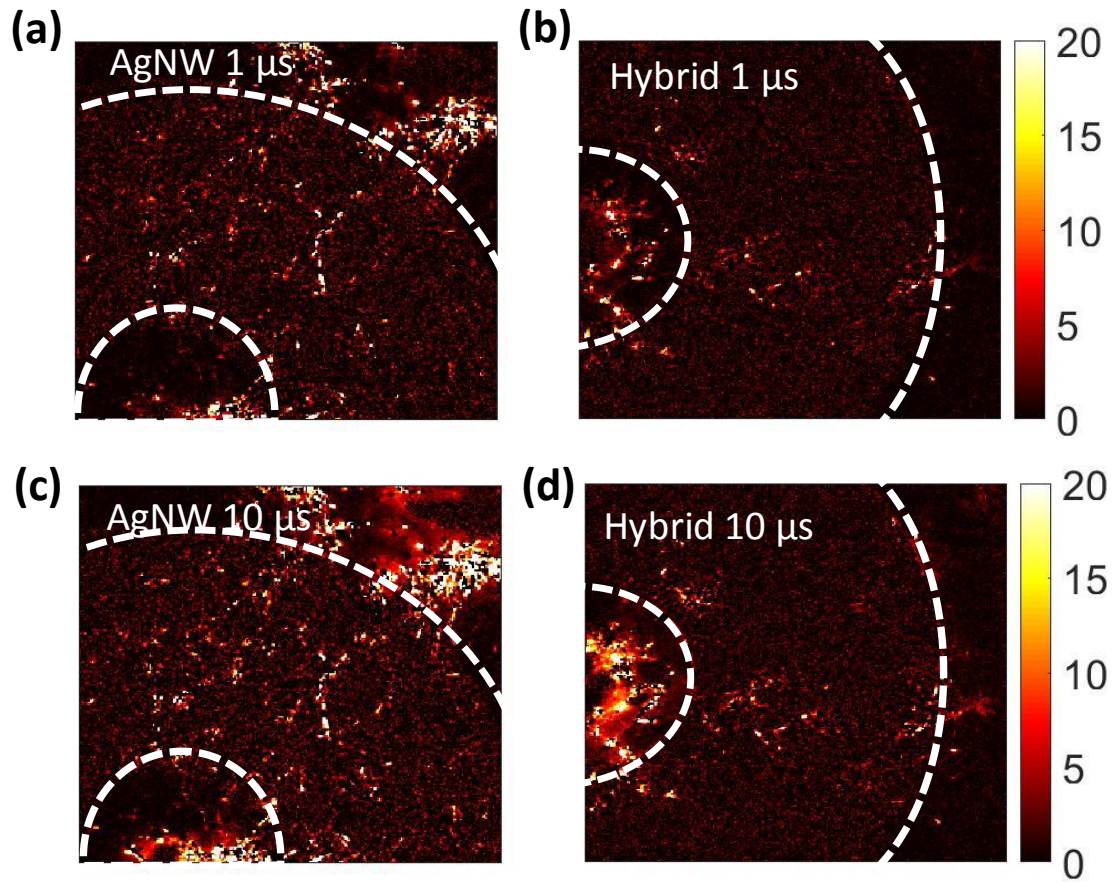


Fig. 6.1: Transient response (i.e. TR images) at different  $\tau_{DS}$  showing formation of hotspots during heating cycle at (a)(b)  $1\ \mu\text{s}$ , and (c)(d)  $10\ \mu\text{s}$  for silver NW and hybrid network respectively. The dotted lines represent the inner and the outer circular electrical contacts respectively.

In order to observe comparative  $\Delta T$  evolution of hotspots with time due to the local self-heating at the NW-NW junctions, we take two representative hotspots, one in the hybrid network and one in the silver NW network, at a comparable distance ( $\sim 60\ \mu\text{m}$ ) from the center of the inner contact. (Note that since NW distributions are random in these two networks, it is challenging to obtain hotspots at comparable distances for a fair

comparison.) Fig. 6.2 shows  $\Delta T$  Vs time profiles during the heating and the cooling cycle. Clearly, for both the hotspots, the transient heating exhibits a single thermal time constant. Similarly, for the cooling cycle, a single thermal time constant is observed for both the hotspots.

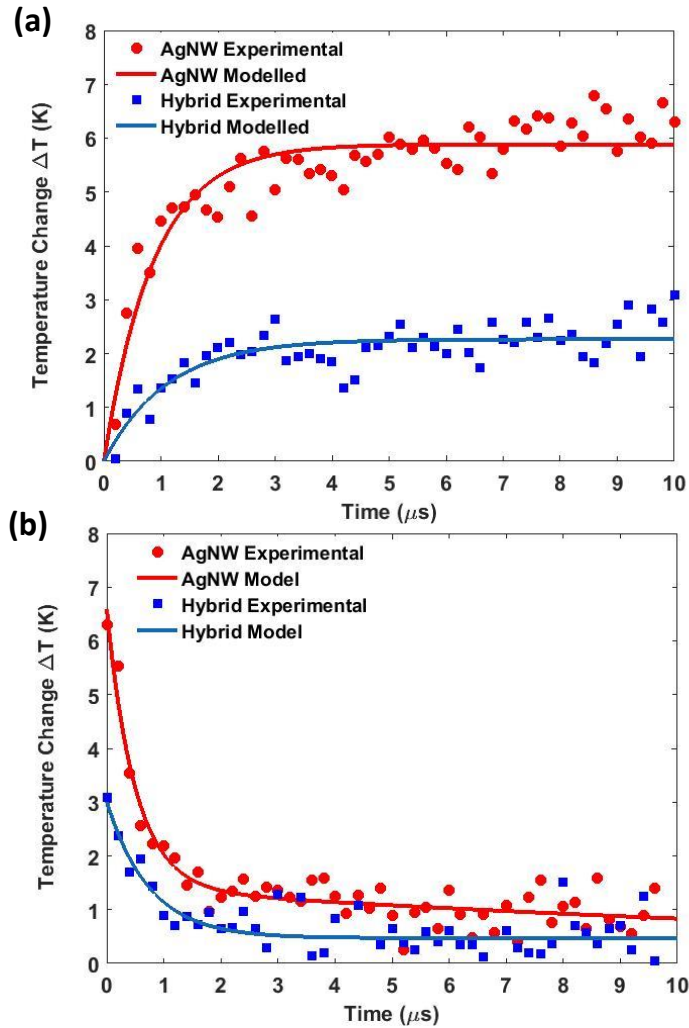


Fig. 6.2: Comparison of  $\Delta T$  vs.  $\tau_D$  profiles of two hotspots at comparable distances in the silver NW and hybrid network during the (a) heating cycle (b) cooling cycle.

To quantify the transient dynamics, we fitted the data from the heating portion of the pulse with  $\Delta T = \frac{A_{H\_Hybrid}}{\tau} (1 - e^{-\frac{t}{\tau_{H\_Hybrid}}})$  for the hotspots in hybrid network and  $\Delta T = \frac{A_{H\_Silver}}{\tau} (1 - e^{-\frac{t}{\tau_{H\_Silver}}})$  for the hotspots in silver NW network where  $\tau_{H\_Hybrid}$ ,  $\tau_{H\_Silver}$  are the thermal time constants, and  $A_{H\_Hybrid}$ ,  $A_{H\_Silver}$  are the corresponding amplitudes of the

hotspots for hybrid and silver NW network respectively during the heating cycle (see red and blue solid line in Fig. 6.2). Similarly, the cooling transient data has been fitted with  $\Delta T = A_{C\_Hybrid} e^{-\frac{t}{\tau_{C\_Hybrid}}}$  and  $\Delta T = A_{C\_Silver} e^{-\frac{t}{\tau_{C\_Silver}}}$ , where  $\tau_{C\_Hybrid}$ ,  $\tau_{C\_Silver}$  and  $A_{C\_Hybrid}$ ,  $A_{C\_Silver}$  are the time constants and amplitudes of hotspots for hybrid and silver NW network during the cooling cycle, respectively. The hotspot in hybrid network shows  $\tau_{H\_Hybrid} \sim 700 \text{ ns}$ ,  $\tau_{C\_Hybrid} \sim 600 \text{ ns}$  and  $A_{H\_Hybrid} \sim 1.8 \text{ K}$ ,  $A_{C\_Hybrid} \sim 2.4 \text{ K}$ . On the other hand, the hotspot in silver NW network shows  $\tau_{H\_Silver} \sim 800 \text{ ns}$ ,  $\tau_{C\_Silver} \sim 800 \text{ ns}$  and  $A_{H\_Silver} \sim 6 \text{ K}$ ,  $A_{C\_Silver} \sim 6 \text{ K}$ . For different hotspots within both types of network, we obtain comparable thermal time constants  $\tau_H < 1 \mu\text{s}$  and  $\tau_C < 1 \mu\text{s}$  during the heating and cooling cycle. In case of these two specific hotspots,  $A_H$  and  $A_C$  values are higher for the hotspot in silver NW network ( $A_{H\_Hybrid} \leq A_{H\_AgNW}$  and  $A_{C\_Hybrid} \leq A_{C\_AgNW}$ ). But, in general, we see that the steady state temperature amplitudes are comparable in both networks (discussed later in Fig. 6.3). Various hotspots within the networks show qualitatively similar behavior with similar time constants, but varying maximum temperature change and weighting of the time constant.

Fig. 6.3 shows the extracted  $\tau_H$ ,  $\tau_C$ ,  $A_H$ , and  $A_C$  values of representative hotspots in the networks at various locations measured from the center of the inner contact  $r$ . The radius of the inner contact is  $40 \mu\text{m}$  and the inner radius of the outer contact is  $140 \mu\text{m}$ . As we mentioned previously, we see that the steady state temperatures are comparable throughout the channel region. Also, we see that  $A_H$  and  $A_C$  of hotspots in both networks shows similar behavior with respect to  $r$ , systematically falling as  $\frac{1}{r^2}$  (similar to how current density scales with  $r$ ) due to the circular structure of the device which we reported in our previous publication. We also find that hotspots in both network show comparable  $\tau_H$ , and  $\tau_C$  values less than  $1 \mu\text{s}$  and remain invariant with distance  $r$ . This observation for hotspots in silver NW network is consistent with our earlier findings for hotspots in hybrid network [2]. Previously, we reported that the thermal time constants of hotspots in hybrid network (formed in response to shorter device heating pulse of  $10 \mu\text{s}$ ) are due to the local self-heating of the NW-NW junctions, depend on the thermal properties in the vicinity of a NW-NW junction, and exhibit no variation with distance. Our findings that hotspots in silver NW network show similar behavior regarding thermal time constants and that steady state temperature amplitudes falls systematically with distance similar to current density, confirm that these parameters origin due to self-heating of NW-NW junctions.

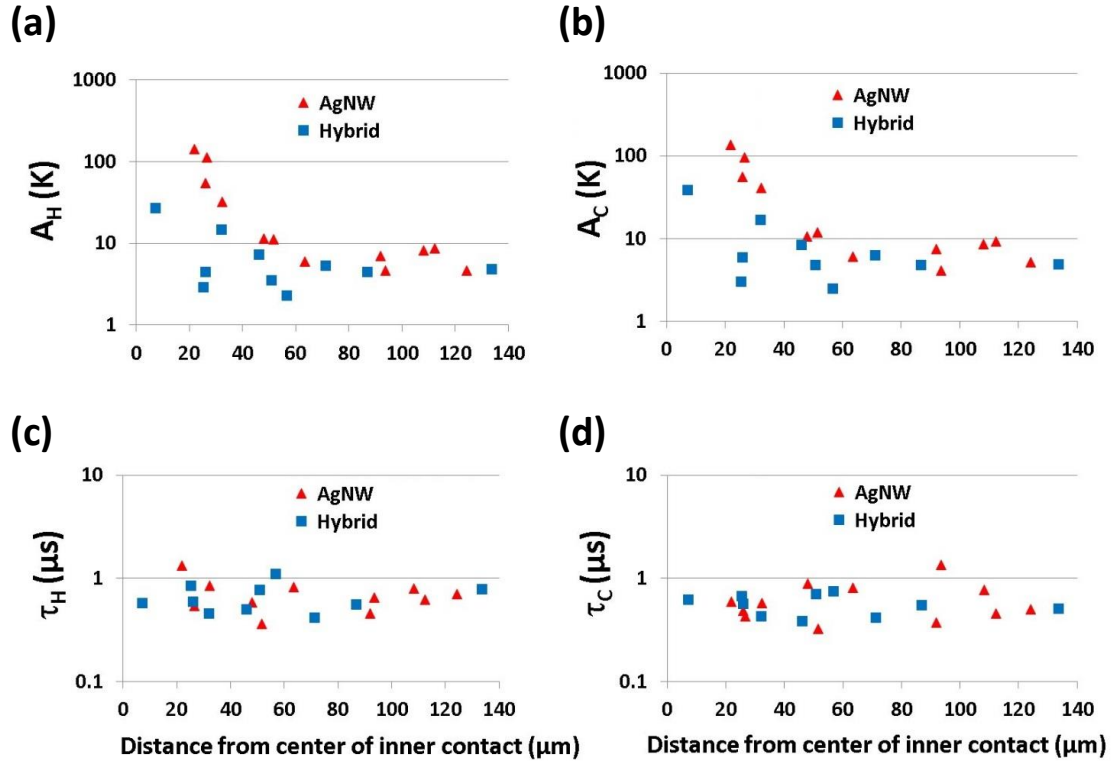


Fig. 6.3: Comparison of (a)  $A_H$  vs distance  $r$  from the center of the inner electrical contact; (b)  $A_C$  vs  $r$ ; (c)  $\tau_H$  vs  $r$ ; (d)  $\tau_C$  vs  $r$  in silver NW and hybrid network.  $r < 40 \mu\text{m}$  and  $r > 140 \mu\text{m}$  represent the inner and the outer electrical contact regions respectively.

To summarize the thermal transient behaviors of individual hotspots in hybrid and silver NW network: we find that hotspots in both network show similar thermal behavior with comparable thermal time constants less than  $1 \mu\text{s}$  which remain invariant with distance. The steady state temperature amplitudes of the hotspots are also comparable in both networks and vary systematically in a similar way with distance within the networks.

## 6.3 Collective Thermal Characteristics of Hotspots

### 6.3.1 Comparison of Evolution of Number of Hotspots

One of the observations from the TR images shown in Fig. 6.1 is that silver NW network has more hotspots compared to hybrid network. This indicates that by incorporating 2D graphene with 1D NW network, a substantial number of electric and thermal bottlenecks can be reduced. We quantify and compare the change in number of

hotspots with time in these two networks. For this analysis, we consider the quarter of the network region that represents the shortest distance in between the two electrical probes and where most of the hotspots are formed (electrical contacts made with Ti/Pd/Au layers are thin, the corresponding resistance cannot be ignored). Both the networks have similar number of total pixels in the areas considered. In order to determine the total number of hotspots within the entire  $100\ \mu\text{m}$  channel area, we used a customized MATLAB script to construct a binary image from the corresponding TR image at  $\tau_D$ s considering only the pixels that have  $\Delta T$  greater than or equal to a threshold temperature change (5K in this case). Joule heating due to the applied electrical power occurs mostly at these hottest hotspots. At  $\tau_D = 1\ \mu\text{s}$ , this threshold temperature represents  $\sim 2\%$  and  $\sim 10\%$  of the hottest pixels within the hybrid and silver NW network respectively. The MATLAB script is used to obtain the total number of hotspots from the total number of the islands of connected pixels. Fig. 6.4 shows the binary images at  $\tau_D = 10\ \mu\text{s}$  for both types of network.

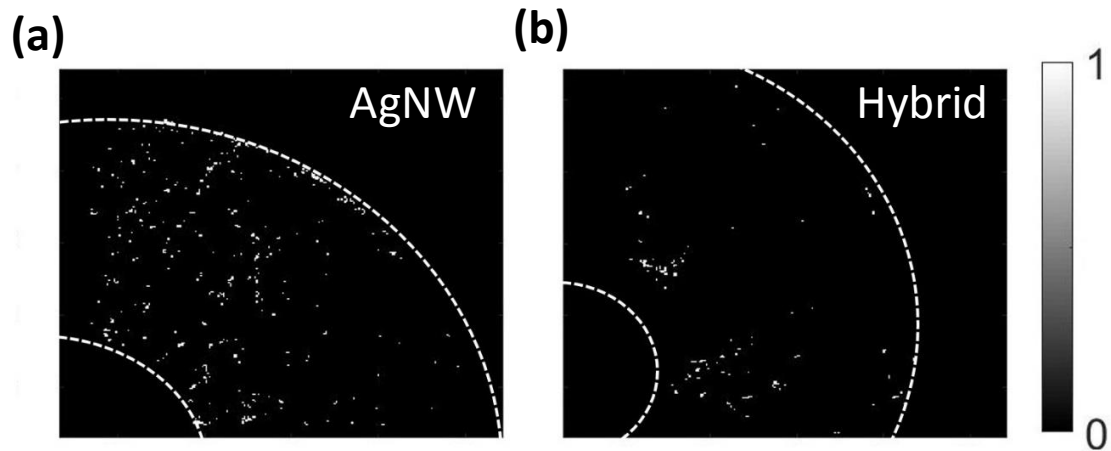


Fig. 6.4: Binary images at  $\tau_D = 10\ \mu\text{s}$  in (a) silver NW network, and (b) hybrid network. Binary images are created from TR images, showing all pixels with  $\Delta T$  greater than or equal to 5K. The binary images are used to calculate the approximate number of hotspots within the network. The dashed lines denote the inner and the outer circular electrical contacts.

Fig. 6.5 shows the evolution of number of hotspots with time in both networks. We find that at the steady state (at after  $1\ \mu\text{s}$ ), silver NW network has 5 times higher the total number of hotspots compared to hybrid network (*i. e.*  $\frac{n_{silver}}{n_{Hybrid}} \cong \frac{250}{50} = 5$ ) during the heating cycle. Here,  $n_{silver}$  ( $n_{Hybrid}$ ) is the total number of hotspots generated within silver

NW (hybrid) network. This ratio remains approximately the same even if the threshold temperature is changed.

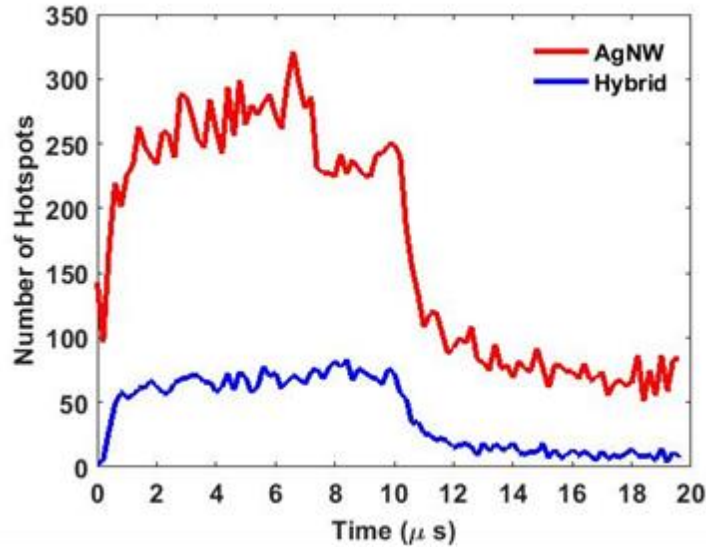


Fig. 6.5: Comparison of number of hotspots vs time  $\tau_D$  in silver NW and hybrid networks.

### 6.3.2 Comparison of Evolution of Average Hotspot Temperature

Fig. 6.6 shows the average  $\Delta T$  of these hotspots with time. At steady state, the hotspots in silver NW network has an average  $\Delta T$  almost 1.6 times higher than the hybrid network i.e.  $\frac{\Delta T_{Avg Silver}}{\Delta T_{Avg Hybrid}} \cong \frac{16}{10} = 1.6$  where,  $\Delta T_{Avg Silver}$  ( $\Delta T_{Avg Hybrid}$ ) is the average hotspot temperature in silver NW (hybrid) network. Higher number of hotspots and higher average  $\Delta T$  of the hotspots in silver NW network (opposite is true for hybrid network) illustrates two important aspects of transport in percolating and coperculating network. In hybrid network, where coperculation is the key transport mechanism, graphene contributes mainly two ways to reduce transport bottlenecks. 1) It provides additional low resistance electrical current pathways to connect portions of NW network which would otherwise be disconnected. 2) It reduces overall NW-NW junction resistance either electrically (by providing alternating route to bypass resistive junctions or conducting current in parallel with NWs) and/or mechanically (by providing mechanical force to fuse the junctions better during the annealing process). We discuss more about the average thermal power at the hotspots later in details.

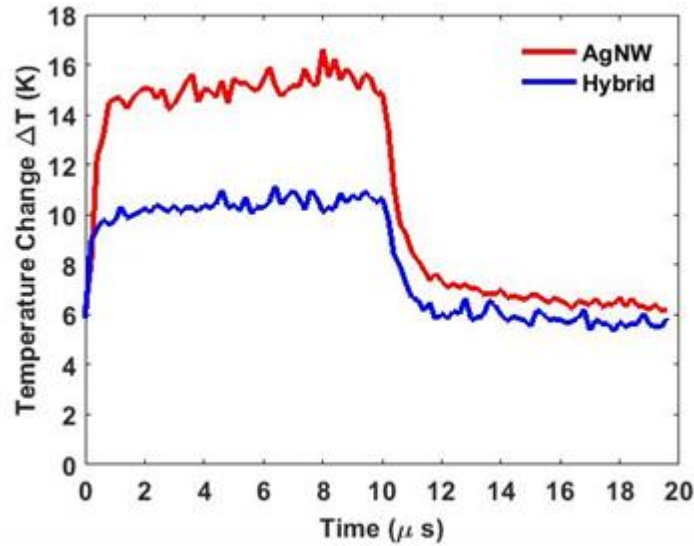


Fig. 6.6: Comparison of average hotspot temperature change ( $\Delta T$ ) vs time  $\tau_D$  in silver NW and hybrid networks.

### 6.3.3 Comparison of Evolution of Spatial Distributions

Another interesting observation from the TR images of Fig. 6.1 is that hotspots within silver NW network seems to be spatially more dispersed compared to coperculating hybrid network. In hybrid network, not only there are less number of hotspots with low average  $\Delta T$  but also these hotspots are more spatially closely packed compared to silver NW network. In an effort to quantify how the hotspots are spatially evolving with time, we take average nearest neighbor (ANN) ratio as a metric of clustering of hotspot. This metric is widely used to compare and quantify observed distributions to a control distribution in various fields in agriculture, biology, urban planning, geography, and regional crime mapping etc.

ANN ratio for network based systems is defined as,

$$ANN\ ratio = \frac{\bar{D}_O}{\bar{D}_E} \quad (6.1)$$

Here,  $\bar{D}_O$  is the observed mean distance between each hotspot and its nearest neighbor hotspot (illustrated in details in the Fig. 6.8), i.e.  $\bar{D}_O = \frac{\sum_{i=1}^n d_i}{n}$  where  $d_i$  is the distance between hotspot  $i$  and its nearest neighbor hotspot,  $n$  is the number of hotspots in the network.  $\bar{D}_E$  is the expected mean distance for the hotspots given a random pattern:

$\bar{D}_E = \frac{1}{2\sqrt{\frac{n}{A}}}$  where  $A$  is the total area where  $n$  features (hotspots in our case) reside. We measure all distances in terms of pixel. Similar area ( $A$ ) with similar total pixel count is considered for both the networks which is a quadrant of the 100  $\mu\text{m}$  channel area in between the electrical probe where most of the hotspots are formed. ANN ratio  $< 1$  indicates that the hotspots exhibits clustering whereas ANN ratio  $> 1$  shows the hotspots are spatially dispersive in nature.

Fig. 6.7 shows schematics of how ANN ratio corresponds to spatial clustering of objects within a specific area [118].

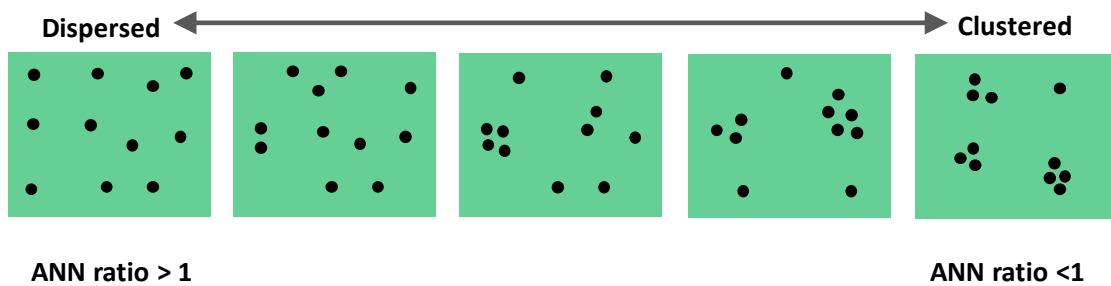


Fig. 6.7: Schematics showing the correlation of ANN ratio with spatial clustering.

In order to quantify ANN ratio for each type of network at a given time instant  $\tau_D$ , first the total number of hotspots  $n$  are determined (the algorithm for determining the number of hotspots is mentioned Chapter 5). Then, for each hotspot  $i$ , its nearest neighbor distance  $d_i$  is determined in pixels [119]. To determine  $d_i$ , a MATLAB program is used to determine the borderlines of each of the hotspots. Then mutual distances (in pixels) between the hotspots are determined using the individual borderlines of the hotspots. For each of the hotspots  $i$ , the lowest of the mutual distances is the corresponding nearest neighbor distance  $d_i$ . Fig. 6.8 shows schematics of this algorithm. For the four hotspots shown, nearest neighbor distances are  $d_1$ ,  $d_1$ ,  $d_2$ , and  $d_3$  at a certain  $\tau_D$ . Therefore,  $\bar{D}_O = \frac{d_1 + d_2 + d_3 + d_3}{4}$  at that  $\tau_D$ .

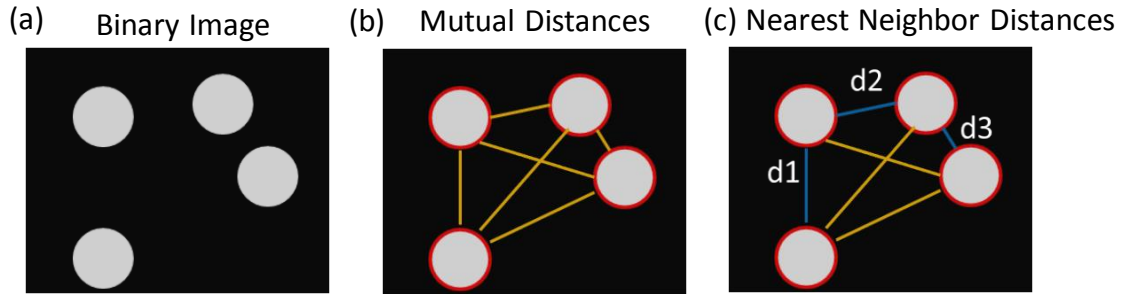


Fig. 6.8: Schematics of (a) binary images to be created from TR images showing different hotspots at a certain time instant  $\tau_D$ ; (b) borderlines of the hotspots are shown in red and mutual distances are shown in yellow lines; (c) Nearest neighbor distances of individual hotspots are shown in blue.

After determining  $\bar{D}_O$  and  $\bar{D}_E$ , ANN ratio at  $\tau_D$  is determined accordingly using Eq. (6.1) mentioned above. Fig. 6.9 shows these parameter values with time. We see a rapid decrease of  $\bar{D}_O$  within 1  $\mu\text{s}$  of the heating cycle for both networks and then it saturates (which is consistent with the observed thermal time constant of 1  $\mu\text{s}$  and also with Fig. 6.2, no new hotspots are formed after this time line). Hybrid network shows comparatively rapid change due to the less number of hotspots formed within the network ( $\bar{D}_O$  changes from 50 to 10 pixel distance) whereas silver NW network  $\bar{D}_O$  changes from 10 to 5. During the cooling cycle,  $\bar{D}_O$  increases, as expected. For silver NW network,  $\bar{D}_O$  value remains steady at the value of 10. For hybrid network, the cooling cycle data is a little noisy due to lower  $\Delta T$  of the network and small number of hotspots. Both the networks show ANN ratio less than 1 during the heating cycle with silver NW network showing a higher ANN ratio of 0.9 and hybrid network a lower value of 0.6. Comparing ANN ratio of hybrid network with that of silver NW network, we have  $\frac{0.6}{0.9} = 0.67$ . This indicates that the distribution of hotspots in hybrid network relative to an expected random distribution appears to be more concentrated than that in silver NW network relative to an expected random distribution (i.e. hotspots in hybrid network are more clustered than in silver NW network). During the cooling cycle, since  $\Delta T$  drops fast within 1 or 2  $\mu\text{s}$ , it is difficult to quantify mutual distances of the hotspots and ANN ratios over time.

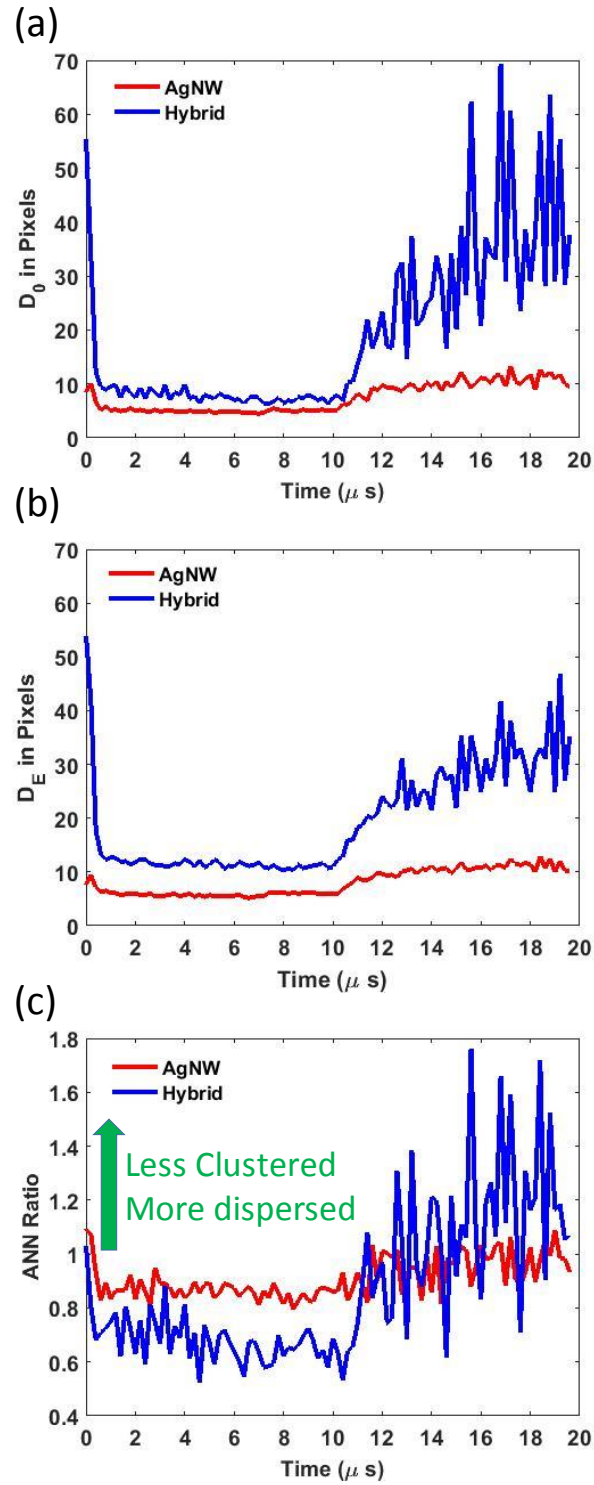


Fig. 6.9: Evolution of (a) average nearest neighbor distance  $\bar{D}_0$ ; (b) expected mean distance given a random pattern  $\bar{D}_E$ ; (c) ANN ratio with time  $\tau_D$ .

### 6.3.4 Comparison of Evolution of Average Network Temperature

Besides hotspots, we also compare the evolution of average network temperature with time taking into account temperature rise of all the NW pixels within the network. A masking algorithm was devised to select only the NW pixels and to eliminate substrate pixels from the CCD images of the networks at different  $\tau_{DS}$ . Even though in 20x measurement, each pixel is  $\sim 670$  nm indicating each pixel includes NWs as well as substrate, the masking algorithm excludes substrate to obtain highest possible accuracy within the limitation of the pixel spatial resolution. For both types of network, pixels with CCD intensity greater than a threshold intensity have been selected for analysis. This threshold intensity is chosen in a way such that the percentage of pixels considered for analysis (representing NW bodies and junctions) matches the area fill factor of NWs ( $\sim 20\%$ ) in the fabricated NW network samples. Then at each  $\tau_D$ ,  $\Delta T$  of the selected NW pixels are averaged in order to obtain the average change of temperature of the network with time. We find that the average temperature of the silver NW network is  $\sim 2.5$  times higher than that of the hybrid network as shown in Fig. 6.10.

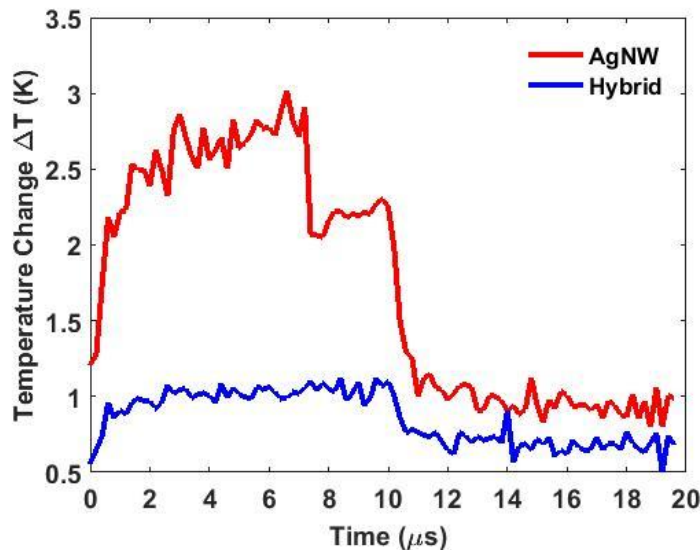
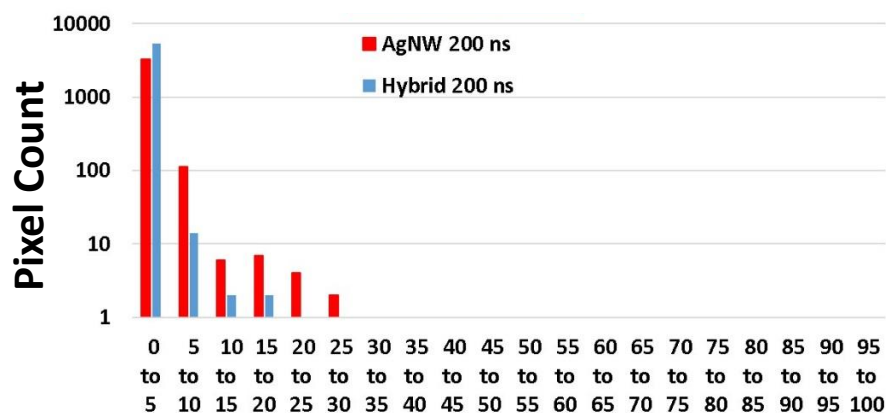


Fig. 6.10: Comparison of average  $\Delta T$  of the NWs within the channel region of silver NW network and hybrid network.

Histograms of  $\Delta T$  of the selected NW pixels at 200 ns and 1  $\mu s$  (Fig. 6.11) also show that silver NW network has hotter pixels compared to hybrid network.

(a)



(b)

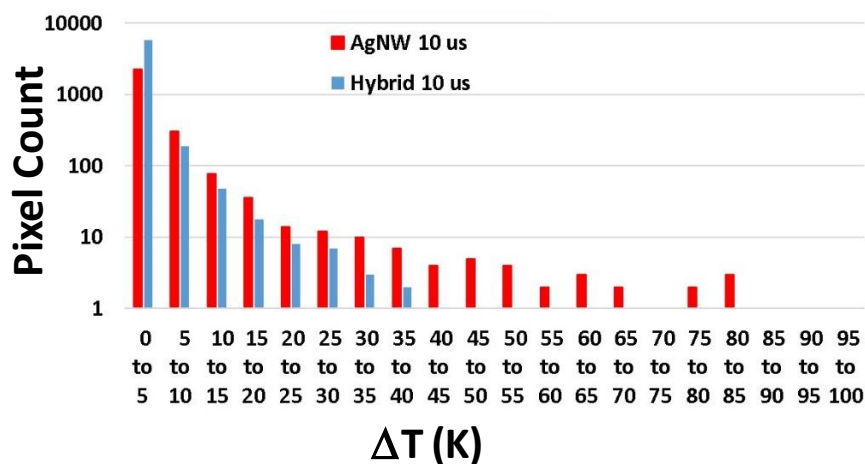


Fig. 6.11: Comparison of temperature histograms of NW pixels within silver NW network and hybrid network at (a)  $\tau_D = 200$  ns, and (b)  $\tau_D = 10$   $\mu$ s.

#### 6.4 Comparison of Microscopic versus Macroscopic Behavior

It is informative to compare the observed microscopic behavior, e.g. individual and collective characteristics of hotspots, with macroscopic parameters, e.g. the terminal characteristics including total current and power. Such comparisons can provide insights regarding the relative contributions of electrical versus thermal properties to the relative differences between the two types of networks. Table 6.1 summarizes few macroscopic properties of the silver NW network and hybrid network. From circular transfer length

measurements (TLM) employing different network channel lengths (10  $\mu\text{m}$ , 20  $\mu\text{m}$ , 50  $\mu\text{m}$ , and 100  $\mu\text{m}$ ), we obtain the sheet resistance and contact resistance of the networks. We find that the sheet resistance of the silver NW network is  $\sim 2.5$  times higher than that of the hybrid network. We also measure the total resistances of two 100  $\mu\text{m}$  devices, one from each type of network, on which we perform the TR measurements. We use 2-point probe technique to measure the total resistances (i.e. channel resistance + contact resistance). We determine the channel resistances by deducting the respective contact resistances from the total measured resistances. Comparable currents of 46.4  $\text{mA}$  and 52  $\text{mA}$  flow through the silver NW and hybrid network respectively. The overall electrical power dissipated within the channel region of each network can be determined from the current and channel resistance. This yields  $P_{\text{Silver}} = (46.4\text{mA})^2 \times 31.6 \Omega = 68 \text{ mW}$  for the silver NW network and  $P_{\text{Hybrid}} = (52\text{mA})^2 \times 13.1 \Omega = 35.3 \text{ mW}$  for the hybrid network where  $P_{\text{Silver}}$  and  $P_{\text{Hybrid}}$  are the total electrical power to the channel in the silver NW network and hybrid network respectively. Therefore, the channel power in the silver NW network is  $\sim 2$  times higher compared to the hybrid network.

Table 6.1: Macroscopic Properties of Silver NW and Hybrid Network

Properties	Silver NW Network	Hybrid Network
Sheet Resistance (TLM measurements)	30.9 $\Omega/\text{sqr}$	12.6 $\Omega/\text{sqr}$
Contact Resistance (TLM measurements)	14 $\Omega$	19.2 $\Omega$
Total Resistance (Measured)	45.6 $\Omega$	32.3 $\Omega$
Channel Resistance( $R_{\text{Ch}}$ )	31.6 $\Omega$	13.1 $\Omega$
Current( $I_{\text{Ch}}$ )	46.4 $\text{mA}$	52 $\text{mA}$
Power in Channel( $I_{\text{Ch}}^2 R_{\text{Ch}}$ ) $P_{\text{Silver}}/P_{\text{Hybrid}}$	$46.4^2 \times 31.6 = 68 \text{ mW}$	$52^2 \times 13.1 = 35.3 \text{ mW}$

Microscopically, we observe from Fig. 6.5 that at steady state,  $\frac{n_{\text{Silver}}}{n_{\text{Hybrid}}} \cong 5$ . We also observe from Fig. 6.6 that at steady state,  $\frac{\Delta T_{\text{Avg Silver}}}{\Delta T_{\text{Avg Hybrid}}} \cong 1.6$ . Qualitatively similar relationships regarding microscopic hotspot temperature are also observed in comparisons of individual hotspots at comparable radii (Fig. 6.3). Since hotspots are the bottlenecks of the network, it is expected that most of the applied electrical power will be dissipated at those hotspots. Therefore, the average thermal power generated at each of the hotspots, denoted as  $P_{\text{Avg Silver}}$  ( $P_{\text{Avg Hybrid}}$ ), can be calculated:

$$P_{\text{Avg Silver}} = \frac{P_{\text{Silver}}}{n_{\text{Silver}}} \cong 0.27 \text{ mW}$$

$$P_{Avg Hybrid} = \frac{P_{Hybrid}}{n_{Hybrid}} \cong 0.71 \text{ mW}$$

$$\therefore \frac{P_{Avg Silver}}{P_{Avg Hybrid}} \cong \frac{1}{2.6}$$

Although  $P_{Hybrid}$  is  $\sim 2$  times smaller than  $P_{Silver}$ , the significant decrease in  $n_{Hybrid}$  yields a  $P_{Avg Hybrid}$  which is  $\sim 2.6$  times higher than  $P_{Avg Silver}$ . Table 6.2 summarizes the microscopic observations from TR measurements along with the average power generated at each hotspot in both types of network. Next, we will discuss how these effects can be explained semi-quantitatively by considering differences between NW and hybrid networks in both resistive pathways and local heat spreading.

Table 6.2: Microscopic Observations and Average Power at Hotspots

Properties	Silver NW Network	Hybrid Network
Number of hotspots at steady state ( $n_{Silver}/n_{Hybrid}$ )	250	50
Average hotspot temperature $\Delta T_{Avg Silver}/\Delta T_{Avg Hybrid}$ (from experiment)	16 K	10 K
Average power at hotspots ( $P_{Avg Silver}/P_{Avg Hybrid}$ )	0.27 mW per hotspot	0.71 mW per hotspot

#### 6.4.1 Resistive Current Pathways

A more physical understanding of the changes in current pathways which lead to the observed changes in number and average power of hotspots can be developed by considering interconnected resistor networks representing the two network types. Broadly, hotspots are expected at relatively resistive links in otherwise conductive pathways. In hybrid networks, the resistance of NW-NW junctions can be reduced by local pathways through the graphene or by more intimate NW-NW contact due to mechanical force applied by the graphene. In PSPICE circuit simulations, we considered two scenarios representing changes between hybrid and NW networks. 1) Reduction of NW-NW resistances within existing current pathways. 2) Additional conductive pathways which connect portions of the network which were weakly connected in the NW network. Considering cases in which the overall resistance changes modestly, the simulated networks show increased power

dissipation at some weak-links, due to increased current associated with the additional pathways feeding current into these weak-links, and reduced power dissipation at other weak-links, due to either reduced resistance of the link or shunting of current away from the link due to new pathways. We discuss the details of the simulations in the next section. These trends qualitatively explain the experimental observations of increased average power per hotspot and reduced number of hotspots in the hybrid network, respectively.

#### 6.4.1.1 Resistor Network Simulations

In order to explain our observations of reduced number of hotspots but with higher thermal power in hybrid network, we did circuit simulations of resistor networks in PSPICE that emulates the transport mechanism within the silver NW and Hybrid network.

A silver NW network can be represented by a resistor network where each of the resistor component represents NW-NW junction resistance. Fig. 6.12 shows such a resistor network (circuit configuration 1) representing two parallel current conducting pathways through a portion of a silver NW network in between the two electrical contacts. Within each of these two current pathway, 4 locally well-connected portions of the network (with lower effective resistance of  $R$ ) are connected through resistors  $R_1$  ( $R \gg R_1$ ,  $R \sim 25 \Omega$  as reported by [90] for similar NWs and annealing conditions) which are otherwise globally disconnected. Hotspots are formed at these high resistance points of the network. The maximum heating occurs at such weak points of the most current conducting pathways. We assign these high resistance points (i.e. hotspots) as HS 1 through 8.

In case of hybrid network, parallel pathways are connected through additional resistors (representing additional connectivity via graphene). Two scenarios are simulated. 1) One of the conducting pathways has been modified and made more conductive. We transform two of the resistive links (HS1 and HS4) more conductive by adding more resistors in parallel to it (Fig. 6.13, circuit configuration 2). This represents the scenario as graphene makes NW-NW junctions better (i.e. reduce the NW-NW junction resistance) either electrically by conducting more current or mechanically by making the junction morphologically better by exerting mechanical force. 2) New conductive pathways with a separate resistor network have been created through graphene which would otherwise be disconnected (Fig. 6.14, circuit configuration 3). This represents the scenario as graphene helps to create more new conductive pathways. In all cases,  $\sim 50$  mA current flows through the network.

We observe that for both the scenarios considered in case of hybrid network, the remaining resistive links (HS2, HS3) shows higher generated power. Additional current from the adjacent current pathways is flowing through graphene via these links, therefore, generating higher thermal power. Moreover, we also found that the other resistive links (HS 5-8) show lower electrical power (i.e. lower current flows through those links). This indicates lower heating at these links and overall reduced number of hotspots in hybrid network. Fig. 6.15 shows the electrical power obtained from the PSPICE simulations at each of these hotspots for all of these circuit configurations.

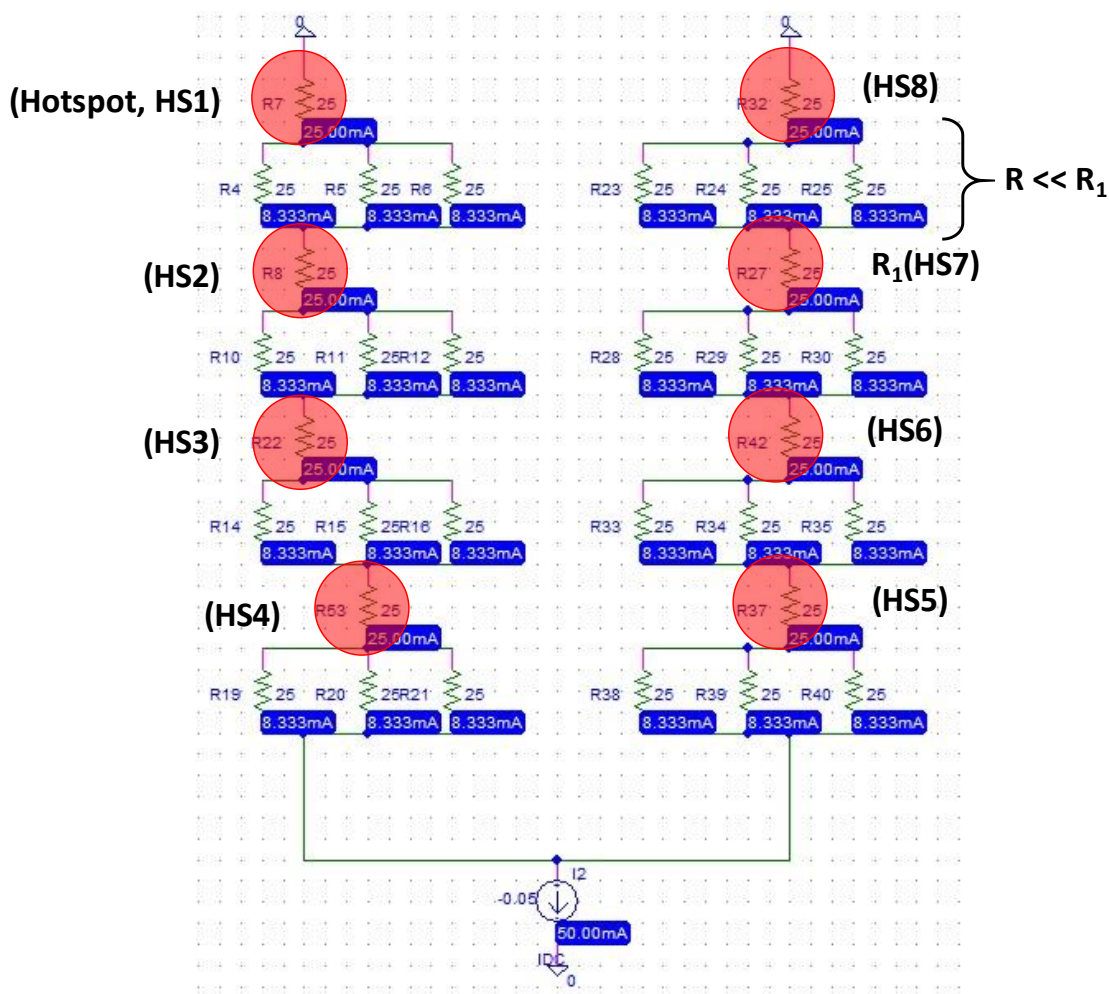


Fig. 6.12: Circuit simulation of a resistor network showing two parallel current conducting pathways in a silver NW network (configuration 1). Eight hotspots (HS 1-8) are represented by the eight resistive links (shown in red circles).



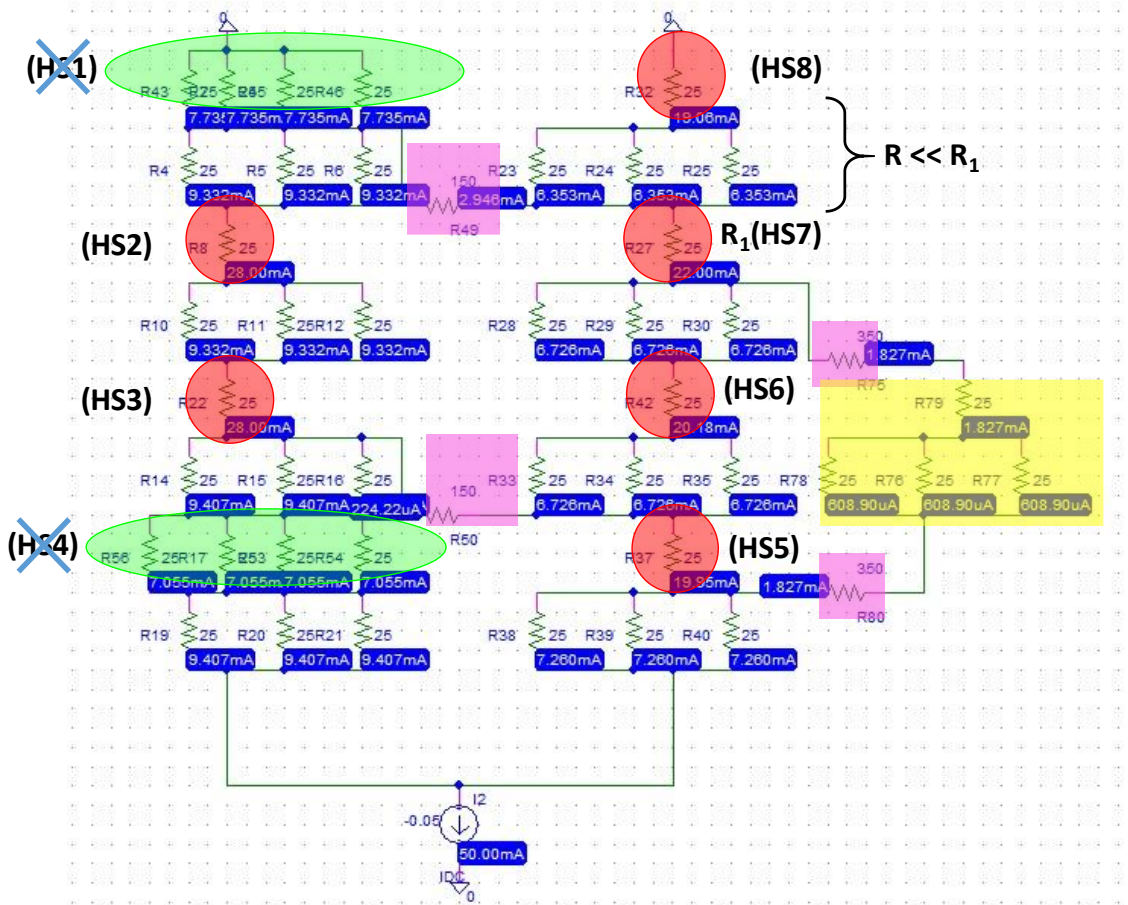


Fig. 6.14: Circuit simulation of the resistor network (configuration 3) with an additional current conducting pathway created through an additional resistor network (shown in yellow).

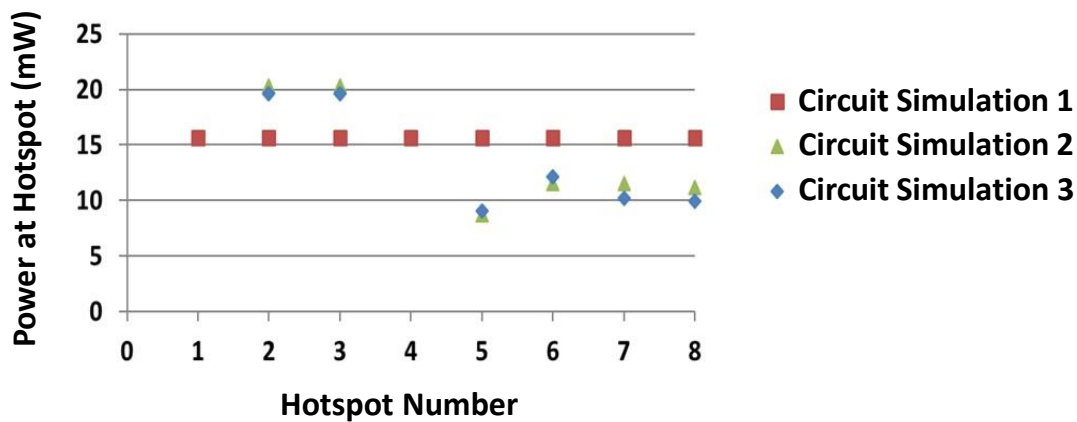


Fig. 6.15: Electrical power at each of the hotspots. Two of the hotspots (HS 2 and 3) show higher power in hybrid network compared to silver NW network whereas other hotspots (HS 5 – 8) show lower values.

### 6.4.2 Local Heat Spreading

In the previous section, we explain our observations of reduced number of hotspots that have higher average power in hybrid network from simulations of resistor networks. In order to explain the other microscopic experimental observation of reduced average hotspot temperature in hybrid network (even with higher average power generated at those hotspots), we look into the details of heat dissipation pathways in the vicinity of NW-NW junctions in both types of network.

We estimated the thermal resistance from a NW-NW junction to heat sink (quartz) via graphene vs. through only NWs. We first determined the typical distance over which graphene is suspended over both sides of the NW ( $\sim 50$  nm) from AFM images and taking length profiles along the diameter of NW in a hybrid network. AFM images of the junctions in both types of network are shown in Fig. 6.16. Length profiles along the NW diameter are shown in Fig. 6.17.

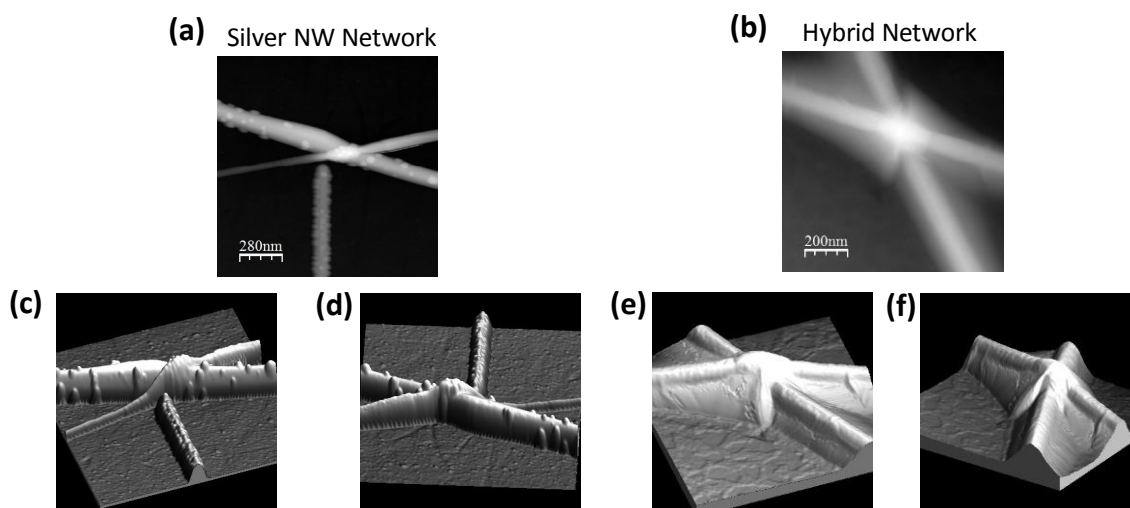


Fig. 6.16: AFM images showing configuration of representative NW-NW junctions in silver NW network and hybrid network. (a)(b) 2-D views; (c) - (f) 3-D views from two different angles of NW-NW junctions in silver NW and hybrid network respectively. In hybrid network, graphene wraps the NW-NW junction.

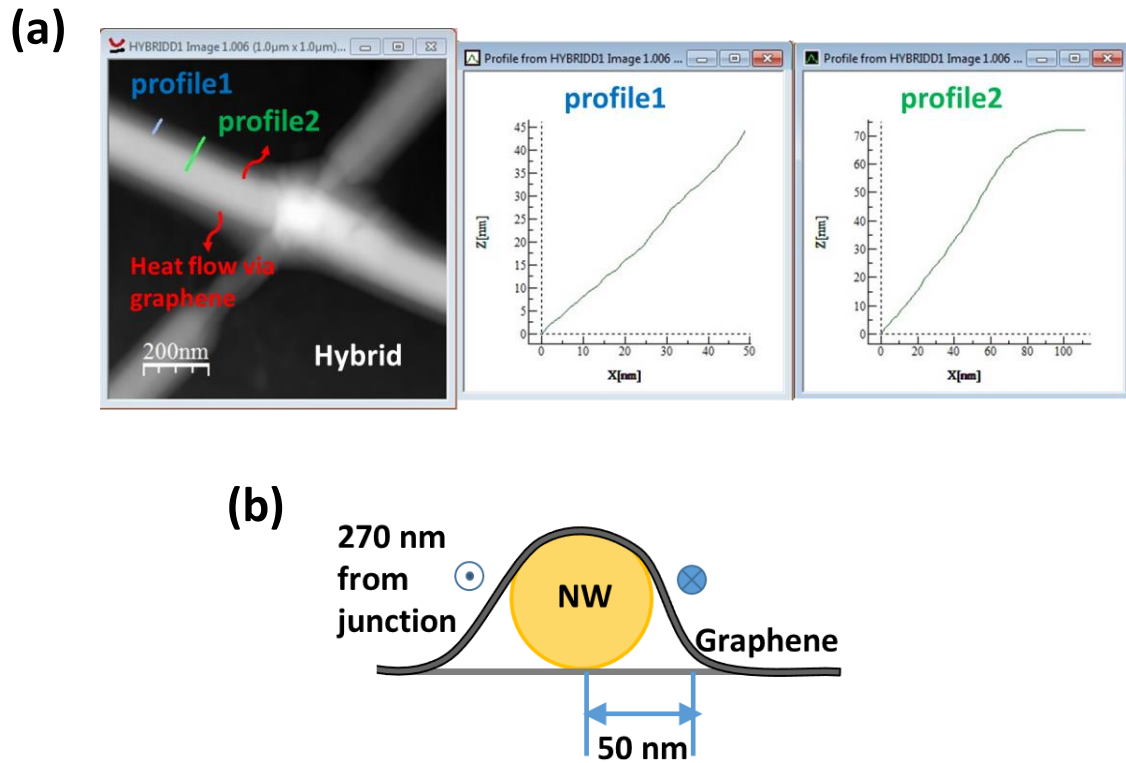


Fig. 6.17: (a) Length profiles from AFM images of a representative NW-NW junction in hybrid network show graphene draping  $\sim 50$  nm on both sides of a NW. (b) Schematics along the cross-section of a NW showing graphene draping on both sides of the NW.

By wrapping the NW-NW junctions, graphene provides additional heat conductive parallel pathways from junction to quartz. Using the draping distance of  $\sim 50$  nm and the distance over which the top NW of a junction makes contact with quartz (270 nm, from our heat model in [120]), we determine the effective thermal resistance of graphene. Thermal resistances of the crossing NWs are determined in a similar way. Our estimation shows that graphene lowers the overall thermal resistance of NW-NW junctions  $\sim 4.5$ x in hybrid network ( $\theta_{Hybrid} = 0.10877 \times 10^5 \frac{K}{W}$  and  $\theta_{SilverNW} = 0.53 \times 10^5 \frac{K}{W}$ ).

Even though graphene is one atomic layer thick, it conducts a considerable amount of heat generated at the NW-NW junction and provides better heat dissipation pathways. Moreover, since graphene has low convection heat transfer coefficient to air, it spreads heat uniformly through the network rather than dissipating heat to air [121]. The lower local thermal resistance in the hybrid network explains how the  $\Delta T_{Avg Hybrid}$  can be lower than  $\Delta T_{Avg Silver}$  even though  $P_{Avg Hybrid}$  is higher than  $P_{Avg Silver}$ . Table 6.3

summarizes the estimated thermal resistances and temperatures of the junctions in silver NW and hybrid network. We find that the ratio of estimated hotspot temperatures (from junction thermal resistances) in these two types of network is similar to the ratio of experimentally observed average hotspot temperature.

$$\Delta T_{Est\ Silver} = P_{Avg\ Silver} \theta_{Silver} = 13.2\ K$$

$$\Delta T_{Est\ Hybrid} = P_{Avg\ Hybrid} \theta_{Hybrid} = 7.7\ K$$

$$\therefore \frac{\Delta T_{Est\ Silver}}{\Delta T_{Est\ Hybrid}} \cong 1.7 \cong \frac{\Delta T_{Avg\ Silver}}{\Delta T_{Avg\ Hybrid}}$$

Table 6.3: Estimated Thermal Resistances and Temperatures of Junctions

Properties	Silver NW Network	Hybrid Network
Estimated thermal resistance of junction ( $\theta_{TH}$ )	$0.4878 \times 10^5\ K/W$	$0.10877 \times 10^5\ K/W$
Average power at hotspots ( $P_{Avg}$ , i.e. $P_{Avg\ Silver}/P_{Avg\ Hybrid}$ )	0.27 mW per hotspot	0.71 mW per hotspot
Estimated average temperature of junction ( $\Delta T_{Est} = P_{Avg} \theta_{TH}$ )	13.2 K	7.7 K
Average hotspot temperature $\Delta T_{Avg\ Silver}/$ $\Delta T_{Avg\ Hybrid}$ (from experiment)	16 K	10 K

## 6.5 Conclusion

In summary, we have done a comparative study of transient thermal responses of hotspots in silver NW and hybrid network. Through TR thermal images, we find out the vulnerable links of the networks where hotspots are formed. We found that hotspots in both networks show similar thermal time constants of less than 1  $\mu s$ . The steady state temperatures of these hotspots show similar distance dependent behavior at different spatial locations of the networks. We determine that silver NW network generates  $\sim 5x$  higher number of hotspots with  $\sim 1.6x$  higher average hotspot temperature. This infers that on an average  $\sim 2.6x$  higher thermal power is generated at each of the hotspots in hybrid network. Simple resistor network circuit simulations verify these experimental observations. Monolayer graphene, in spite of atomically thin, transport a significant amount of

generated power from the NW-NW junction to substrate at this nanoscale. Our thermal resistance model shows that wrapping a silver NW network with graphene reduces the thermal resistance of a NW–NW junction  $\sim 4.5x$ . This becomes evident in the fact that despite generating higher thermal power, the hotspots in hybrid network exhibit  $\sim 1.6x$  lower average temperature rise. Moreover, since graphene drapes over the NWs in hybrid network, significant amount of strain is induced during the annealing process that reduce the overall electrical resistance of the NW-NW junctions. Therefore, we can infer that higher generated power ( $I^2R$ ,  $R$  is junction resistance) at hotspots in hybrid network renders to higher amount of current flowing through these hotspots. We find that hotspots in hybrid network have lower thermal resistance and higher average power; yet we obtain similar thermal time constants for both types of network which is probably due to the higher specific heat capacity of graphene (748 J/KgK [64]) compared to silver NWs (232 J/KgK [35]). Finally, even though TR images cannot capture heating either in NW bodies or in graphene (silver NW bodies, as metallic, does not heat up significantly due to its high electrical and thermal conductivity; on the other hand, graphene is transparent), this technique traces the links where heating is the maximum. By tracking the temperature of these resistive links, it is possible to semi-qualitatively know about current conducting pathways within the networks. Collectively, this electro-thermal study illustrates different current conduction mechanisms in silver NW (percolation) and hybrid (coperculation) network. It also emphasizes the significant role graphene plays in lowering electrical and thermal resistance. This study shows that 1D-2D layered hybrid materials are comparatively more reliable in terms of better thermal conductance and uniform heat spreader with less hotspots making hybrid nanostructured network a superior choice of material to be used in future technologies for novel applications.

## 7. TIME DEPENDENT TEMPERATURE DISTRIBUTIONS IN SILVER NANOWIRE NETWORK CONDUCTORS

### 7.1 Overview

Nano-structured network based systems have become a unique testbed to explore interesting anomalous percolation based transport phenomena. Unlike conventional uniform thin film conductors, intrinsic inhomogeneity is the key feature of such systems. Fundamental inhomogeneity leads to non-uniform current conducting pathways as well as spatially distributed hotspots at the highly resistive nanowire (NW)-NW junctions along a current pathway. These systems show complex non-linear behavior including super-Joule heating of the hotspots [24], recurring turning on/off of certain portions of the network etc. On the other hand, despite these, certain characteristics of such non-homogenous systems can be simply expressed. Recently our group has reported a single thermal time constant of less than 1  $\mu\text{s}$  related to the hotspots in the self-heating time regime (0-10  $\mu\text{s}$ ). We also reported that at steady state, self-heating of such systems due to different applied current bias, can be described by a simple Weibull distribution [30].

In this chapter, we study transient evolution of temperature distributions in silver NW random network. We find that temperature distributions at different time instants at a constant current bias can be described by Weibull distributions. However, the characteristics of the shape parameters with time are opposite in the two different time regime considered. Over 0 – 10  $\mu\text{s}$ , when the temperature rise is mainly due to the local self-heating of the NW-NW junctions, the value of the shape parameters decrease with time until it reaches a steady state value of  $\sim 1$  after 2  $\mu\text{s}$ . Within the time interval of 10 - 450  $\mu\text{s}$ , when heat from nearby electrical contacts start to spread through the network and substrate, we find that the temperature distributions follow Weibull distributions but the shape parameters keep increasing with time. Self-heating simulation of silver thin film on quartz shows that temperature distributions do not follow Weibull distributions. On the other hand, heat diffusion simulation shows that temperature distributions do follow Weibull distributions with shape parameter increasing with time. This study reveals that temperature distributions of network based distributed conductors follow Weibull distributions in contrast with thin film uniform conductors. Nevertheless, the behavior of

shape parameter with time demonstrates whether local self-heating or heat diffusion is predominant within the network.

This chapter is arranged in the following way. First, we discuss the temporal evolution of temperature distributions in the time regime of 0 - 10  $\mu\text{s}$  over which faster local self-heating process mainly at the NW-NW junctions is predominant. Next, we discuss the same for longer 0 – 450  $\mu\text{s}$  time domain as heat (due to resistive heating of the electrical contacts) starts to spread slowly through the network/substrate region from the contacts. Next, we discuss self-heating and heat diffusion simulation results considering a silver thin film on quartz.

## 7.2 Temporal Evolution of Temperature Distributions in Self-Heating Regime of 0-10 $\mu\text{s}$

To obtain temperature distributions of silver NW network, we devised a masking algorithm in MATLAB to select only NW pixels rather than the quartz substrate. A high-resolution TR technique with spatial resolution  $\sim 200 - 400$  nm enables to do so. At each time instant  $\tau_D$ , we construct a binary mask from the grayscale CCD image where pixels with CCD intensity greater than a threshold intensity (generally grayscale value  $\sim 375500$ ) have been selected for analysis. Since NW pixels are comparatively more reflective than underneath quartz substrate, this algorithm helps to select only the NW pixels and to eliminate substrate pixels. Fig. 7.1 shows such a binary mask at  $\tau_D = 1 \mu\text{s}$ . This threshold intensity is chosen in a way such that the percentage of pixels considered for analysis (representing NW bodies and junctions) matches the area fill factor of NWs ( $\sim 20\%$ ) in the fabricated NW network samples.  $\Delta T$  of only these NW pixels are considered for analysis.

For each  $\tau_D$ , the probability distribution function  $f(\Delta T, \tau_D)$  is obtained by plotting the temperature histogram of the distribution with bin size of  $\sim 0.5\text{K}$ . Fig. 7.2(a)-(c) show representative distributions at different  $\tau_D$ s ( $\tau_D = 200$  ns, 400 ns, and 800 ns) in the self-heating time regime of 0 – 10  $\mu\text{s}$  along with corresponding Weibull distributions.

In order to figure out if the temperature distributions corresponds to any known distribution, we plotted  $\ln(-\ln(1 - F))$  vs.  $\ln(\Delta T)$  in a double-log plot. Here,  $F(\Delta T, \tau_D) = \int_0^{\Delta T} f(\Delta y, \tau_D) dy$  is the cumulative probability distribution function. In Fig. 7.2(e), the double-log plots at different  $\tau_D$ s are shown. Each of these plots represents a straight line, which is the signature of a Weibull distribution. Therefore, the experimental  $\Delta T$  distributions at different time instants  $\tau_D$ s can be described by a two-parameter Weibull distribution,

$$f(\Delta T, \tau_D; \alpha, \beta) = \frac{\beta(\tau_D)}{\alpha(\tau_D)} \left(\frac{\Delta T}{\alpha(\tau_D)}\right)^{\beta(\tau_D)-1} \exp\left[-\left(\frac{\Delta T}{\alpha(\tau_D)}\right)^{\beta(\tau_D)}\right] \quad (7.1)$$

Here,  $\alpha$  and  $\beta$  are the time dependent scale and shape parameters respectively.

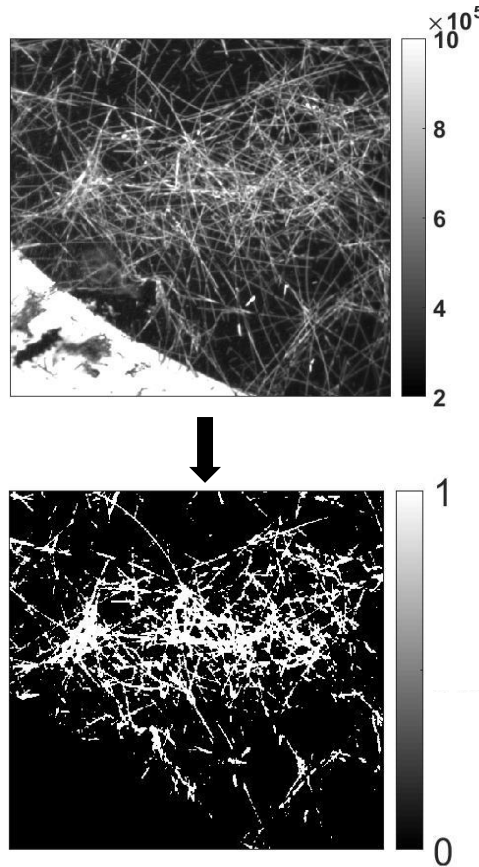


Fig. 7.1: Binary mask obtained from grayscale CCD image. This mask was used to select pixels corresponding to NW locations, and to eliminate pixels corresponding to areas without NWs.

While a double-log plot determines whether the experimental data follows Weibull distributions, it is also important to check the fit at high temperature regime where  $\Delta T \gg \alpha$  and  $\beta$  approaches 1. In this high temperature regime, from Eq. (7.1), we find,  $\ln(f) \rightarrow -\left(\frac{\Delta T}{\alpha(\tau_D)}\right)^{\beta(\tau_D)}$  i.e. logarithm of pdf decreases almost linearly depending on how close the value of  $\beta$  is to 1. Fig. 7.2(d) shows  $\ln(f)$  vs.  $\Delta T$  plots at several representative

$\tau_D$  s. Each of the plots show that Weibull distributions correctly capture the high temperature tails of the distributions.

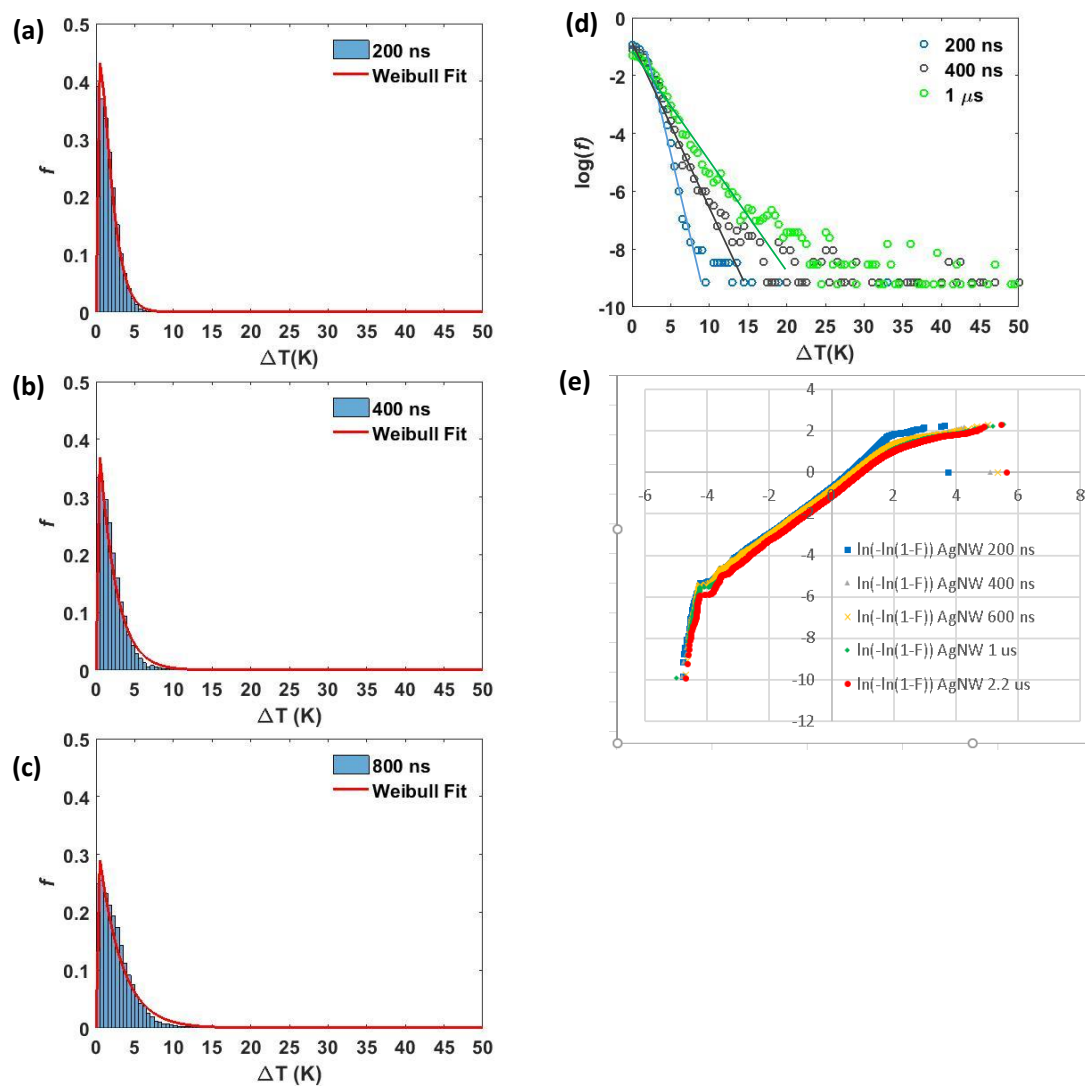


Fig. 7.2: Probability density function  $f$  vs.  $\Delta T$  at various time instants over local self-heating time regime at (a) 200 ns, (b) 400 ns, and (c) 800 ns. (d)  $\log(f)$  vs.  $\Delta T$  at various time instants to take a closer look at the tail of the temperature distributions. (e)  $\log(-\log(1-F))$  vs.  $\log(\Delta T)$  at various time instants showing straight lines (signature of Weibull distributions).

Next, we plot the derived shape parameter  $\beta$  of the distributions with time  $\tau_D$  (i.e. slopes of the straight lines shown in Fig. 7.2(e)). As shown in Fig. 7.3(a), we find that  $\beta$  decreases with  $\tau_D$  until it reaches a steady state  $\sim 2 \mu s$ . The value of  $\beta$  changes from  $\sim 1.20$  to  $\sim 1.08$  within time interval of  $\sim 2 \mu s$ . The decrease of  $\beta$  with  $\tau_D$  reflects that in the self-heating time domain of  $0 - 10 \mu s$ ,  $\Delta T$  of the NW-NW junctions increase but  $\Delta T$  of the NW bodies do not increase in the same proportion, therefore, making the standard deviation (i.e. the spread of data of the temperature distributions) higher with time. This decrease of  $\beta$  with  $\tau_D$  may be an intrinsic characteristics of network based non-homogenous conductors when temperature rise is due to the local self-heating of the NW-NW junctions. This behavior is in contrast with the characteristics we observe in the longer time domain  $0 - 450 \mu s$  which we discuss in the next section.

Within this self-heating time interval, we find that the scale parameter  $\alpha$  increases with time and eventually reaches the steady state as shown in Fig. 7.3(b). The relationship of  $\alpha$  with time delay  $\tau_D$  can be described as,  $\alpha(\tau_D) = A (1 - \exp^{-\frac{\tau_D}{\tau}})$  where the time constant,  $\tau < 1 \mu s$ . This is consistent with individual heating and cooling thermal time constants of the microscopic hotspots formed at the NW-NW junctions that we previously reported[2].

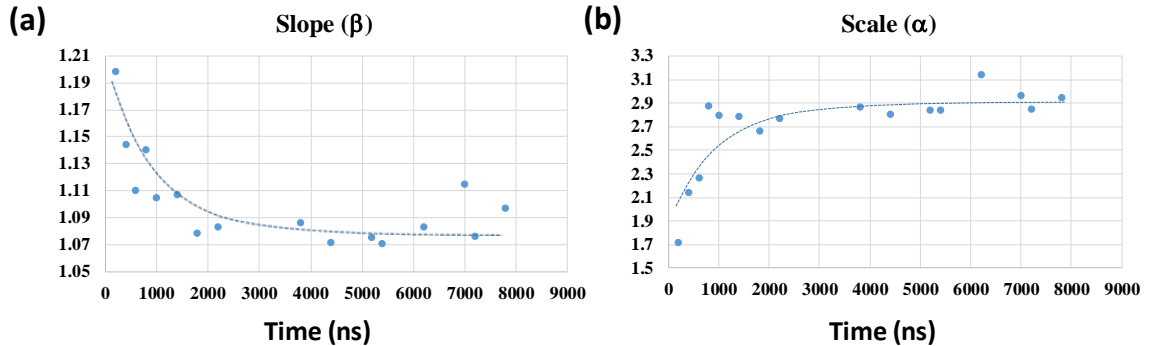


Fig. 7.3: Over the local self-heating time regime, evolution of (a) shape parameter (b) scale parameter with time.

### 7.3 Temporal Evolution of Temperature Distributions in Heat Diffusion Regime of 0- 450 $\mu s$

Previously in [2], we showed that during the longer time domain  $\tau_D = 0 - 450 \mu s$ , temperature rise is mainly due to heat diffusion from the electrical contacts through the

network and substrate. Using similar procedures as mentioned in the previous section for the local self-heating regime of  $0 - 10 \mu\text{s}$ , we obtain temperature distributions from binary mask and derive probability density function  $f(\Delta T, \tau_D)$  and cumulative density function  $F(\Delta T, \tau_D)$  within time interval of  $0 - 450 \mu\text{s}$ . We find that the temperature distributions at different  $\tau_D$ s in this longer time domain can also be described by Weibull distributions (Eq. (7.1)). In Fig. 7.4(a)-(d), the probability distribution functions  $f(\Delta T, \tau_D)$  at different  $\tau_D$ s ( $\tau_D = 20, 50, 160, 400 \mu\text{s}$ ) are shown which are obtained from the histograms of the temperature distributions. Also shown in Fig. 7.4(f), the double-log plots of the experimental data. Each of the plots are straight lines identifying Weibull distributions as the best fit to the experimental data. High temperature tails of the distributions also fit well with Weibull distribution (Fig. 7.4(e)) where  $\ln(f)$  clearly shows almost linear drop with  $\Delta T$ .

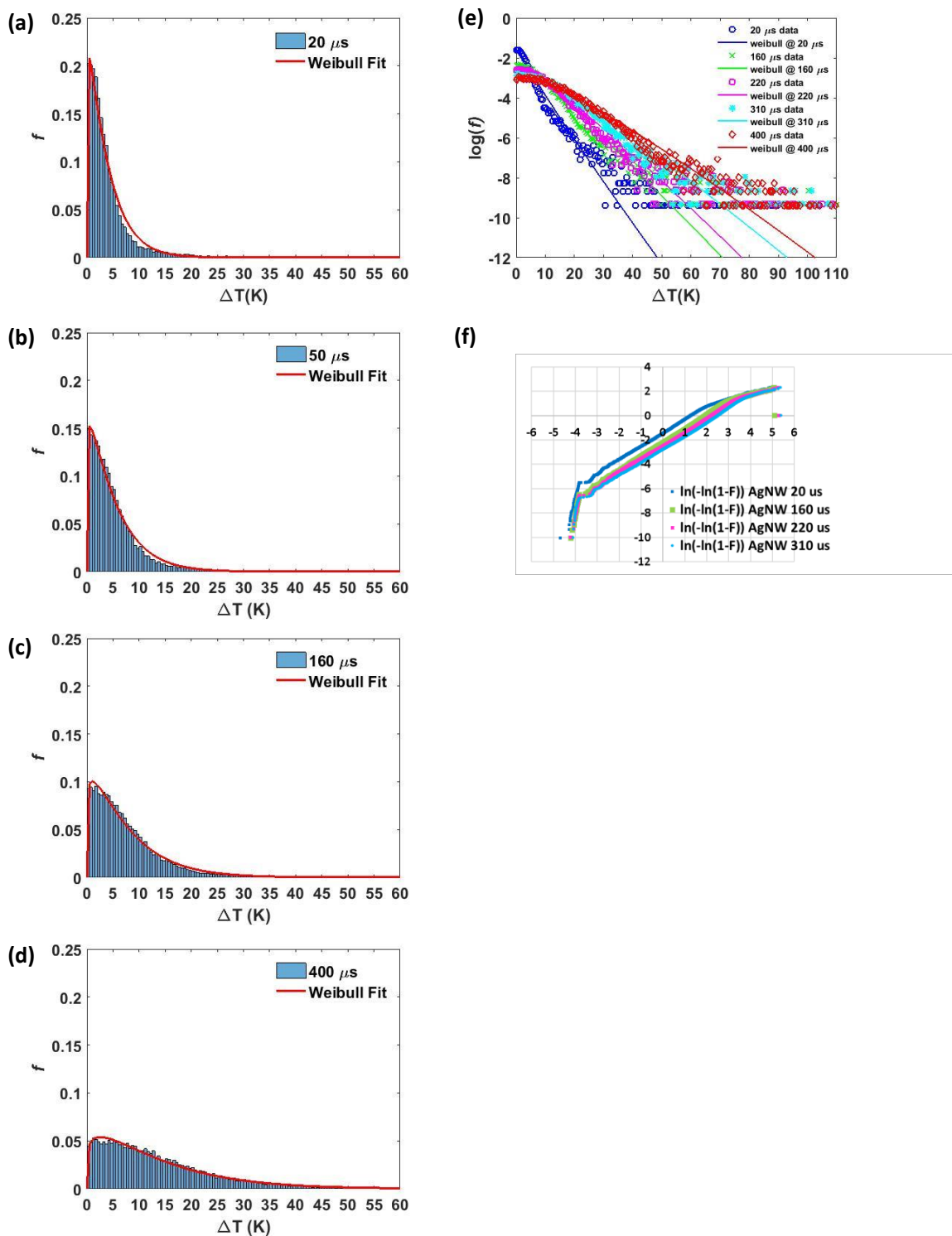


Fig. 7.4: Probability density function  $f$  vs.  $\Delta T$  at various time instants over heat diffusion time regime at (a) 20  $\mu\text{s}$ , (b) 50  $\mu\text{s}$ , (c) 160  $\mu\text{s}$ , and (d) 400  $\mu\text{s}$ . (e)  $\log(f)$  vs.  $\Delta T$  at various

time instants to take a closer look at the tail of the temperature distributions. (f)  $\log(-\log(1-F))$  vs.  $\log(\Delta T)$  at various time instants showing straight lines (signature of Weibull distributions).

However, we see that the shape parameter  $\beta$  increases with time (Fig. 7.5(a)) in contrast with the behavior seen in the self-heating time regime (Fig. 7.3(a)). The initial  $\beta$  value is  $\sim 1.07$ , which is the steady state  $\beta$  value at the end of the self-heating time regime and then it increases  $\sim 1.16$  within  $450 \mu\text{s}$ . As heat starts to spread, the temperature of the whole network including NW bodies as well as the substrate increases which reduces the standard deviation of the experimental data. This results in higher  $\beta$  values as time evolves.

The scale parameter  $\alpha$  increases (2K to 16K) with time but does not saturate within  $450 \mu\text{s}$  (Fig. 7.5(b)). This behavior of  $\alpha$  is consistent with long time domain transient thermal characteristics of microscopic hotspots.

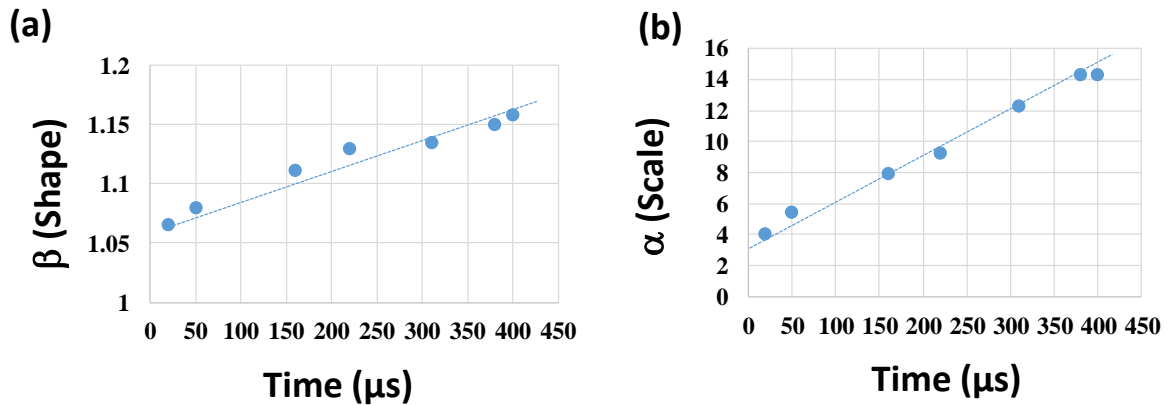


Fig. 7.5: Over the heat diffusion time regime, evolution of (a) shape parameter (b) scale parameter with time.

## 7.4 Simulation of Self-heating and Heat Diffusion in Silver Thin Film

Next, we simulate self-heating and heat diffusion for a uniform homogenous conductor e.g. silver thin film to see how the temperature distributions evolve over time.

The general heat transfer equation for a homogeneous thermal conductor is:

$$\frac{\delta \Delta T}{\delta t} = \frac{\kappa}{\rho C} \nabla^2(\Delta T) + \frac{1}{\rho C} Q_r \quad (7.2)$$

Here,  $\rho$  is the mass density,  $C$  is the specific heat,  $\kappa$  is the thermal conductivity, and  $Q_r$  is the generated heat per unit volume (unit  $\text{W}/\text{m}^3$ ) at position  $r$  for the system under consideration. With appropriate geometries, boundary conditions, and heat generation terms, this partial differential equation can be used to model either local self-heating (i.e. heat generation within the film) over  $0 - 10 \mu\text{s}$  time regime, or long-range heat diffusion through the channel region (i.e. silver film/quartz) over  $0 - 450 \mu\text{s}$ . We solve Eq. (7.2) using finite element analysis in PDETool in MATLAB for a 2D system consisting of 20 nm thin silver film on a quartz substrate (Fig. 7.6(a)). Since self-heating in silver thin film is a 3-D cylindrical heat problem and the PDETool (Partial Differential Equation Toolbox) of MATLAB supports 2-D geometry and requires the equation to be in Cartesian coordinates, we transformed the 3-D cylindrical geometry to 2-D Cartesian coordinate geometry according to section 4.6.2.

#### 7.4.1 Simulation of Self-heating in Silver Thin Film

We have used Eq. (7.2) with heat generation  $Q_r = 9.5 \times 10^4 \frac{\text{W}}{\text{m}^3}$  within a uniform continuous silver thin film over the time interval  $\tau_D = 0 - 10 \mu\text{s}$  to see how  $\Delta T$  distributions change due to local self-heating in order to compare/contrast those with nanostructured network based distributed conductors.  $Q_r$  is the generated heat per unit volume (unit  $\text{W}/\text{m}^3$ ) within a strip located  $r$  distance away from the center of the inner contact due to Joule heating caused by current  $I$  that flows radially uniformly from the inner contact to the outer contact.  $Q_r$  can be expressed as,  $Q_r = I^2 \frac{R_s}{(2\pi)^2 d r^2}$  (derivation details are provided in [2]) where  $R_s$  is the sheet resistance, and  $d$  is the thickness of the film. To make a fair comparison of the experimental data for the silver NW network with the thin film simulation results, we use comparable  $I \cong 50 \text{ mA}$  that flows through silver NW network and  $R_s \cong 30 \Omega/\text{sqr}$  which is the sheet resistance of the silver NW network so that the applied electrical power in both cases are the same. The thickness of the quartz substrate is taken as  $\sim 1 \mu\text{m}$  which is consistent with the heat diffusion length within quartz over  $10 \mu\text{s}$  time interval according to  $\sqrt{D_{\text{Quartz}} \tau} = \sqrt{1.4 \times 10^{-6} \frac{\text{m}^2}{\text{s}} \times 10 \mu\text{s}} \cong 3.7 \mu\text{m}$ . The spatial domain is chosen such that  $r' = 180 \mu\text{m}$  corresponds to the center of the inner contact and  $r' = 220 - 320 \mu\text{m}$  corresponds to the channel region. For the boundary representing the interface between silver film and air, we assume  $\text{grad}(\Delta T) = 0$  i.e. no incoming or outgoing heat flux. For all other boundaries, we assume Dirichlet boundary conditions,  $\Delta T = 0$  since the boundaries are located far away from the channel region

where heat is generated. No heat generation ( $Q_r = 0$ ) is assumed under the electrical contacts.

Fig. 7.6(a) shows the layout of the simulated structure. Fig. 7.6(b) show the temperature profile at  $\tau_D = 10 \mu\text{s}$ . Bulk  $\rho$ ,  $C$ ,  $\kappa$  values of silver and quartz are used in the simulation. We plotted  $\Delta T$  vs. distance at different  $\tau_D$ s as shown in solid line in Fig. 7.6(c). Since the Joule heating term  $Q_r$  has  $\frac{1}{r^2}$  dependency, we see that  $\Delta T$  falls from the edge of the inner contact. Fig. 7.6(d) shows  $\Delta T$  vs.  $\tau_D$  for different spatial locations at different distances within the film. All the temperature profiles show saturation with time showing thermal time constants  $\tau_{H\_Silver} \sim 100$  ns. We find that  $\tau_{H\_Silver}$  related to these spatial locations does not vary much with distance. Interestingly, we see that this behavior of  $\tau_{H\_Silver}$  with spatial distance is consistent to our previously reported  $\tau_H$  vs. distance relation for graphene-silver NW hybrid network based conductor where  $\tau_H$  of such network system originating from Joule heating at the NW-NW junction does not change with distance (Fig. 4.5(a)) [2].

Now, in order to get  $\Delta T$  distributions of the circular channel at different  $\tau_D$  s, we have taken  $\Delta T$  vs. distance profiles of Fig. 7.6(c) and converted those into pixels (1 pixel  $\sim 200 \text{ nm} \times 200 \text{ nm}$ ) in order to make a reasonable comparison with our experimental findings. Fig. 7.6(e) shows probability density distribution of temperature of silver film at  $\tau_D = 10 \mu\text{s}$ . Fig. 7.6(f) shows double-log plot of the temperature distribution of the film at  $\tau_D = 10 \mu\text{s}$ . The plot do not show characteristics straight line of a Weibull distribution.

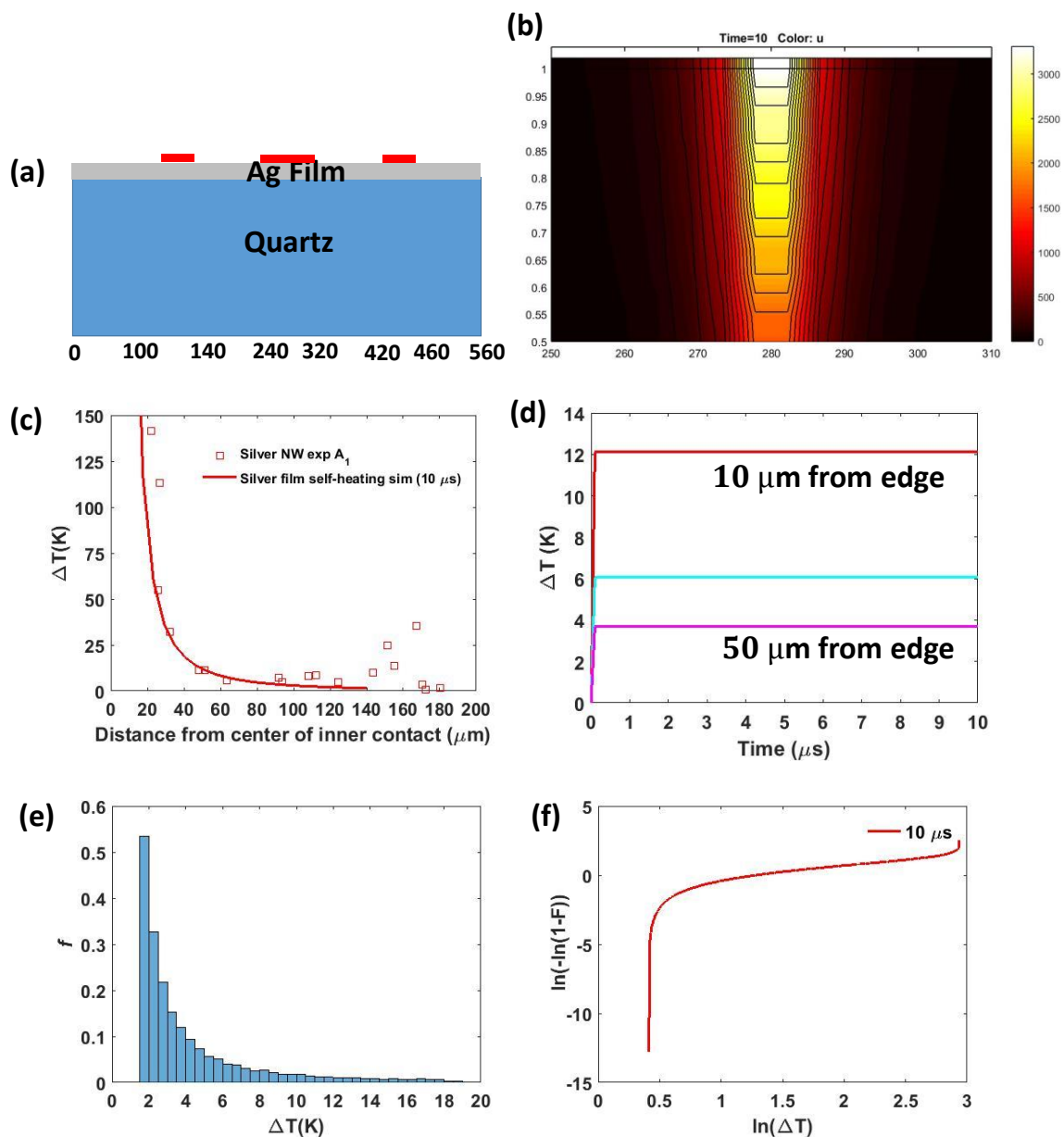


Fig. 7.6: (a) Device structure for self heating Simulation of silver thin film. (b)  $\Delta T$  profile at  $10 \mu\text{s}$ . (c)  $\Delta T$  vs. distance for different  $\tau_D$  s from  $200 \text{ ns}$  to  $10 \mu\text{s}$ . (d)  $\Delta T$  vs. time for different spatial locations. (e) pdf at  $10 \mu\text{s}$ . (f)  $\log(-\log(1-F))$  vs.  $\log(\Delta T)$  at  $10 \mu\text{s}$ .

### 7.4.2 Simulation of Heat Diffusion from Electrical Contacts to Silver Thin Film

The same partial differential Eq. (7.2) has been solved to simulate heat diffusion from the electrical contacts through silver thin film/quartz with heat generation  $Q = 0$  and the electrical contacts as heat sources over the time interval  $\tau_D = 0 - 450 \mu\text{s}$  when heat diffusion rather than local self-heating becomes predominant. The thickness of the silver film remains the same as before (20 nm) but thicker quartz substrate is considered (500  $\mu\text{m}$  thick) due to the longer time interval. For heat diffusion simulation, the spatial domain is chosen such that  $r'' = 240 - 320 \mu\text{m}$  corresponds to the inner contact and  $r'' = 100 - 140 \mu\text{m}$  and  $420 - 460 \mu\text{m}$  represent the outer contact. The boundary conditions for this system include Dirichlet boundary conditions corresponding to  $\Delta T$  at the contacts which are specified as  $f(t)$  since  $\Delta T$  within the contacts takes time to rise to its steady state value. The expression for the boundary condition for the inner (outer) contact has been obtained by fitting experimental transient  $\Delta T$  of the hotspot within the electrical contacts closest to the channel region. Details of the similar boundary conditions have been discussed in our previous publication [2].

The resulting boundary condition for the inner contact is:

$$\begin{aligned} \Delta T (r'', t) &= 52.5 * \left(1 - \exp\left(-\frac{t}{8.5}\right)\right) + 78 * \left(1 - \exp\left(-\frac{t}{185}\right)\right); | r'' \\ &= 240 - 320 \mu\text{m} \end{aligned}$$

The boundary condition for the outer contact is:

$$\begin{aligned} \Delta T (r'', t) &= 11.12 * \left(1 - \exp\left(-\frac{t}{4.8}\right)\right) + 8 * \left(1 - \exp\left(-\frac{t}{414}\right)\right); | r'' \\ &= 100 - 140 \mu\text{m}, 420 - 460 \mu\text{m} \end{aligned}$$

For all other boundaries, we assume  $grad(\Delta T) = 0$  i.e. no incoming or outgoing heat flux.

Fig. 7.7(a) shows the simulation results at  $\tau_D = 450 \mu\text{s}$ . Bulk values of  $\rho$ ,  $C$ ,  $\kappa$  parameters of silver and quartz are used in the simulation. The temperature profile at  $\tau_D = 450 \mu\text{s}$  shows that heat diffuses  $\sim 50 \mu\text{m}$  into the quartz over this time interval. We plotted the temperature profile within the film vs. distance from the inner contact at different  $\tau_{DS}$  as shown in solid line in Fig. 7.7(b). The profiles show heat diffuses  $\sim 50-60 \mu\text{m}$  from both the inner and the outer contact inside the film over this time. Fig. 7.7(c) shows the

temperature vs. time profiles for different locations within the film. The profiles do not saturate within this time interval which is consistent considering the thickness of the quartz. The temperature profiles vs. distance as shown in Fig. 7.7(b) is then converted to temperature vs. pixel profile as described in the self-heating simulation section.

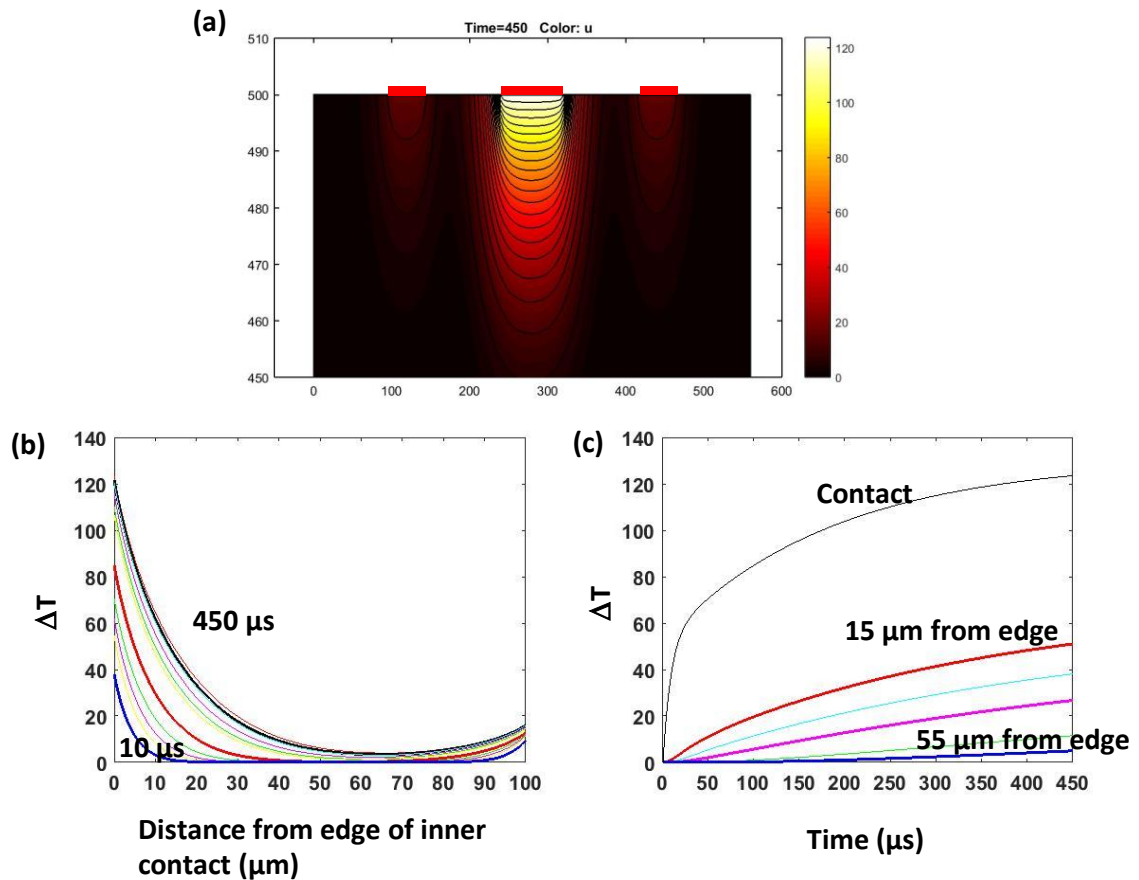


Fig. 7.7: Simulation results of heat diffusion through silver film (a)  $\Delta T$  profile at 450  $\mu\text{s}$ . (b)  $\Delta T$  vs. distance for different  $\tau_D$  s from 10  $\mu\text{s}$  to 450  $\mu\text{s}$ . (c)  $\Delta T$  vs. time for different spatial locations.

Fig. 7.8 shows probability density distribution of temperature of silver film at different  $\tau_D$  s. Fig. 7.9 shows the corresponding double-log plots of the temperature distributions of the film. The plots show characteristics straight line of Weibull distributions.

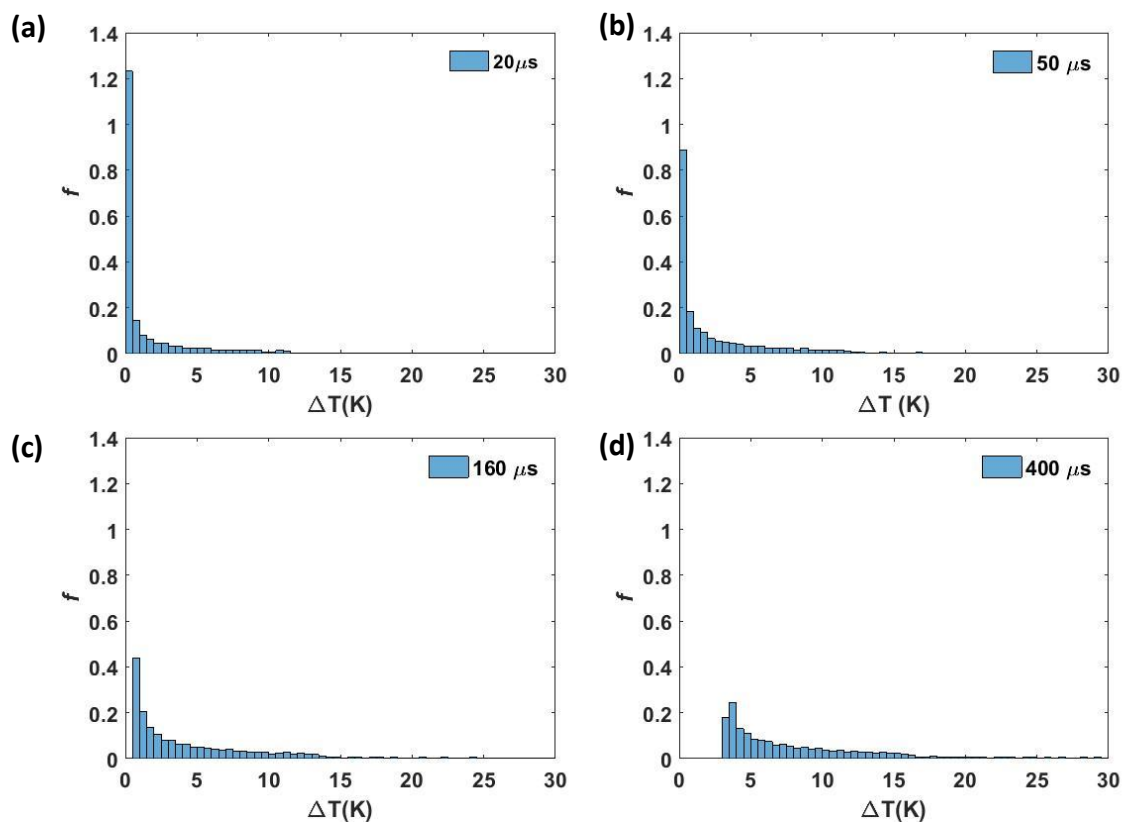


Fig. 7.8: Probability distribution function at different time instants (a)  $\tau_D = 20 \mu\text{s}$ , (b)  $\tau_D = 50 \mu\text{s}$ , (c)  $\tau_D = 160 \mu\text{s}$ , and (d)  $\tau_D = 400 \mu\text{s}$ .

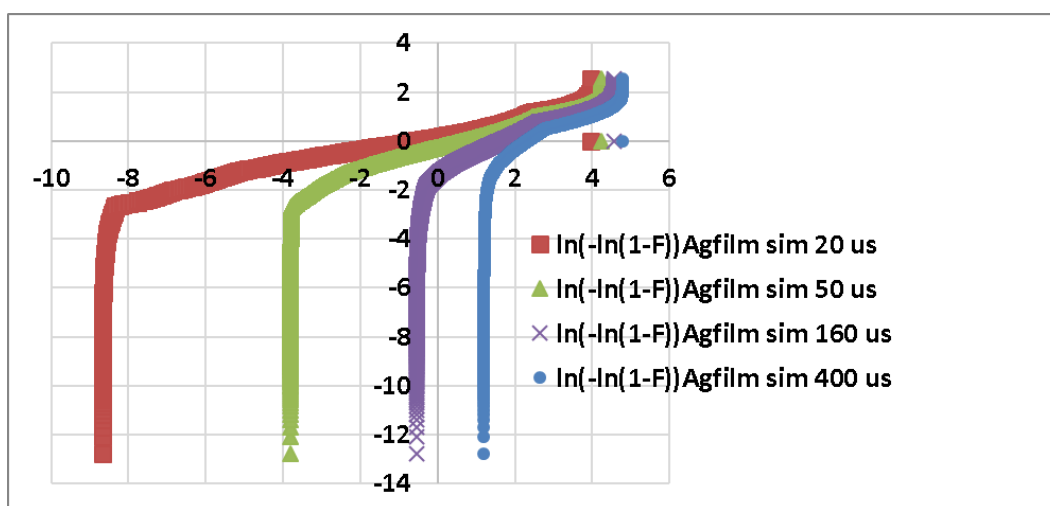


Fig. 7.9:  $\log(-\log(1-F))$  vs.  $\log(\Delta T)$  at corresponding time instants of  $\tau_D = 20 \mu\text{s}$ ,  $50 \mu\text{s}$ ,  $160 \mu\text{s}$ , and  $400 \mu\text{s}$ .

Fig. 7.10(a) shows the evolution of shape parameter and a comparison with our experimental shape parameters. In this longer time regime, we see the shape parameter from simulation to increase with time, which is similar to experimentally obtained silver NW network shape parameter for long time domain but in contrast with experimental silver NW network self-heating time domain shape parameter (Fig. 7.3(a)). The scale parameter increase with time similar to the silver NW network in this longer range time regime.

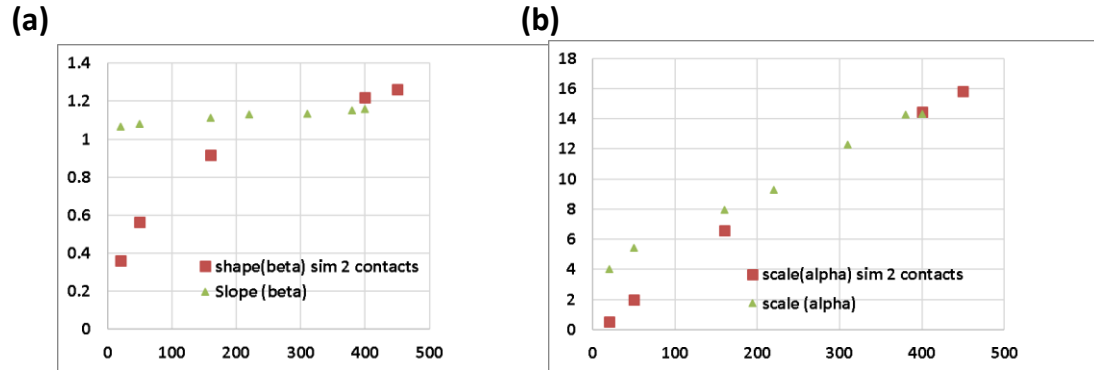


Fig. 7.10: Evolution of (a) shape and (b) scale parameter with time (0 – 450  $\mu\text{s}$ ) as obtained from heat diffusion simulation within silver film.

## 7.5 Conclusion

In this chapter, we study the evolution of temperature distributions of NWs in silver NW network with time. We found that at each time instant, the distributions could be described by a Weibull distribution. Our study finds that the Weibull distributions exhibit distinctive signatures of local self-heating in the vicinity of NW-NW junctions vs. heat spreading through network. The shape parameter decreases with time over the time domain of 0 – 10  $\mu\text{s}$  when temperature rise is mostly due to the self-heating of the NW-NW junctions. In contrast, it increases with time over 10 – 450  $\mu\text{s}$  when heat starts to diffuse through the network/substrate from nearby extrinsic heat sources (e.g. heating from electrical contacts) and temperature of the NWs rises mostly due to this spreading of heat. Simulation of thin silver film of comparable thickness on quartz shows that while increase of the shape parameter with time occurs in the heat spreading time regime but it does not happen in case of self-heating of the film. This suggests that decrease of shape parameter probably is a unique characteristic of non-homogenous networks over self-heating time domain when intrinsic thermal properties of the network prevails.

## 8. SUMMARY, CONCLUSION, AND FUTURE WORK

### 8.1 Research Objective, Summary and Conclusion

The primary objective of this thesis was to understand the evolution of microscopic current conducting pathways in 2D non-homogenous network conductors. We took self-heating at the resistive junctions of crossing nanowires (NWs) as a means to semi-quantitatively determine the current flowing through these NW-NW junctions. We utilized transient thermoreflectance (TR) imaging technique that provides high temporal and spatial resolution to study multiple hotspots simultaneously. Since hotspots are the vulnerable links within a network and are prone to breakdown due to their high temperature, understanding the current flow and their time dependent temperature rise is important to reliably use it in emerging applications in flexible photovoltaics, LED, displays etc. as transparent conducting electrodes. In these novel applications, non-homogenous network based transparent conductors have been increasingly used due to their mechanical flexibility, better sheet resistance performance at higher transmittance, and most importantly, lower cost compared to traditional oxide based transparent conductors.

In Chapter 4, we discussed about the time dependent temperature rise of hotspots in hybrid network and found two thermal time constants associated with these hotspots. In this study, each hotspot consists of multiple junctions, therefore the spatial resolution is low but the TR images provide an overall end-to-end view of all the hotspots formed within the network from one electrical contact to the other and give the opportunity to study multiple hotspots simultaneously. Using the steady state temperature amplitude values and thermal time constants of multiple hotspots located at different spatial distances within the network and analyzing their behavior, we determined the physical origin of the time constants. Most importantly, we resolved the time regime over which temperature rise is mainly due to the local self-heating of the junctions (therefore, represents intrinsic properties of the junctions) and the time regime over which temperature rise is due to diffused heat from a nearby heat source e.g. heating at the electrical contacts spreading

through the network and substrate (therefore, represents extrinsic properties of network/substrate). In our subsequent studies, we focused on the self-heating time zone to learn about the hotspot characteristics.

In Chapter 5, we advance one step closer towards our goal of determining the current at the NW-NW junctions. Using higher resolution TR imaging, we looked into the details of time dependent temperature rise of individual hotspots where each hotspot corresponds to one NW-NW junction. We also observed how the temperature profile changes along the length of two crossing NWs. Using a heat transfer model, we estimated the power at the junction and the percentage each constituent NW conducts.

In Chapter 6, we looked into the material/composition dependent variation of hotspot characteristics by taking into account two different non-homogenous networks with different junction configurations and transport physics. We analyzed how the average hotspot temperature, number of hotspots, and their spatial distributions vary within the self-heating time regime and how these experimental observations can be explained by considering differences of the network configurations in terms of both resistive pathways and local heat dissipation pathways.

In Chapter 7, we explored the evolution of overall temperature distributions of the NWs including hotspots as a function of time. We observed that temperature distributions of a silver NW network at different time instants could be expressed as Weibull distributions. The shape parameters of the Weibull distributions, however, change differently with time based on the prevalent thermal process (i.e. local self-heating in the vicinity of the NW-NW junctions or heat diffusion through the network/substrate).

Collectively, these studies help us to understand the evolution of hotspot temperature as a function of time, space and network configuration. Even though we are able to quantify the power generated at the junctions, the current flowing through these junctions is yet to be determined. In order to resolve the current, electrical resistances of the junctions need to be determined. Since the annealing conditions configure the junctions in a similar way, electrical measurements of junction resistances at few representative portions of the network will be sufficient to find out the distributions of junction electrical resistances.

## 8.2 Future Work

There are several topics related to this work that may be interesting to explore. For example, we observed in Chapter 4 that the temperature profile during the heating cycle in response to longer device pulses of 450  $\mu\text{s}$  does not saturate. It could be useful to learn when the temperature profile saturates experimentally by utilizing pulses longer than 450  $\mu\text{s}$  and how it relates with the substrate thickness.

In Chapter 5, we investigated the characteristics of microscopic hotspots formed at the junction of two crossing NWs within silver NW network. Similar high-resolution TR imaging can be performed on hybrid network in order to compare/contrast the temperature vs. length profiles in these two types of network and to determine the power at the hotspots formed within hybrid network.

In one of our transient studies, we observed recurrent turning on/off of a portion of a hybrid network that caused the temperature to rise/fall with time. We also observed structural changes of NWs with time from the captured CCD images. It could be an interesting research topic to correlate the change of morphology of the network with the time dependent repeated/reversible redistributions of current pathways.

In a reliability related study, we observed generation and elimination of hotspots with changing voltage bias. We also observed that hybrid network is more stress tolerant (breakdown occurs later) and has extended lifetime compared to silver NW network. This research direction could be explored more to learn about the reliability aspects of the hotspots or the non-homogenous networks.

## LIST OF REFERENCES

- [1] S. R. Das, S. Sadeque, C. Jeong, R. Chen, M. A. Alam, and D. B. Janes, "Copercolating Networks: An Approach for Realizing High-Performance Transparent Conductors using Multicomponent Nanostructured Networks," 2016.
- [2] S. Sadeque *et al.*, "Transient Thermal Response of Hotspots in Graphene-Silver Nanowire Hybrid Transparent Conducting Electrodes," *IEEE Transactions on Nanotechnology*, 2018.
- [3] B. G. Lewis and D. C. Paine, "Applications and processing of transparent conducting oxides," *Mrs Bulletin*, vol. 25, no. 08, pp. 22-27, 2000.
- [4] Ç. Kılıç and A. Zunger, "Origins of coexistence of conductivity and transparency in SnO<sub>2</sub>," *Physical Review Letters*, vol. 88, no. 9, p. 095501, 2002.
- [5] H. Liu, V. Avrutin, N. Izyumskaya, Ü. Özgür, and H. Morkoç, "Transparent conducting oxides for electrode applications in light emitting and absorbing devices," *Superlattices and Microstructures*, vol. 48, no. 5, pp. 458-484, 2010.
- [6] K. L. Chopra, S. Major, and D. K. Pandya, "Transparent conductors—a status review," *Thin solid films*, vol. 102, no. 1, pp. 1-46, 1983.
- [7] R. G. Gordon, "Criteria for choosing transparent conductors," *MRS bulletin*, vol. 25, no. 08, pp. 52-57, 2000.
- [8] K. Roy, B. Jung, D. Peroulis, and A. Raghunathan, "Integrated systems in the more-than-moore era: designing low-cost energy-efficient systems using heterogeneous components," *IEEE Design & Test*, vol. 33, no. 3, pp. 56-65, 2016.
- [9] M. F. L. De Volder, S. H. Tawfick, R. H. Baughman, and A. J. Hart, "Carbon nanotubes: present and future commercial applications," *science*, vol. 339, no. 6119, pp. 535-539, 2013.
- [10] L. Hu, H. S. Kim, J.-Y. Lee, P. Peumans, and Y. Cui, "Scalable coating and properties of transparent, flexible, silver nanowire electrodes," *ACS nano*, vol. 4, no. 5, pp. 2955-2963, 2010.
- [11] Z. Wu *et al.*, "Transparent, conductive carbon nanotube films," *Science*, vol. 305, no. 5688, pp. 1273-1276, 2004.
- [12] D. Zhang *et al.*, "Synthesis of ultralong copper nanowires for high-performance transparent electrodes," *Journal of the American Chemical Society*, vol. 134, no. 35, pp. 14283-14286, 2012.
- [13] P. E. Lyons *et al.*, "High-performance transparent conductors from networks of gold nanowires," *The Journal of Physical Chemistry Letters*, vol. 2, no. 24, pp. 3058-3062, 2011.
- [14] J. Van De Groep, P. Spinelli, and A. Polman, "Transparent conducting silver nanowire networks," *Nano letters*, vol. 12, no. 6, pp. 3138-3144, 2012.
- [15] T. Tokuno, M. Nogi, J. Jiu, and K. Suganuma, "Hybrid transparent electrodes of silver nanowires and carbon nanotubes: a low-temperature solution process," *Nanoscale research letters*, vol. 7, no. 1, p. 281, 2012.
- [16] I. N. Kholmanov *et al.*, "Improved electrical conductivity of graphene films integrated with metal nanowires," *Nano letters*, vol. 12, no. 11, pp. 5679-5683, 2012.
- [17] Y. Ahn, Y. Jeong, and Y. Lee, "Improved thermal oxidation stability of solution-processable silver nanowire transparent electrode by reduced graphene oxide," *ACS applied materials & interfaces*, vol. 4, no. 12, pp. 6410-6414, 2012.

- [18] C. Jeong, P. Nair, M. Khan, M. Lundstrom, and M. A. Alam, "Prospects for nanowire-doped polycrystalline graphene films for ultratransparent, highly conductive electrodes," *Nano letters*, vol. 11, no. 11, pp. 5020-5025, 2011.
- [19] R. Chen, S. R. Das, C. Jeong, M. R. Khan, D. B. Janes, and M. A. Alam, "Co-Percolating Graphene-Wrapped Silver Nanowire Network for High Performance, Highly Stable, Transparent Conducting Electrodes," *Advanced Functional Materials*, vol. 23, no. 41, pp. 5150-5158, 2013.
- [20] B. Deng *et al.*, "Roll-to-roll encapsulation of metal nanowires between graphene and plastic substrate for high-performance flexible transparent electrodes," *Nano letters*, 2015.
- [21] L. J. Andrés *et al.*, "Rapid synthesis of ultra-long silver nanowires for tailor-made transparent conductive electrodes: proof of concept in organic solar cells," *Nanotechnology*, vol. 26, no. 26, p. 265201, 2015.
- [22] S. De, P. J. King, P. E. Lyons, U. Khan, and J. N. Coleman, "Size effects and the problem with percolation in nanostructured transparent conductors," *Acs Nano*, vol. 4, no. 12, pp. 7064-7072, 2010.
- [23] S. De *et al.*, "Silver nanowire networks as flexible, transparent, conducting films: extremely high DC to optical conductivity ratios," *ACS nano*, vol. 3, no. 7, pp. 1767-1774, 2009.
- [24] K. Maize *et al.*, "Super-Joule heating in graphene and silver nanowire network," *Applied Physics Letters*, vol. 106, no. 14, p. 143104, 2015.
- [25] C.-C. Chen *et al.*, "Visibly transparent polymer solar cells produced by solution processing," *Acs Nano*, vol. 6, no. 8, pp. 7185-7190, 2012.
- [26] Z. Ertekin, U. Tamer, and K. Pekmez, "Cathodic electrochemical deposition of Magnéli phases  $Ti_nO_{2n-1}$  thin films at different temperatures in acetonitrile solution," *Electrochimica Acta*, vol. 163, pp. 77-81, 2015.
- [27] (2017, February). <http://www.acsmaterial.com/silver-nanowire-500mg-2226.html>.
- [28] S. Zhu *et al.*, "Transferable self-welding silver nanowire network as high performance transparent flexible electrode," *Nanotechnology*, vol. 24, no. 33, p. 335202, 2013.
- [29] M. C. Çakır, D. Çalışkan, B. Bütün, and E. Özbay, "Planar Indium Tin Oxide Heater for Improved Thermal Distribution for Metal Oxide Micromachined Gas Sensors," *Sensors*, vol. 16, no. 10, p. 1612, 2016.
- [30] S. R. Das *et al.*, "Evidence of Universal Temperature Scaling in Self-Heated Percolating Networks," *Nano letters*, vol. 16, no. 5, pp. 3130-3136, 2016.
- [31] H. H. Khaligh and I. A. Goldthorpe, "Failure of silver nanowire transparent electrodes under current flow," *Nanoscale research letters*, vol. 8, no. 1, p. 1, 2013.
- [32] T. Sannicolo *et al.*, "Direct Imaging of the Onset of Electrical Conduction in Silver Nanowire Networks by Infrared Thermography: Evidence of Geometrical Quantized Percolation," *Nano Letters*, vol. 16, no. 11, pp. 7046-7053, 2016.
- [33] J.-Z. Chen, H. Ahn, S.-C. Yen, and Y.-J. Tsai, "Thermally Induced Percolational Transition and Thermal Stability of Silver Nanowire Networks Studied by THz Spectroscopy," *ACS applied materials & interfaces*, vol. 6, no. 23, pp. 20994-20999, 2014.
- [34] M. Bobinger, D. Angeli, S. Colasanti, P. La Torraca, L. Larcher, and P. Lugli, "Infrared, transient thermal, and electrical properties of silver nanowire thin films for transparent heaters and energy-efficient coatings," *physica status solidi (a)*, 2016.
- [35] S. Ji, W. He, K. Wang, Y. Ran, and C. Ye, "Thermal response of transparent silver nanowire/PEDOT: PSS film heaters," *Small*, vol. 10, no. 23, pp. 4951-4960, 2014.

- [36] M. Engel, M. Steiner, J.-W. T. Seo, M. C. Hersam, and P. Avouris, "Hot Spot Dynamics in Carbon Nanotube Array Devices," *Nano letters*, vol. 15, no. 3, pp. 2127-2131, 2015.
- [37] S. Ishibashi, Y. Higuchi, Y. Ota, and K. Nakamura, "Low resistivity indium–tin oxide transparent conductive films. II. Effect of sputtering voltage on electrical property of films," *Journal of Vacuum Science & Technology A: Vacuum, Surfaces, and Films*, vol. 8, no. 3, pp. 1403-1406, 1990.
- [38] W. Tang and D. C. Cameron, "Aluminum-doped zinc oxide transparent conductors deposited by the sol-gel process," *Thin solid films*, vol. 238, no. 1, pp. 83-87, 1994.
- [39] A. R. Madaria, A. Kumar, F. N. Ishikawa, and C. Zhou, "Uniform, highly conductive, and patterned transparent films of a percolating silver nanowire network on rigid and flexible substrates using a dry transfer technique," *Nano Research*, vol. 3, no. 8, pp. 564-573, 2010.
- [40] V. Scardaci, R. Coull, P. E. Lyons, D. Rickard, and J. N. Coleman, "Spray deposition of highly transparent, low-resistance networks of silver nanowires over large areas," *Small*, vol. 7, no. 18, pp. 2621-2628, 2011.
- [41] M.-S. Lee *et al.*, "High-performance, transparent, and stretchable electrodes using graphene–metal nanowire hybrid structures," *Nano letters*, vol. 13, no. 6, pp. 2814-2821, 2013.
- [42] J.-Y. Lee, S. T. Connor, Y. Cui, and P. Peumans, "Solution-processed metal nanowire mesh transparent electrodes," *Nano letters*, vol. 8, no. 2, pp. 689-692, 2008.
- [43] M. D. Benoy, E. M. Mohammed, M. Suresh Babu, P. J. Binu, and B. Pradeep, "Thickness dependence of the properties of indium tin oxide (ITO) FILMS prepared by activated reactive evaporation," *Brazilian Journal of Physics*, vol. 39, no. 4, p. 629, 2009.
- [44] H.-Z. Geng, K. K. Kim, K. P. So, Y. S. Lee, Y. Chang, and Y. H. Lee, "Effect of acid treatment on carbon nanotube-based flexible transparent conducting films," *Journal of the American Chemical Society*, vol. 129, no. 25, pp. 7758-7759, 2007.
- [45] B. N. Chandrashekar *et al.*, "Roll-to-roll green transfer of CVD graphene onto plastic for a transparent and flexible triboelectric nanogenerator," *Advanced Materials*, vol. 27, no. 35, pp. 5210-5216, 2015.
- [46] J. Fang, S. R. Das, L. J. Prokopenko, V. M. Shalaev, D. B. Janes, and A. V. Kildishev, "Time-domain modeling of silver nanowires-graphene transparent conducting electrodes," pp. 88060I-88060I: International Society for Optics and Photonics.
- [47] V. K. Jain and A. P. Kulshreshtha, "Indium-tin-oxide transparent conducting coatings on silicon solar cells and their "figure of merit", " *Solar Energy Materials*, vol. 4, no. 2, pp. 151-158, 1981.
- [48] S. Shin *et al.*, "Direct Observation of Self-heating in III-V Gate-All-Around Nanowire MOSFETs," *Electron Devices, IEEE Transactions on*, vol. 62, no. 11, pp. 3516-3523, 2015.
- [49] M. A. Wahab, S. H. Shin, and M. A. Alam, "Spatio-Temporal Mapping of Device Temperature due to Self-Heating in Sub-22 nm Transistors," IEEE International Reliability Physics Symposium (IRPS), 2016.
- [50] M. A. Wahab, S. Shin, and M. A. Alam, "3D Modeling of Spatio-temporal Heat-transport in III-V Gate-all-around Transistors Allows Accurate Estimation and Optimization of Nanowire Temperature," *Electron Devices, IEEE Transactions on*, vol. 62, no. 11, pp. 3595-3604, 2015.
- [51] K. Yazawa, D. Kendig, K. Maize, and A. Shakouri, "Transient thermal characterization of HEMT devices," pp. 1-4: IEEE.

- [52] K. Maize, A. Kundu, G. Xiong, K. Saviers, T. S. Fisher, and A. Shakouri, "Electroreflectance imaging of gold–H<sub>3</sub>PO<sub>4</sub> supercapacitors. Part I: experimental methodology," *Analyst*, vol. 141, no. 4, pp. 1448-1461, 2016.
- [53] R. Singh, J. Christofferson, Z. Bian, J. Nurnus, A. Schubert, and A. Shakouri, "Characterization of Thin-film Thermoelectric Micro-modules using Transient Harman ZT Measurement and Near-IR Thermorefectance," vol. 1044, pp. 1044-U10: Cambridge Univ Press.
- [54] K. Maize, E. Heller, D. Dorsey, and A. Shakouri, "Fast transient thermorefectance CCD imaging of pulsed self heating in AlGaIn/GaN power transistors," pp. CD-2: IEEE International Reliability Physics Symposium (IRPS), 2013.
- [55] A. Shakouri, K. Maize, P. Jackson, X. Wang, B. Vermeersch, and K. Yazawa, "Ultrafast submicron thermal characterization of integrated circuits," pp. 1-2: IEEE.
- [56] Y. Ezzahri, J. Christofferson, K. Maize, and A. Shakouri, "Short time transient behavior of SiGe-based microrefrigerators," Cambridge Univ Press.
- [57] K. Maize, D. Kendig, A. Shakouri, and V. Vashchenko, "Nanosecond transient thermorefectance imaging of snapback in semiconductor controlled rectifiers," pp. EL-4: IEEE.
- [58] J. S. Woo *et al.*, "Electrically robust metal nanowire network formation by in-situ interconnection with single-walled carbon nanotubes," *Scientific reports*, vol. 4, 2014.
- [59] J. E. Shaw, A. Perumal, D. D. C. Bradley, P. N. Stavrinou, and T. D. Anthopoulos, "Nanoscale current spreading analysis in solution-processed graphene oxide/silver nanowire transparent electrodes via conductive atomic force microscopy," *Journal of Applied Physics*, vol. 119, no. 19, p. 195501, 2016.
- [60] P. N. Nirmalraj *et al.*, "Manipulating connectivity and electrical conductivity in metallic nanowire networks," *Nano letters*, vol. 12, no. 11, pp. 5966-5971, 2012.
- [61] J. A. Fairfield, C. Ritter, A. T. Bellew, E. K. McCarthy, M. S. Ferreira, and J. J. Boland, "Effective electrode length enhances electrical activation of nanowire networks: experiment and simulation," *ACS nano*, vol. 8, no. 9, pp. 9542-9549, 2014.
- [62] P. N. Nirmalraj, P. E. Lyons, S. De, J. N. Coleman, and J. J. Boland, "Electrical connectivity in single-walled carbon nanotube networks," *Nano letters*, vol. 9, no. 11, pp. 3890-3895, 2009.
- [63] (April, 2017). <https://www.mathworks.com/help/pde/ug/heat-distribution-in-a-radioactive-rod.html?requestedDomain=www.mathworks.com>.
- [64] E. Pop, V. Varshney, and A. K. Roy, "Thermal properties of graphene: Fundamentals and applications," *MRS bulletin*, vol. 37, no. 12, pp. 1273-1281, 2012.
- [65] Z. Cheng, M. Han, P. Yuan, S. Xu, B. A. Cola, and X. Wang, "Strongly Anisotropic Thermal and Electrical Conductivities of Self-assembled Silver Nanowire Network," *arXiv preprint arXiv:1603.06845*, 2016.
- [66] G. Eda, G. Fanchini, and M. Chhowalla, "Large-area ultrathin films of reduced graphene oxide as a transparent and flexible electronic material," *Nature nanotechnology*, vol. 3, no. 5, pp. 270-274, 2008.
- [67] R. Singh, J. Christofferson, Z. Bian, J. Nurnus, A. Schubert, and A. Shakouri, "Characterization of Thin-film Thermoelectric Micro-modules using Transient Harman ZT Measurement and Near-IR Thermorefectance," in *MRS Proceedings*, vol. 1044, pp. 1044-U10:., January, 2007, vol. 1044, pp. 1044-U10: Cambridge Univ Press.
- [68] A. Shakouri, K. Maize, P. Jackson, X. Wang, B. Vermeersch, and K. Yazawa, "Ultrafast submicron thermal characterization of integrated circuits," in *19<sup>th</sup> IEEE*

- International Symposium on the Physical and Failure Analysis of Integrated Circuits (IPFA)*, 2012., pp. 1-2.
- [69] Y. Ezzahri, J. Christofferson, K. Maize, and A. Shakouri, "Short time transient behavior of SiGe-based microrefrigerators," in *Journal of Applied Physics* 106.11 (2009): 114503: Cambridge Univ Press.
- [70] K. Maize, D. Kendig, A. Shakouri, and V. Vashchenko, "Nanosecond transient thermorefectance imaging of snapback in semiconductor controlled rectifiers," in *IEEE International Reliability Physics Symposium (IRPS)*, 2011, pp. EL-4.
- [71] S. Hong *et al.*, "Highly stretchable and transparent metal nanowire heater for wearable electronics applications," *Advanced materials*, vol. 27, no. 32, pp. 4744-4751, 2015.
- [72] H. Zhai, R. Wang, X. Wang, Y. Cheng, L. Shi, and J. Sun, "Transparent heaters based on highly stable Cu nanowire films," *Nano Research*, vol. 9, no. 12, pp. 3924-3936, 2016.
- [73] H.-G. Cheong, D.-W. Song, and J.-W. Park, "Transparent film heaters with highly enhanced thermal efficiency using silver nanowires and metal/metal-oxide blankets," *Microelectronic Engineering*, vol. 146, pp. 11-18, 2015.
- [74] K. Yazawa, D. Kendig, D. Hernandez, K. Maze, and A. Shakouri, "Challenges and opportunities for transient thermal imaging of microelectronic devices," in *18th IEEE International Workshop on Thermal Investigations of ICs and Systems (THERMINIC)*, 2012, pp. 1-4.
- [75] K. Yazawa, D. Kendig, A. Shakouri, A. Ziabari, and A. Shakouri, "Thermal imaging of nanometer features," pp. 495-500: 15th IEEE Intersociety Conference on Thermal and Thermomechanical Phenomena in Electronic Systems (ITherm), 2016.
- [76] S. Sadeque *et al.*, "Transient Thermal Response of Hotspots in Graphene-Silver Nanowire Hybrid Transparent Conducting Electrodes," Unpublished Work, 2017.
- [77] J.-Y. Lee, S. T. Connor, Y. Cui, and P. Peumans, "Semitransparent organic photovoltaic cells with laminated top electrode," *Nano letters*, vol. 10, no. 4, pp. 1276-1279, 2010.
- [78] B. E. Hardin, W. Gaynor, I. K. Ding, S.-B. Rim, P. Peumans, and M. D. McGehee, "Laminating solution-processed silver nanowire mesh electrodes onto solid-state dye-sensitized solar cells," *Organic Electronics*, vol. 12, no. 6, pp. 875-879, 2011.
- [79] W. Gaynor, G. F. Burkhard, M. D. McGehee, and P. Peumans, "Smooth nanowire/polymer composite transparent electrodes," *Advanced Materials*, vol. 23, no. 26, pp. 2905-2910, 2011.
- [80] W. Gaynor, J.-Y. Lee, and P. Peumans, "Fully solution-processed inverted polymer solar cells with laminated nanowire electrodes," *ACS nano*, vol. 4, no. 1, pp. 30-34, 2009.
- [81] T. Tokuno *et al.*, "Fabrication of silver nanowire transparent electrodes at room temperature," *Nano research*, vol. 4, no. 12, pp. 1215-1222, 2011.
- [82] E. C. Garnett *et al.*, "Self-limited plasmonic welding of silver nanowire junctions," *Nature materials*, vol. 11, no. 3, pp. 241-249, 2012.
- [83] A. Bejan, *Convection heat transfer*. John wiley & sons, 2013.
- [84] V. Bahadur, J. Xu, Y. Liu, and T. S. Fisher, "Thermal resistance of nanowire-plane interfaces," *TRANSACTIONS-AMERICAN SOCIETY OF MECHANICAL ENGINEERS JOURNAL OF HEAT TRANSFER*, vol. 127, no. 6, p. 664, 2005.
- [85] J. N. Israelachvili, *Intermolecular and surface forces*. Academic press, 2011.
- [86] F. L. Leite, C. C. Bueno, A. L. Da Róz, E. C. Ziemath, and O. N. Oliveira, "Theoretical models for surface forces and adhesion and their measurement using

- atomic force microscopy," *International journal of molecular sciences*, vol. 13, no. 10, pp. 12773-12856, 2012.
- [87] Z. Cheng, L. Liu, S. Xu, M. Lu, and X. Wang, "Temperature dependence of electrical and thermal conduction in single silver nanowire," *Scientific reports*, vol. 5, pp. 10718-10718, 2015.
- [88] G. Wang and X. Li, "Predicting Young's modulus of nanowires from first-principles calculations on their surface and bulk materials," *Journal of Applied Physics*, vol. 104, no. 11, p. 113517, 2008.
- [89] Y. Zhu *et al.*, "Size effects on elasticity, yielding, and fracture of silver nanowires: In situ experiments," *Physical review B*, vol. 85, no. 4, p. 045443, 2012.
- [90] F. Selzer *et al.*, "Electrical limit of silver nanowire electrodes: Direct measurement of the nanowire junction resistance," *Applied Physics Letters*, vol. 108, no. 16, p. 163302, 2016.
- [91] A. T. Bellew, H. G. Manning, C. Gomes da Rocha, M. S. Ferreira, and J. J. Boland, "Resistance of Single Ag Nanowire Junctions and Their Role in the Conductivity of Nanowire Networks," *ACS nano*, vol. 9, no. 11, pp. 11422-11429, 2015.
- [92] A. Ziabari *et al.*, "Sub-diffraction limit thermal imaging for HEMT devices," pp. 82-87: IEEE.
- [93] Q. Nian *et al.*, "Crystalline nanojoining silver nanowire percolated networks on flexible substrate," *ACS nano*, vol. 9, no. 10, pp. 10018-10031, 2015.
- [94] T.-B. Song *et al.*, "Nanoscale joule heating and electromigration enhanced ripening of silver nanowire contacts," *ACS nano*, vol. 8, no. 3, pp. 2804-2811, 2014.
- [95] S. Nam, H. W. Cho, S. Lim, D. Kim, H. Kim, and B. J. Sung, "Enhancement of electrical and thermomechanical properties of silver nanowire composites by the introduction of nonconductive nanoparticles: experiment and simulation," *ACS nano*, vol. 7, no. 1, pp. 851-856, 2012.
- [96] R. M. Mutiso, M. C. Sherrott, A. R. Rathmell, B. J. Wiley, and K. I. Winey, "Integrating simulations and experiments to predict sheet resistance and optical transmittance in nanowire films for transparent conductors," *ACS nano*, vol. 7, no. 9, pp. 7654-7663, 2013.
- [97] S. Coskun, E. S. Ates, and H. E. Unalan, "Optimization of silver nanowire networks for polymer light emitting diode electrodes," *Nanotechnology*, vol. 24, no. 12, p. 125202, 2013.
- [98] C. Mayousse, C. Celle, A. Fraczkiewicz, and J.-P. Simonato, "Stability of silver nanowire based electrodes under environmental and electrical stresses," *Nanoscale*, vol. 7, no. 5, pp. 2107-2115, 2015.
- [99] J. L. Elechiguerra, L. Larios-Lopez, C. Liu, D. Garcia-Gutierrez, A. Camacho-Bragado, and M. J. Yacaman, "Corrosion at the nanoscale: the case of silver nanowires and nanoparticles," *Chemistry of Materials*, vol. 17, no. 24, pp. 6042-6052, 2005.
- [100] H. H. Khaligh *et al.*, "The Joule heating problem in silver nanowire transparent electrodes," *Nanotechnology*, vol. 28, no. 42, p. 425703, 2017.
- [101] B. Deng *et al.*, "Roll-to-roll encapsulation of metal nanowires between graphene and plastic substrate for high-performance flexible transparent electrodes," *Nano letters*, vol. 15, no. 6, pp. 4206-4213, 2015.
- [102] N. Ye *et al.*, "Silver nanowire-graphene hybrid transparent conductive electrodes for highly efficient inverted organic solar cells," *Nanotechnology*, vol. 28, no. 30, p. 305402, 2017.
- [103] M. P. Gupta and S. Kumar, "Numerical study of electrical transport in co-percolative metal nanowire-graphene thin-films," *Journal of Applied Physics*, vol. 120, no. 17, p. 175106, 2016.

- [104] S. H. Kim, W. I. Choi, K. H. Kim, D. J. Yang, S. Heo, and D.-J. Yun, "Nanoscale chemical and electrical stabilities of graphene-covered silver nanowire networks for transparent conducting electrodes," *Scientific reports*, vol. 6, p. 33074, 2016.
- [105] M. Topsakal, H. Şahin, and S. Ciraci, "Graphene coatings: an efficient protection from oxidation," *Physical Review B*, vol. 85, no. 15, p. 155445, 2012.
- [106] D. Prasai, J. C. Tuberquia, R. R. Harl, G. K. Jennings, and K. I. Bolotin, "Graphene: corrosion-inhibiting coating," *ACS nano*, vol. 6, no. 2, pp. 1102-1108, 2012.
- [107] Y. Zhao *et al.*, "Highly impermeable and transparent graphene as an ultra-thin protection barrier for Ag thin films," *Journal of Materials Chemistry C*, vol. 1, no. 32, pp. 4956-4961, 2013.
- [108] W. Zhang *et al.*, "Use of graphene as protection film in biological environments," *Scientific reports*, vol. 4, p. 4097, 2014.
- [109] J. S. Bunch *et al.*, "Impermeable atomic membranes from graphene sheets," *Nano letters*, vol. 8, no. 8, pp. 2458-2462, 2008.
- [110] E. Sutter, P. Albrecht, F. E. Camino, and P. Sutter, "Monolayer graphene as ultimate chemical passivation layer for arbitrarily shaped metal surfaces," *Carbon*, vol. 48, no. 15, pp. 4414-4420, 2010.
- [111] D. Lee, H. Lee, Y. Ahn, Y. Jeong, D.-Y. Lee, and Y. Lee, "Highly stable and flexible silver nanowire-graphene hybrid transparent conducting electrodes for emerging optoelectronic devices," *Nanoscale*, vol. 5, no. 17, pp. 7750-7755, 2013.
- [112] Q. Nian, M. Saei, Y. Hu, B. Deng, S. Jin, and G. J. Cheng, "Additive roll printing activated cold welding of 2D crystals and 1D nanowires layers for flexible transparent conductor and planer energy storage," *Extreme Mechanics Letters*, vol. 9, pp. 531-545, 2016.
- [113] G. A. dos Reis Benatto *et al.*, "Roll-to-roll printed silver nanowires for increased stability of flexible ITO-free organic solar cell modules," *Nanoscale*, vol. 8, no. 1, pp. 318-326, 2016.
- [114] B.-Y. Wang, E.-S. Lee, D.-S. Lim, H. W. Kang, and Y.-J. Oh, "Roll-to-roll slot die production of 300 mm large area silver nanowire mesh films for flexible transparent electrodes," *RSC Advances*, vol. 7, no. 13, pp. 7540-7546, 2017.
- [115] L. Y. L. Wu, W. T. Kerk, and C. C. Wong, "Transparent conductive film by large area roll-to-roll processing," *Thin Solid Films*, vol. 544, pp. 427-432, 2013.
- [116] E. Jung, C. Kim, M. Kim, H. Chae, J. H. Cho, and S. M. Cho, "Roll-to-roll preparation of silver-nanowire transparent electrode and its application to large-area organic light-emitting diodes," *Organic Electronics*, vol. 41, pp. 190-197, 2017.
- [117] C. Zhao *et al.*, "Large-area chemical vapor deposition-grown monolayer graphene-wrapped silver nanowires for broad-spectrum and robust antimicrobial coating," *Nano Research*, vol. 9, no. 4, pp. 963-973, 2016.
- [118] (February, 2018). <http://pro.arcgis.com/en/pro-app/tool-reference/spatial-statistics/average-nearest-neighbor.htm>.
- [119] (April, 2018). <https://www.mathworks.com/matlabcentral/answers/164955-distance-between-several-objects-in-binary-image>.
- [120] A. C. Sajja Sadeque, Yu Gong, Kerry Maize, Amir K. Ziabari, Amr M.S. Mohammed, Ali Shakouri, Timothy Fisher and David B. Janes, "Transient Thermal Response of Microscopic Hotspots in Silver Nanowire Network Conductors," February, 2018.
- [121] P. Li, J. G. Ma, H. Y. Xu, H. C. Zhu, and Y. C. Liu, "The role of graphene in enhancing electrical heating and mechanical performances of graphene-aligned silver nanowire hybrid transparent heaters," *Applied Physics Letters*, vol. 110, no. 16, p. 161901, 2017.



## VITA

Sajia Sadeque obtained the B.S. degree from the Department of Computer Engineering, Bangladesh University of Engineering and Technology (BUET), Dhaka, Bangladesh, in 2006. She received her M.S. degree from the Department of Electrical and Computer Engineering, Purdue University, West Lafayette, IN, in 2012. She received her Ph.D. degree from the same department in May 2018. While at Purdue, she worked as a research assistant in the area of nano-electronics under the supervision of Professor David B. Janes at the Birck Nanotechnology Center and also worked as a teaching assistant for Integrated Circuit Fabrication Lab course. Her research interest includes physics, simulation, fabrication and characterization of flexible electronics, including non-homogenous, 1-D/2-D hybrid nanostructured network systems.